On biophysical aspects of growth and dynamics of epithelial tissues

Dissertation

zur Erlangung des Grades des Doktors der Naturwissenschaften
der Naturwissenschaftlich-Technischen Fakultät II
- Physik und Mechatronik -
der Universität des Saarlandes

von

Sebastian J Streichan

Saarbrücken, 2011

Tag des Kolloquiums

Dekan der Fakultät Physik und Mechatronik

Mitglieder des Prüfungsausschusses

Zusammenfassung

Formgebung von Organen ist ein grundlegendes, ungelöstes Problem des Lebens. Ihre Gestalt resultiert aus raumzeitlich kontrollierten Zellteilungen sowie Bewegungen von Zellen. Um mechanische Stabilität sowie Integrität des Gewebes zu gewährleisten, werden Zell-Zell Wechselwirkungen benötigt. Viele genetische Netzwerke kontrollieren die polarisierte Zellbeweglichkeit oder fördern die Zellteilung. Interaktion zwischen Zellen führt zu einer erhöhten Komplexität. Dennoch bilden sich reguläre Muster. Die Form von Objekten und deren Bewegung unterliegt physikalischen Gesetzen. Zellen sind von aktiver Art, teilen und bewegen sich, interessante Eigenschaften für ein Material, welche in neuen Erkenntnissen münden könnten.

In dieser Arbeit führen wir eine quantitative Charakterisierung von zwei Modellsystemen der Morphogenese von Geweben durch. Anhand von kultivierten Epithelien behandeln wir die mechanischen Eigenschaften der Wachstumskontrolle und identifizieren Regulationsmechanismen. Darauf aufbauend, schlagen wir eine phänomenologische Modellbeschreibung für Gewebedynamik vor, welche die Beobachtungen reproduziert. Wir machen Gebrauch von diesen Methoden um die Mechanik der Migration eines embryonalen Epithels zu verstehen. Dabei messen wir die gerichtete Bewegung des Gewebes und zeigen, dass die resultierenden Daten durch Kopplung der biophysikalischen Motilitätsbeschreibung an einen dynamisch regulierten Polarisationsmechanismus reproduziert werden.

Abstract

A fundamental and unresolved question of life is how organs are formed. The shape and form of organs emerges by spatio temporally controlled division and motility of cells. As both processes are tightly coordinated, interactions amongst cells are required to ensure stability and integrity. Many genetic networks controlling the polarised cell motility or promoting cell division have been identified. Action between cells results in an increased complexity. Yet cells give rise to regular patterned organs. The form of objects and their motion is subject to physical laws. Cells are of an active character, divide and move, interesting properties for a material, with potentially new knowledge emerging from their study.

Here, we perform a quantitative characterisation of two experimental models for tissue morphogenesis. Using cultured epithelial sheets we address the mechanical properties of growth control and identify regulatory mechanisms. Based on this study, we propose a phenomenological description of tissue dynamics, reproducing the observed data. Using the methods developed to understand the cultured sheet, we approach the role of mechanics in the migration of an embryonic tissue. We measure the directed motion of the tissue and show that the findings can be reproduced by coupling the biophysical model of motile cells to a dynamically regulated polarisation mechanism.

Acknowledgements

First and foremost I want to thank my family, Sophie and Friederike, for they are the most special people in my life. I am grateful for your understanding and care.

I want to thank my supervisors Lars Hufnagel, Darren Gilmour and Eric Karsenti, for giving me the opportunity to work in a highly stimulating environment and for supporting my projects. I am grateful to the members of the Hufnagel and Gilmour group, for generating a nice and relaxed working atmosphere. Especially, I want to express my gratitude to Gerrit Heuvelman, who constructed the laser ablation setup that I made extensive use of. I am obliged to thank Daniela Holzer, Andreas Kunze and Andreea Gruia, for providing me with excellent technical support as well as taking care of cell culture and fish. The discussions and collaborations with Guillaume Valentin, Celine Revenu and Virginie Lecaudey have been very useful. Thanks to Christian Hoerner, for sharing more than a desktop. I also want to thank Boris Shraiman and Alberto Puliafito for valuable discussions.

I am thankful to my friends, my parents, brothers and sisteres for supporting and encouraging me along the way.

Contents

Chapter 1

Introduction

During the life cycle, an animal experiences a sequence of changes in its outer and inner appearance. Many processes can be used to shape the body parts. Spatio-temporal regulation of growth and regrouping of cells, involving active migration give rise to organs. As D'Arcy Thompson in his book on growth and form states [Thompson92] "... it is obvious that the form of an organism is determined by its rate of growth in various directions; hence rate of growth deserves to be studied as a necessary preliminary to the theoretical study of form, and organic form itself is found, mathematically speaking, to be a function of time."

Similar to the entire body, organ formation requires precise control of the growth rate of the constituent cells, where initially fast divisions are required to suddenly stop at the point of proper organ size. Phenotypes observed when migration or growth are affected induce severe consequences on the organism, ranging from malformed limbs to lethal migratory cancers proliferating in an uncontrolled manner.

A common theme is the connection of cells to form a tissue, which mediate mechanical stability and integrity of the structure [Lecuit08]. The form of organs is determined by growth, apoptosis, passive and active motion of cells as well as cell deformation in response to extensively studied signalling molecules [Lecaudey06, Wolpert07, Lecuit07]. Cell shape, size and their motion are subject to mechanical forces [Lecuit08, Fletcher10, Guck10] and provide key understanding to final organ form and may be quantified, resulting in data that can be analysed using physical

principles. These can feed into quantitative models and their predictions be tested, increasing understanding about the system at hand.

Considering cells as a kind of active matter [Menon10, Ramaswamy10], growth may also introduce new insight to physics. Conversely studies on the ability of cells to divide results in a different mechanics than that of other material such as soap bubbles. Growth as such is quite different from the growing systems that have been studied in physics. Where in the latter case, new atoms are added from the outside to the pre-existing structure, in the biological case, cells can also divide in the bulk of tissues. Such a division will have consequences on the mechanical configuration of the tissue. On the other hand, a thinkable scenario is a feedback of mechanical configuration of the tissue to cells and their ability to divide.

What is the nature of the forces in motile tissues that proliferate, where do the forces originate and what is their feedback on the signalling pathways of cells? Due to the increased knowledge about migration and signalling pathways based on single cells as well as an increased understanding of the biophysical description of non migratory tissues, the coupling of growth to motility of tissues has become a tractable problem [Friedl03, Shraiman05, Hufnagel07, Käfer07, Farhadifar07, Rorth09, Friedl09].

1.1 Learning from single cells

Cells are active discrete subunits of the body, which have a set of remarkable properties. They are able to duplicate by cell division, actively modulate their shape, differentiate to perform specialised functions and migrate actively. In the next paragraphs, we will discuss the basic concepts employed to shape cells and maintain their integrity.

A lipid bilayer, part of the cells plasma membrane separates the cells interior from its environment. Eukaryotic cells contain a number of compartments known as organelles, described as "little organs" each being highly specialised for a particular function. Examples are provided by the nucleus, which contains and secures the genetic code, or the golgi apparatus, where macromolecules become prepared for leaving the cell. Cells exist over various length scales ranging from a micron in

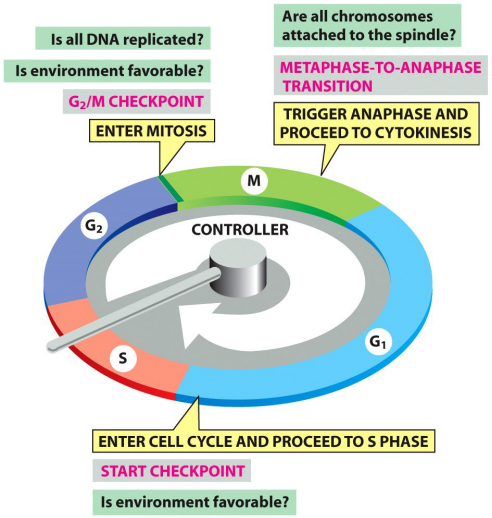

Figure 1.1: Cell Cycle Control. The 4 phases of the cell cycle are subject to control of molecular signalling. Progression in the cell cycle, that rotates from $G1$ over S, $G2$ to M is controlled by checkpoints, where progression can become arrested or continue, depending on the provided information. Most important check-points are found at the interface of the phases, where essential aspects such as damage or proper replication of DNA are probed. Taken from [Alberts08].

bacteria to meters in for instance neurons [Phillips09].

1.1.1 Regulation of cell division

The time between birth and division of a cell is called cell cycle and its control is central to the prevention of overgrowth in tissues. It is subdivided into four parts, with gap phases called $G1$ and $G2$ separating the phase of DNA synthesis called S-phase from the phase where the actual division is conducted, called M-phase. Specific signals are required for the transition from one phase in the cell cycle to another. Numerous such check-points controlling the continuation of the cell cycle such as $G1$ to S or $G2$ to M-phase, where for instance a check for damage of the genetic code is performed, exist [Alberts08]. There is a large range of time scales that cells take to complete the cell cycle, ranging from fast division on the scale of minutes in the early *Drosophila* embryo to days also depending on the availability of nutrients or temperature.

One control strategy is provided by contact inhibition of proliferation, where cells cease division and become immobile due to an increased cell density independent of nutrient abundance [Abercrombie67, Castor68, Abercrombie70, Martz72]. When contact inhibited, cells leave the cell cycle and enter another gap phase called $G0$,

where they are known to exist for a long time. For example, most cells in adults have stopped proliferation and entered $G0$ phase [Rorth09].

Many inputs can influence the checkpoints between phases in the cell cycle. Chemical signals known as growth factors promote growth. Transmembrane receptors are embedded in the membrane and accept these signals from the environment. They trigger signalling cascades inside the cell in form of molecular interactions, eventually resulting in cell cycle progression. For example, cell cycle control at the end of $G1$-phase was shown to involve ERK, an activator molecule of the MAPK signalling pathway, which through a sequence of molecules enables the cell to progress in cell cycle towards S-phase [Sherr96, Matsubayashi04, Shixiong04].

Interesting studies of single cells and their shapes proved a link between the shape and growth in cells, indicating mechanical control of cell proliferation [Folkman78]. Experiments, where cells are provided with a well defined space on which they can spread revealed a minimal area required for cell cycle progression [Chen97, Huang99]. The possible involvement of mechanics in the control of proliferation was further pursued in studies on the cell cycle, where a cytoskeleton dependent checkpoint for S-phase entrance, independent of MAPK signalling was identified [Huang02]. Constraining tissues into well defined geometric structures confirmed that mechanics can act as a regulator of proliferation in cells [Nelson05]. Thus many ways of controlling the cell cycle are employed, leading to a complex network of interactions required for cell cycle progression.

1.1.2 Single cell motility

A remarkable feature about cells is their ability to consume chemical energy to perform mechanical work in form of active motion. The machinery that drives dynamic cell shape changes during crawling is elucidated from studies on single cells. Microfilaments, polarised polymers of the molecule actin are essential for crawling. In a process called treadmilling, the filaments can grow at one end while shrinking from the other. They can be arrangend in different ways, a gel-like network structure forming the cortex of a cell, anti-parallel bundles in form of stress fibres, or parallel

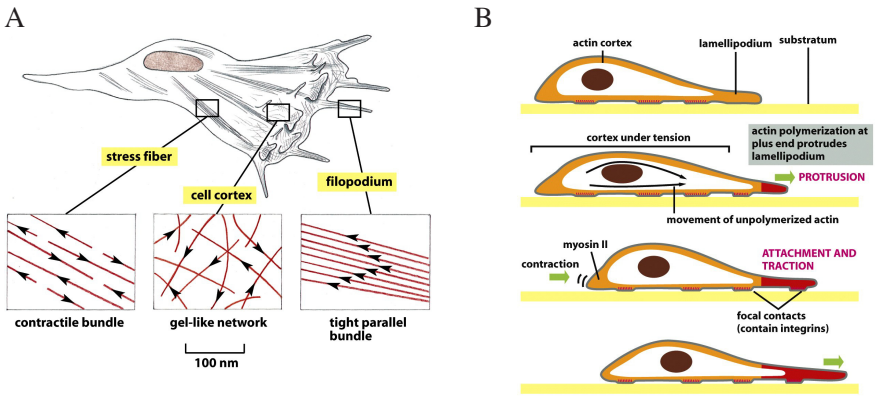

Figure 1.2: Single cell motility. A) Actin can be arranged in form of gels at the cortex of the cell or bundles which can be parallel or antiparallel, where antiparallel bundles and the gel enable contractility via myosin II motors. B) A polarised cell forms protrusions at its leading edge in form of lamellipodia, which subsequently results in formation of new attachment points to the substrate, necessary for traction. Contraction of acto-myosin network pulls the cell forward and contracts the rear. Taken from [Alberts08].

bundles in form of filopodia as shown in fig. 1.2. The energy released by hydrolysis of ATP, which is a common energy carrier in cells, is used by a pair of connected Myosin II motors, each attached to neighbouring antiparallel actin filaments, to move along the plus end of the respective filament, thereby enabling contractility. Cell adhesion molecules known as integrins couple the dynamic actin cytoskeleton to the cell surface and substrate interface to allow traction.

Cells migrate on extracellular matrix (ECM), reiteratively applying a standardised scheme of interdependent steps as shown in fig. 1.2 B). The cells cytoskeleton becomes remodelled, actin based protrusions called lamellipodia and filopodia form. Binding via molecules such as integrins upon contact with the basement membrane molecules eventually results in the formation of focal adhesions, a stable cluster of integrins connecting the cells cytoskeleton to the substrate [Lauffenburger96, Friedl03, Vicente-Manzanares05, Fletcher10]. The control of the acto-myosin cytoskeleton is separated in two parts. Thus cortical actin generating the lamellipodia is independently controlled from the contractile acto-myosin network arranged in stress fibres

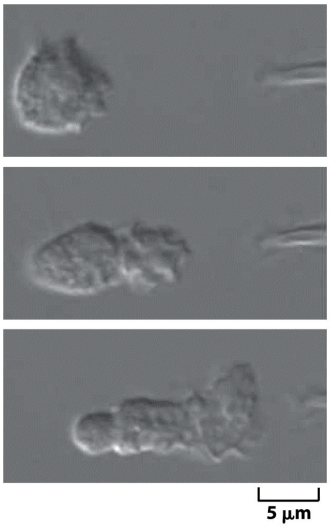

Figure 1.3: Chemotaxis leads to polarisation. A pipette shown in the right of the panels is used to generate a source of chemical signal, that attracts the cell. Rapid formation of a cytoskeleton based polarisation of the cell is observed and it moves towards the signalling source. Taken from [Alberts08].

that connect to the focal adhesions. Active contraction of the stress fibres pulls the cell body in the direction of migration [Friedl03]. Finally focal adhesions at the rear must be broken and the rear contracted, for the cell to advance.

1.1.3 Chemotaxis is a common polarisation method

The molecular machinery enabling the cell to crawl requires directional information. A method to establish polarity in a cell is given by concentration fields of signalling molecules. In a process called chemotaxis, cells move towards or away from local maxima in signalling molecule concentration by approximating the gradient of concentration as shown in fig. 1.3 [Dormann03, Stephens08].

Examples of single cell polarisation are provided by primordial germ cells (PGC), which give rise to sperm and eggs in the male and female gonads, respectively. In zebrafish embryos, PGCs move individually from somites to the gonad, where the ligand receptor pair SDF1a/CXCR4b directs the motion. Initially round cells emit protrusions around their periphery and become polarised in the direction of greater SDF1a abundance [Blaser05]. Note that migration via SDF1a/CXCR4b is used repeatedly for cell migration, such as cancer migration or the migration of lateral line primordium of zebrafish, which will be discussed in detail later.

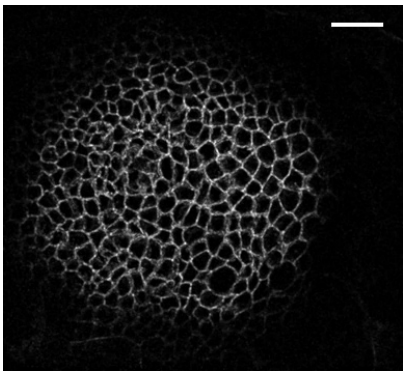

Figure 1.4: Epithelial tissues. Shown is the *Drosophila* wing disc epithelium. A junctional network of tightly coupled cells is a characteristic observation in epithelia. Rearrangements of the topology but no net motion occur. Scale bar 20 μm.

The slime mold *Dictyostelium discoideum* is used to study the phenomenon of chemotaxis on the level of a cell collective [Weijer09]. Initially individual migrating cells can in response to nutrient withdrawal enter a collective migration phase, where cells aggregate and later form a motile slug. The aggregation of cells is triggered by the diffusive chemoattractant cyclic adenosine monophosphate cAMP, which is secreted by cells and amplified in a positive feedback loop. Sensitivity to cAMP reduces over time in an adaption process to the high cAMP levels, during which cells cease to follow cAMP gradients. Reduction of cAMP levels by degradation via secreted phosphodiesterase leads to a reset of the adaption [Garcia09, Gregor10].

1.2 Cells in tissues

1.2.1 Junctions connect cells to form tissues

In higher eukaryotes, the primary function of cells is to form tissue, apart from a few exceptions. Cells are arranged in a so called epithelium, that is characterised by tight connections between neighbouring cells and a clear positioning of specialised molecules along the apico-basal axis within cells [Alberts08]. Figure 1.4 shows an example epithelial tissue, the wing disc of *Drosophila*. It forms from around 50 cells and by division spans scales up to $5 \cdot 10^4$ cells. Epithelia are dynamic in the sense that cell division and topological rearrangements lead to consecutive sequences of shape changes, that must be controlled in order to reassure integrity of the tissue.

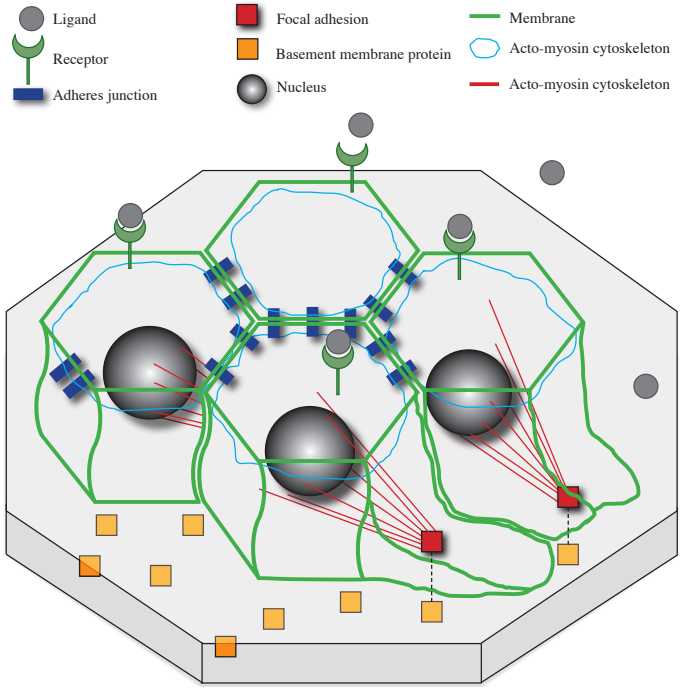

Figure 1.5: Interaction of cells in tissues. Cells adapt cylindrical shape with polygonal apex. Connection of cells is mediated via adherens junctions, which are linked to the acto-myosin cytoskeleton inside the cell. Focal adhesions establish connection to the extracellular matrix via binding to basement membrane proteins. Inside they are connected to stress fibres of acto-myosin cytoskeleton. Cell-cell contact and ligand mediated signalling form the basic parts of cell cell communication.

Connection of cells is known to be mediated by adhesion molecules such as cadherins as shown in dark blue in fig. 1.5, which increase the tendency of attaching cells to increase their surface of contact. The junctions formed by adhesion molecules are called adherens junctions. Cortical tension that counterbalances this tendency is generated by the cortical acto-myosin cytoskeleton inside the cell depicted in light blue rings at the apical part as shown in fig. 1.5 [Lecuit07]. Together these opposing processes generate intercellular surface tension. At the basal part of the cells, integrins in focal adhesions establish the connection to the extracellular matrix. The acto-myosin cytoskeleton arranged in fibres connects the focal adhesion to the cell body.

1.2.2 EMT and migration of epithelial tissues

For a long time, epithelia where considered static in the sense of motility, albeit dynamic in the sense of cell cell rearrangements and division. The common view was that for a tissue to move, cells must undergo a transition to a mesenchymal state,

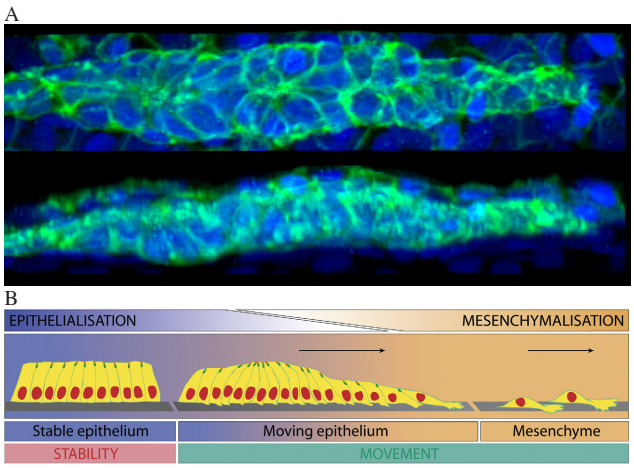

Figure 1.6: Partial EMT allows epithelial migration. A) Top and side view on posterior lateral line primordium in zebrafish, an example of a motile tissue showing epithelial as well as mesenchymal features. Green channel shows membrane, and blue channel nuclei. Tissue moves from left to right. Cells at the rear display epithelial properties, whereas flat mesenchymal character is adapted in the front. B) Schematic of EMT allowing cells to move. Taken from [Revenu09].

where they lose the apicobasal polarity and connectivity characterising epithelia and become mobile. This process is termed epithelial to mesenchymal transition (EMT). Such a process occurs for instance during the folding movements of gastrulation, where the future mesoderm, that gives rise to muscles or the skeleton undergoes an EMT and moves into the embryo, leaving the future parts of the ectoderm, giving rise to skin or nervous system, on the periphery of the embryo [Wolpert07].

The long standing paradigm of immobility of epithelia is inconsistent with the frequent occurrence of migrating epithelial sheets during development, with only a few cells losing epithelial morphology and adapting mesenchymal morphology while remaining in contact with each other. An example of such a transition is provided by the posterior lateral line primordium as shown in fig. 1.6 A), where cells at the rear of the tissue have a clear epithelial morphology and a leading edge, comprising cells of mesenchymal character. Figure 1.6 B) shows a schematic of the epithelial to mesenchymal transition EMT [Revenu09]. We define a collective migration as the movement of groups of cells, that are physically coupled. Many derived forms of collective cell migration exist, such as sheet migration present in wound healing [Rorth07, Shaw09].

EMT plays a crucial role in the invasive motion of cancers, its study of utmost

importance, as epithelial cancers are the most common ones. A cancer has differentiating cells in its bulk and an invasive zone undergoing EMT - suitable for the invasion of different tissue compartments, resembling tissues observed in non-malignant situations such as the posterior lateral line primordium in zebrafish [Baum08].

1.2.3 Biophysical description of non migratory tissues

The understanding of tissue mechanics is still in its infancy. Mechanical integrity and functionality of organs in conjunction with remodelling of tissues due to proliferation, shape changes or motion are the seemingly contradictory aspects, which must be coordinated and balanced by cells.

Models regarding growth control and the resulting shapes are becoming increasingly popular. Shraiman considers the problem of control of proliferation rate in growing immobile tissues, which are not connected to a substrate. Heterogeneous growth rates throughout the tissue leads to stress, when the tissue doesn't respond by remodelling. In the example epithelium of the *Drosophila* wing disc, such remodelling is not observed. The distribution of the growth promoting molecules however, is known to be heterogeneous, at a high level in the centre of the tissue exponentially dropping outwards. This would favour cell division in the centre, yet a homogeneous proliferation rate throughout the tissue is observed. Based on the description of an elastic solid, an integral feedback mechanism, that relates local differences in growth rate to stress is proposed as a regulator. Local overgrowth induces stress, which reduces the growth rate, enabling the control of an even proliferation throughout the tissue [Shraiman05].

A step towards biophysical description of cells and their interaction by cell to cell contact is provided by considering tension and pressure, which feed into an energy function, that upon minimisation describes the configurations of cells as a consequence of the balance of forces emerging from their interaction [Lecuit07]. This was successfully applied to describe shape distributions in tissues, establishment of compartments boundaries or convergent extension based on anistropy in tension [Käfer07, Rauzi08, Landsberg09].

Describing epithelia in a two dimensional approximation, the basic building blocks of the energy function are given by a term considering area fluctuations of cells as well as a surface tension term

$$E = \sum_{\alpha} p_{\alpha} \frac{(A_{\alpha} - A_0)^2}{\sqrt{A_{\alpha}}} + \sum_{ij} l_{ij}\sigma_{ij},$$

where A_{α} describes the area of cell α around a preference area A_0, with pressure p_{α}. This is counterbalanced by the surface tension σ_{ij} at cell-cell interfaces of length l_{ij}.

Based on variations of such energy functions and an earlier developed lattice representation of cells, where a cell is described as a polygon with vertices as the dynamic variable, the problems of size determination, or polygon distributions in growing epithelia where considered [Hufnagel07, Farhadifar07, Honda84]. Vertex configurations are obtained by balance of forces reached at local minima of the energy. Topological rearrangements in the lattice mediate neighbour exchanges. Growth is introduced as a discrete process, where a polygon 'divides' by introduction of a separation line, that intersects with two opposing bonds. The points of intersection form the new vertices. Upon division, the lattice configuration is obtained by energy minimisation, describing a quasistatic evolution between local minima. Distributions of polygons in growing lattices resembling polygon distributions in epithelia are observed [Farhadifar07]. Coupling of the mechanical feedback mechanism for growth control explained above and functional dependence of the growth rate on measured growth promoter distributions, results in growth arrest in lattices, that resembles that of organs [Hufnagel07].

1.2.4 Migration of growing tissues

Single cell analysis of growth and migration has revealed mechanisms implemented by cells to control their growth and motility. Knowledge of the interplay of growth and migration in tissues however falls short. A number of questions arise, for instance, how is the polarisation of cells in the tissue regulated in conjunction with tight coupling of cells? Uncertainty about the mechanisms of motion lead to conflict-

ing hypothesis, ranging from cooperative migration, treating cells in the collective as equally potent polarised migrators, to the common view of specialised leader cells positioned at the boundary dragging the collective behind [Vaughan66, Farooqui04]. Polarisation of single cells can be achieved by chemical signalling, how is this translated to the level of a moving epithelium, which can span considerable lengths. This leads to scenarios with cells experiencing different signalling molecule concentration gradients depending on their position within the tissue. How does this become coordinated to keep the tissues integrity and maintain its ability to move?

Motion also triggers activity of signalling pathways used for growth promotion, such as the MAPK signalling pathway [Huang99, Benoit09]. This immediately raises the question, how growth is coordinated with motion to maintain integrity and stability of the tissue. The view of partial EMT for motile epithelia and its parallel in form of malignant migrating tissues, where growth control is out of order, fuel the study of the interplay of growth control in dynamic adherent cells.

1.3 Thesis

In this thesis, we will consider two different types of growing dynamic epithelia. A growing tissue of culture cells will be used to address the question of mechanical regulation of cell cycle control. In the second part, we will study an embryonic tissue, that performs chemical signalling mediated directional migration. We will discuss the mechanical consequences and their use for organ deposition.

In Vitro

At the morphological transition to epithelial character, growing colonies of adherent cells are characterised by a transition from exponential to subexponential size increase. This is in conjunction with a reduced velocity of cells in the bulk of the colony, due to increased cell density. Short range ordering appears and cell size approaches a steady distribution accompanied by growth arrest. Based on this, we develop a model showing that 1) size dependant growth rate, 2) finite velocity of cells and 3) plastic cell size increase, can explain observed measurements and correctly predict behaviour after constraint release. Furthermore, we find that epithelial to mesenchymal transition is characterised by a melting of the tissue in form of reduced density, with successively increasing cell area leading to cell cycle advancement. We identify two mechanical checkpoints controlling cell cycle progression.

In Vivo

We consider chemical signalling based directed migration of tissues and find that this type of motion is characterised by a highly ordered migration, that leads to stretching of the tissue. We propose a mechanism that translates polarisation into active remodulation of uniform distributed chemokine and show that this mechanism predicts length dependence of tissue velocity. By introducing growth, we show that this mechanism is suitable for the description of organ formation. The predicted anisotropic stress distribution due to different migration efficiency of individuals in the tissue is observed by direct measurements.

Chapter 2

Biophysical aspects of growth and motility of epithelia

2.1 Introduction

Cells in an epithelial tissue gain motility, by epithelial to morphological transition (EMT). Textbook EMT is described as the transition from a tightly coupled epithelium to isolated migrating cells. The most common class of cancer cells involves epithelial cells that undergo EMT, and form motile cells suitable for the formation of metastases [Baum08]. In recent years, more and more motile tissues, displaying a mixture of epithelial and mesenchymal character have been identified, indicating a grey area between immobile epithelial tissues and motile single cells [Revenu09]. For example, wounding a tissue results in EMT of boundary cells, that invade the free space. The tissue is known to respond with proliferation and cover the wound site. The regulatory mechanisms of proliferation are poorly understood. Growth promoting pathways involved are identified to play a role in the wound healing process, however the large number of proteins identified prevents a clear picture [Vitorino08].

Just as cells can switch from epithelial to mesenchymal character, they can also undergo a mesenchymal epithelial transformation, called MET [Baum08]. This is observed, when mesenchymal cells come together and upon formation of contact

adopt clear epithelial characteristics such as apico-basal polarity. Contact inhibition of proliferation is defined as the long term state that emerges after a gradual decrease in cell motility in conjunction with division arrest due to increased cell density, and used as a descriptor for the state of proliferation of arrest [Abercrombie67, Castor68, Abercrombie70, Martz72]. It is assumed that contact inhibition of proliferation is induced by cell to cell contact. Data shows that the MAPK signalling pathway, promoting growth, is involved via its ERK branch [Shixiong04]. On the other hand, adherens junctions are assumed to play a role [Tinkle08], however the complex phenotype prevents a clear picture.

Here, we perform a quantitative study of the two effects MET and EMT, in order to obtained better understanding of the regulatory mechanisms involved. For this, we use a sample epithelium in cell culture. This provides the ideal setting for well defined studies, as signalling and environmental influences on cells can be controlled, a much more difficult task to do in other situations, e.g. wound healing in the embryo [Kiehart00, Solon09, Fenteany00, Farooqui04, Vitorino08]. Cultured Madin-Darby Canine Kidney (MDCK) cells are a kidney cell line derived from dogs and used as an *in vitro* model of epithelial cells [Rothen-Rutishauser98]. MDCK cells can be cultured for many weeks and their behaviour under various conditions with different culture media is well studied [Gaush66, Taub79]. After several days, the cells form a sheet, that has been shown to proliferate with a cell cycle duration of about 18 hours and comprises highly motile cells, which eventually undergo contact inhibition of proliferation. The strict flat sheet character of the tissue furthermore simplifies microscopy and data analysis. Presenting cells with free space, which is achieved by wounding the tissue or releasing boundary constraints, where cells are grown against a removable boundary results in EMT [Fenteany00, Nikolic06, Poujade07]. Directional motion of the tissue towards free space is reported to be dependant on a branch of the MAPK signalling pathway, as inhibition of this branch results loss of tissue motility [Fenteany00, Farooqui04, Altan04]. ERK, a player in another MAPK signalling pathway branch is also reported to play an important role in wounding. [Matsubayashi04] report on two waves of ERK travelling through tissue upon wounding, a fast first wave on the time-scale of minutes and a slower second

wave on the time-scale of hours, which was found to have a coupling to cell motility [Nikolic06]. Inhibition of ERK via MAPK/ERK Kinase (MEK) inhibitors resulted in a significantly reduced boundary advancement. We will begin with a quantitatively analysis of the contact inhibition phenotype, where we consider a growing colony of MDCK cells.

2.2 Mechanical aspects of mesenchymal to epithelial transition

This part is currently under review with PNAS [Puliafito11].

In order to study colony growth, a few cells where seeded on a flat surface. With time, cells divide and a flat colony with negligible variations in the third dimension grows as shown in fig. 2.1 A). The expansion of the colony is characterised by a velocity fluctuating around 15 $\mu m/h$ and the boundary of the colony exhibits a rough surface with finger like structures emerging, similar to previous observations [Poujade07, Petitjean10, Mark10].

Measurements of the total colony size reveal an exponential law for area increase for up to five days as shown in fig. 2.2 A). Segmentation of cells based on a combination of membrane and nuclear markers provides the number of cells in a colony as well as the sectional area of individual cells. When multiplying the average cell size with the total number of cells at a given point in time, one finds that the result coincides well with the total area of the colony at that point in time. As shown in fig. 2.2 B) the cell density in the same time fluctuates around a constant value. This indicates, that cell division following an exponential rate drives colony expansion.

As the colony size continues to increase, it begins to deviate from the observed exponential law after approximately five days as shown in fig. 2.2 A). At the same time, an onset of gradual cell density increase in the bulk of the colony is observed as shown in fig. 2.2 B). As the flat sheet character remains, we interpret this cross over from exponential to subexponential colony size increase as the inability of the colony to accommodate space for new born cells at continued proliferation in the

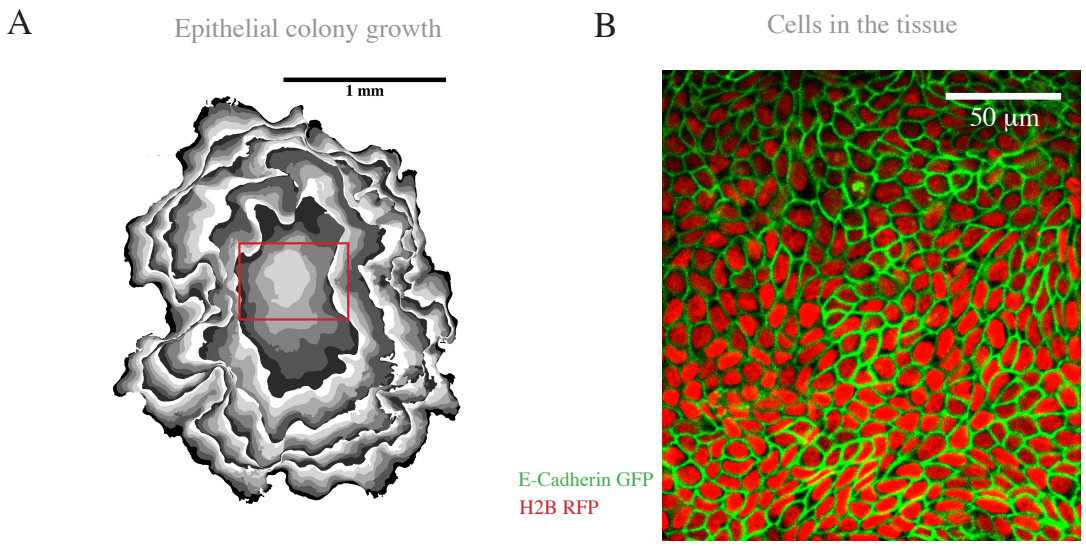

Figure 2.1: Epithelial colony growth. A) A growing epithelial colony. Binary images superimposed and greyscale colour coded. Black contours correspond to 3, 4.8, 5.5, 5.9 and 6.3 days respectively. Frame indicates centre of the colony. B) MDCK cells stained for E-Cadherin-GFP localised at the adherens junctions in the green channel and H2A-FRP labelling the nuclei in the red channel. Scale bar is 50 μm.

bulk, due to finite boundary advancement, limited by the single cell maximum speed of 15 $\mu m/h$. Two types of response can be thought of: 1) Reduction of cell size in the bulk, due to continued and unchanged cell division, with a resulting exponential increase in density or 2) reduction of the rate of cell division in the centre of the colony. Cell density does not increase exponentially as shown in fig. 2.2 B) and thus cell division rate must change.

With higher density, the velocity gradually reduces as shown in red in fig. 2.2 C). This is accompanied by an appearance of increased order in the system as shown by the radial structure function in fig. 2.2 D). It is defined as the ratio of local density in annulus at a distance R from a reference cell and the average tissue density. Before velocity reduction, the structure function shows an exclusion zone corresponding to the size of a nucleus, followed by a gradual increase and saturation. This indicates that cells are disordered and don't overlap. At the time of transition to arrested

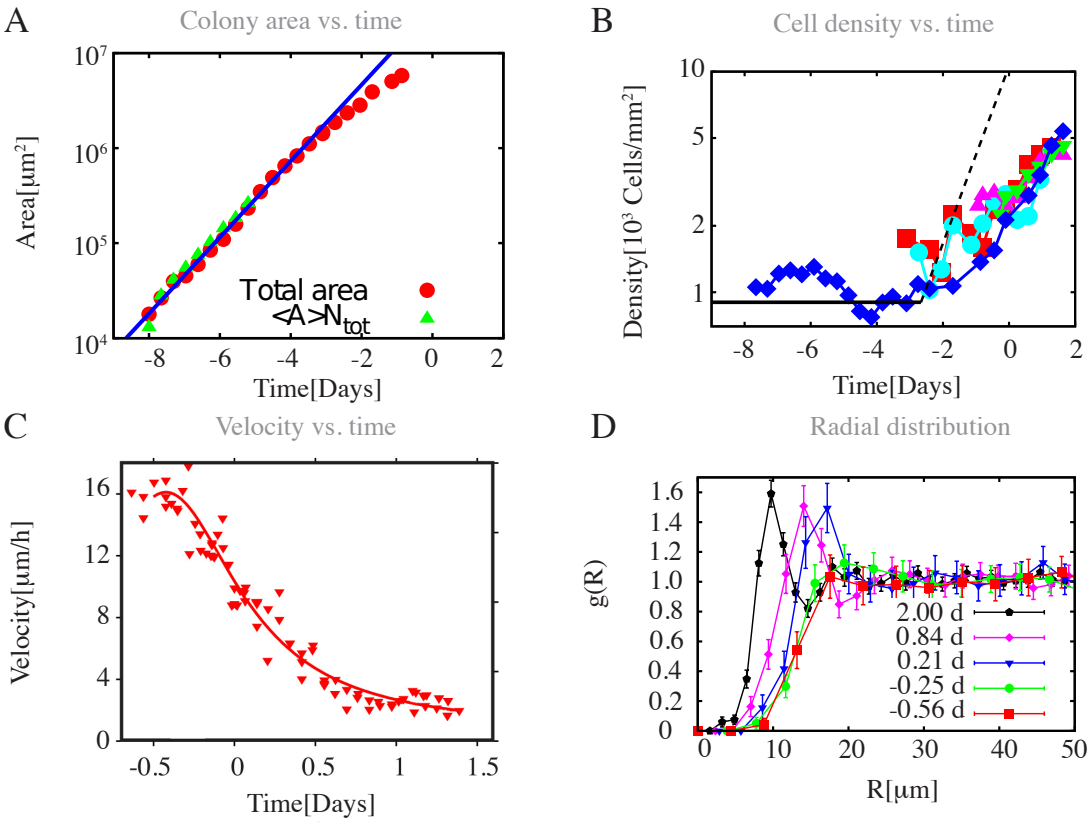

Figure 2.2: Colony growth, cell motility and cell density at the morphological transition. A) Total area covered by the colony as a function of time in days shown as red dots. Blue line indicates exponential growth. Green spots show number of cells multiplied by average cell size. B) Cell density as a function of time. Initially cell density fluctuates around a constant value indicated as black line and subsequently increases markedly. Black dashed line indicates exponential increase. Colour codes for different fields of view in the colonies bulk. $t = 0$ indicates morphological transition. C) Velocity of cells obtained via particle image velocimetry shown in red as described in [Raffel98]. $t = 0$ indicates morphological transition. D) Radial structure function $g(R)$ against intercellular distance. Colour codes for different time points, with $t = 0$ serving as the definition of the morphological transition, determined by first detected peak appearance, where a peak is defined by values of $g(R) > 1.2$.

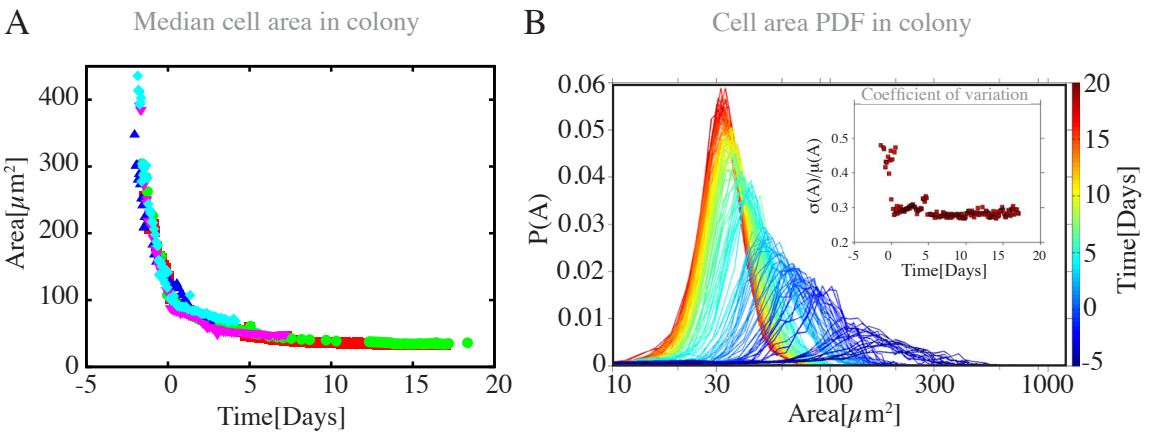

Figure 2.3: Area distribution in epithelial growth. A) Temporal evolution of median cell area in a growing colony of adherent cells over a field of view of 450×336 μm^2. Different colours indicated different experiments, aligned according to the time of appearance of the morphological transition. Cells where seeded at densities, such that a confluent tissue is formed from the start. A sharp initial drop in area is followed by convergence against a constant value around 30 μm^2. $t = 0$ indicates the morphological transition. B) Empirical probability density function of cell size distribution. Colour codes for time, $t = 0$ indicating morphological transition. The distribution shifts towards reduced sizes and converges against a steady distribution. Inset shows coefficient of variation $\sigma(A)/\mu(A)$ as a function of time. A constant value describes a simultaneous reduction of mean and standard deviation.

velocity, a peak in the radial structure function close to the exclusion zone appears. This indicates, that increased short range ordering of cells exists. We refer to the first appearance of a peak in the structure function as morphological transition.

The median area as a function of time around morphological transition is shown in fig. 2.3 A). The time of morphological transition marks a sharp transition from fast cell size reduction to slowed cell size reduction. In the long term, the median cell size approaches a constant value. From beginning of the experiment to the steady median cell size, cells have reduced their area by approximately a factor of 10. The distribution of cell areas starting short before morphological transition is shown in fig. 2.3 B). Experiments start with a flat distribution of cell sizes with

median around 100 μm that shifts towards lower areas accompanied by a reduction in standard deviation due to cell division. In the long term, the area distribution converges against a constant distribution with median around 30 μm^2. The coefficient of variation, described by the ratio of standard deviation and mean of area as a function of time converges against a constant value, indicating that the degree of deviation around the mean area reduces proportionally to the reductions of the mean area. Note that the particular position of the median of the distribution is a function of the substrate cells grow on. Glass dishes tend to support increased cell areas, but the dynamics remains the same.

Qualitatively, the dynamics can be understood as follows: In the exponential growth regime, cells divide and subsequently grow again. This corresponds to a sliding of cells along the area axis, to lower values upon division and increasing again during cell growth. As the density in the tissue increases, cell growth becomes limited and dividing cells can't reach the previous size anymore, resulting in size reductive divisions. This corresponds to a shift of the cell size distributions towards lower values. Thus there are two regimes: One before the morphological transition characterised by high proliferation rate, inducing a gradual velocity reduction, followed by cell size reduction and transiting into the second regime, the post morphological transition regime, where the area covered by cells continuously reduces and approaches a steady distribution. As a potential response to reduced sectional area, cells could increase their height and keep the volume constant. We have observed that the height of a cell in the same time only changes by a factor of two as compared to the ten fold decrease in the area, thus the volume of cells is reduced and area the relevant descriptor. This indicates, that the division rate is subject to cell size, and arrests once cell size drops below a threshold.

2.3 Physical description of dynamic adherent cells

In the previous section, we have observed that cells although coupled can be highly motile and that inhibition in cell motility is followed by progressively decreased rate of cell division accompanied by a reduction of cell sizes. We want to understand in

more detail, to which extend, mechanical constraints can account for the observed inhibition of proliferation. To achieve this we develop a model description for motile adherent cells. Based on an existing description of non-motile cells that adhere to each other, we add an interaction between cells and the substrate they migrate on.

Motion in the lattice model

Lets consider a section through an epithelial cell collective as shown in fig. 2.4 A): On the apical part, a cortical acto-myosin ring is formed and on the baso-lateral part adherens junctions connect adjacent cells. The resulting interfacial tension can be described by a two dimensional vertex based lattice model, that takes the opposing effects of contraction and expansion of the cell interface induced by cortical tension and adhesion into account. Interfaces between cells evolve quasi-statically towards a steady configuration, subject to an energy function comprising a perimeter term and an elastic area term for each cell, representing adhesion between cells as well as the contractile acto-myosin cytoskeleton [Hufnagel07, Farhadifar07, Käfer07]. Adhesion is thought to provide negative contribution to the perimeter, as it has the tendency to increase the surface of contact between cells, whereas the cortical acto-myosin cytoskeleton contributes to both terms [Lecuit08]. To reach the stable configuration, cells can employ passive change in their position by topological rearrangements, if this minimises the energy.

Cells are known to move actively. From studies of migrating single cells, we know that cells form focal adhesions at their leading edge, which become disassembled at the rear of the cell. The filamentous acto-myosin cytoskeleton inside the cell forms contact with the focal adhesions and actively contracts to pull the cell body in the direction of new formed focal adhesions resulting in a net displacement of the cell [Friedl03]. These are the two essential aspects about cell motility, we will add to the lattice model.

A cell is described as a polygon comprising vertices $\mathbf{q}_i \in \mathbb{R}^2$ and the lattice consists of N_V vertices arranged in N_C cells, collectively the vertices are referred to as $\mathbf{q} = (\mathbf{q}_1, \ldots, \mathbf{q}_{N_V}) \in \mathbb{R}^{2\times N_V}$. Focal adhesions of a cell α attach to the substrate, and for simplicity, we assume that their cumulated dynamics can be represented by

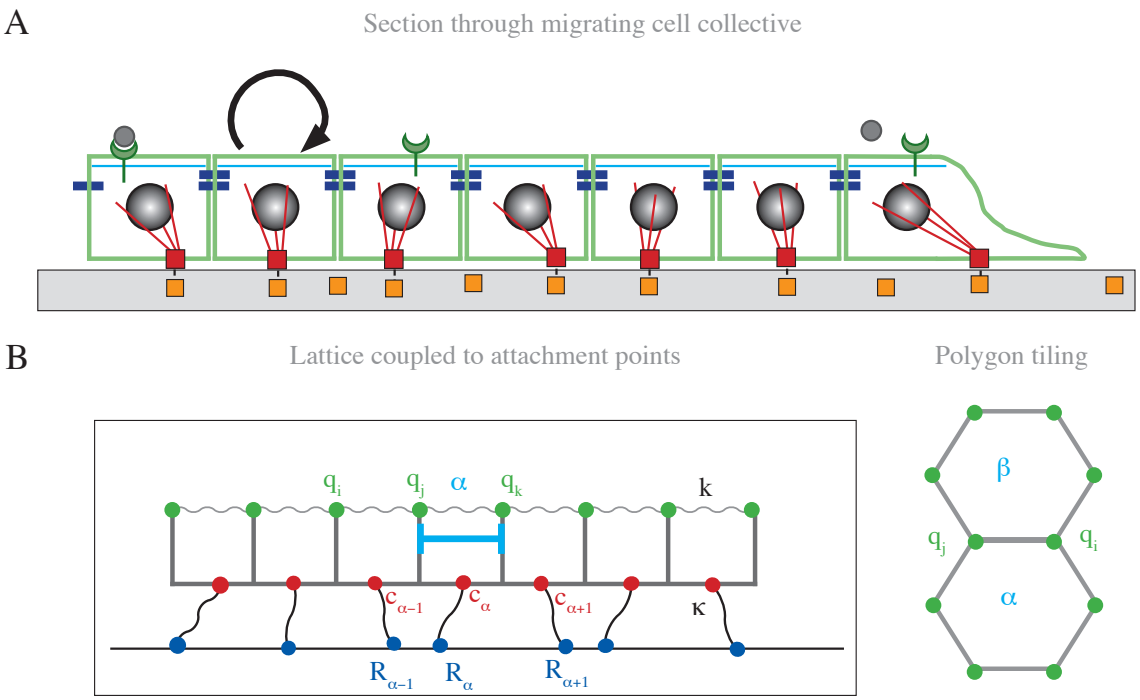

Figure 2.4: Motility in the lattice model. A) Section through migrating cell collective. Apical acto-myosin network shown in light blue, adhesion junctions connecting cells shown in dark blue. Nucleus depicted in grey. Basement membrane molecules indicated by orange box serve as anchor for focal adhesions represented by red box, which connect to the filamentous acto-myosin network in the cell represented in red lines. Active contractions of the filamentous acto-myosin cytoskeleton pulls the cell body along when migrating. B) Cell dynamics described by extended lattice model. Cells α comprise vertices q_i indicated by green dots. Attachment points to the extracellular matrix R_α shown in blue are elastically coupled to the center of mass of each cell C_α indicated in red. Coupling constant κ indicates the coupling strength of attachment points to the center of mass and k coupling strength of vertices (1 dimensional case) respectively. In the two dimensional lattice model [Honda84], cells are described by a polygonal tiling.

a single attachment point $\mathbf{R}_\alpha \in \mathbb{R}^2$. There are N_C cells and the attachment points of the collective are referred to as $\mathbf{R} = (\mathbf{R}_1, \ldots, \mathbf{R}_{N_C}) \in \mathbb{R}^{2\times N_C}$ shown as blue spots in fig. 2.4 B). These are elastically coupled to the cell body, represented by the centre

of mass $\mathbf{C}_\alpha \in \mathbb{R}^2$, reflecting the contractile acto-myosin filaments shown in red in fig. 2.4 A). With $\varrho_\alpha \in \mathbb{R}$ and $A_\alpha \in \mathbb{R}$ as the perimeter and area of cell α respectively, we consider the following extension of the lattice model

$$E(\mathbf{q}, \mathbf{R}) = \frac{1}{2} \sum_\alpha \left\{ \Lambda \varrho_\alpha + p \Big(A_\alpha - A_{0,\alpha}(t) \Big)^2 + \kappa \Big(\mathbf{R}_\alpha - \mathbf{C}_\alpha \Big)^T \cdot \Big(\mathbf{R}_\alpha - \mathbf{C}_\alpha \Big) \right\}. \quad (2.1)$$

In eq. (2.1) the first and second term are the usual perimeter and area term, involving the perimeter of a cell and its area compared to an intrinsic area $A_{0,\alpha}(t)$. The inner product between the difference of the attachment point from the center of mass of the cell with itself couples the lattice to the attachment points. Assuming an overdamped regime, we can introduce a friction τ and obtain the update rule for the vertices

$$\dot{\mathbf{q}}_\mathbf{i} = -\frac{1}{\tau} grad_{\mathbf{q}_\mathbf{i}} \big(E(\mathbf{q}, \mathbf{R}) \big). \quad (2.2)$$

As the dynamics of the system are determined by the relative contribution of the parameters Λ, p and κ, this effectively results in a two parameter description. We need to specify the update rule for the attachment points in order to introduce motion to eq. (2.1). Assuming a random force driving their motility, we get the update rule for the attachment points

$$\dot{\mathbf{R}}_\alpha = -\frac{1}{\nu} grad_{\mathbf{R}_\alpha} \big(E(\mathbf{q}, \mathbf{R}) \big) + \mathbf{v}_{max,\alpha} + \xi_\alpha, \quad (2.3)$$

where $\xi_\alpha(t)$ is defined by its second moment $\langle \xi^a_\alpha(t), \xi^b_\beta(s) \rangle = \Gamma \delta_{\alpha\beta} \delta_{ab} \delta(t-s)$, any non-zero mean contribution may be absorbed into an additional term denoted $\mathbf{v}_{\max,\alpha} = \langle \xi_\alpha \rangle$ and ν is the friction coefficient. Measuring mass in units of time, ν and τ become dimensionless entities representing the time scale of the relaxation dynamics.

2.3.1 Analysing motility in one dimension

To understand the motion of the lattice in more detail, we derive the one dimensional version of eq. (2.1) and derive a multivariate inhomogeneous linear equation of

motion for the system at hand. In one dimension, the perimeter term vanishes and the area term becomes replaced by a spring with constant k and intrinsic preferred length $\mathcal{L}(t) = (l_1(t), \dots, l_{N_C}(t)) \in \mathbb{R}^{N_C}$. The vertices $\mathbf{q} = (q_1, \dots, q_{N_C+1}) \in \mathbb{R}^{N_C+1}$ and attachment points $\mathbf{R} = (R_1, \dots, R_{N_C}) \in \mathbb{R}^{N_C}$ are considered subject to the following energy functional

$$\begin{aligned} E\Big(\mathbf{q}(t), \mathbf{R}(t)\Big) &= \frac{k}{2}\Big(L^T\mathbf{q} - \mathcal{L}(t)\Big)^T\Big(L^T\mathbf{q} - \mathcal{L}(t)\Big) + \frac{\kappa}{2}\Big(\mathbf{R} - \frac{1}{2}C\mathbf{q}\Big)^T\Big(\mathbf{R} - \frac{1}{2}C\mathbf{q}\Big) \\ &= \frac{1}{2}\sum_{i=1}^{N_C}\Big\{k\Big(q_{i+1} - q_i - l_i(t)\Big)^2 + \kappa\Big(R_i - \frac{q_{i+1}+q_i}{2}\Big)^2\Big\}, \end{aligned} \tag{2.4}$$

which is the one dimensional analogue of eq. (2.1).

The evolution equation of the attachment points and vertex positions obtained by gradient descent give the following system of coupled inhomogeneous differential equations:

$$\begin{aligned} \dot{\mathbf{q}}(t) &= -\frac{1}{\tau}grad_{\mathbf{q}}(E) = -\frac{1}{\tau}M\mathbf{q}(t) + \frac{\kappa}{2\tau}C^T\mathbf{R}(t) + \frac{k}{\tau}L\mathcal{L}(t) \\ \dot{\mathbf{R}}(t) &= -\frac{1}{\nu}grad_{\mathbf{R}}(E) + \mathbf{v}_{max} + \xi = -\frac{\kappa}{\nu}\Big(\mathbf{R}(t) - \frac{1}{2}C\mathbf{q}(t)\Big) + \mathbf{v_{max}} + \xi, \end{aligned} \tag{2.5}$$

with the matrices $M = (kLL^T + \frac{\kappa}{4}C^TC) \in \mathcal{M}(N_C+1 \times N_C+1)$, $C \in \mathcal{M}(N_C \times N_C+1)$ and $L \in \mathcal{M}(N_C + 1 \times N_C)$ describing the coupling of vertices with vertices and attachment points with vertices respectively.[1] $\xi(t)$ is a rapidly fluctuating function, defined by its second moment as gaussian white noise $\langle \xi_i(t), \xi_j(s)\rangle = \Gamma\delta_{ij}\delta(t-s)$, with any non zero mean absorbed in $\mathbf{v}_{max}$. By definition of $\mathbf{x}(t) := \big(\mathbf{q}(t), \mathbf{R}(t)\big)$, $\mathbf{g}(t) := \big(L\mathcal{L}(t), \mathbf{v}_{max}\big)$, $\bar{\xi}(t) := \big(0, \xi(t)\big)$ and $A := \begin{pmatrix} M & -\frac{\kappa}{2}C^T \\ -\frac{\kappa}{2\nu}C & \frac{\kappa}{\nu}E_{N_C \times N_C} \end{pmatrix} \in \mathcal{M}(2N_C + 1 \times 2N_C + 1)$, we rewrite eq. (2.5) in form of the corresponding linear system, and find it is given by an inhomogeneous time-dependent Langevin equation, similar to

[1] Expressions for M, C and L are given in the appendix.

that of the Ornstein-Uhlenbeck process

$$\dot{\mathbf{x}}(t) = -A\mathbf{x}(t) + \mathbf{g}(t) + \bar{\xi}(t). \tag{2.6}$$

Following standard Itō-calculus [Gardiner09], the integral of $\bar{\xi}(t)$ is the Wiener process $\mathbf{W}(t)$ and we identify $\mathbf{dW}(t) := W(t+dt) - W(t) = \bar{\xi}(t)dt$. With $B := \sum_{i>N_C+1} \sqrt{\Gamma} E_{ii}$,[2] we obtain the solution of the SDE $d\mathbf{x}(t) = \big(-A\mathbf{x}(t) + \mathbf{g}(t)\big)dt + BdW(t)$ of eq. (2.6)

$$\mathbf{x}(t) = e^{-At}\mathbf{x}(0) + e^{-At}\int_0^t e^{Au}\mathbf{g}(u)du + \int_0^t e^{-A(t-u)}BdW(u) \tag{2.7}$$

with mean given by

$$\langle x(t)\rangle = e^{-At}\langle \mathbf{x}(0)\rangle + e^{-At}\int_0^t e^{Au}\mathbf{g}(u)du. \tag{2.8}$$

Eq. (2.7) gives the general solution of eq. (2.6) for N oscillators with attachment points following gaussian white noise and mean absorbed in $\mathbf{v}_{max}$. Now we carry out an explicit example of a single cell.

Single Cell

Lets consider a single cell described by two vertices $\mathbf{q}(t) = \big(q_1(t), q_2(t)\big)$ and attachment point $R(t)$ subject to random motion ξ as described above. The maximum velocity of the cell is given by v_{max} and its preferred intrinsic length is l_0, such that $g = (-kl_0, kl_0, v_{max})$ is no longer time dependent. The matrices determining the coupling of the variables read as

$$A = \begin{pmatrix} \frac{1}{\tau}\big(k+\frac{\kappa}{4}\big) & \frac{1}{\tau}\big(\frac{\kappa}{4}-k\big) & -\frac{\kappa}{2\tau} \\ \frac{1}{\tau}\big(\frac{\kappa}{4}-k\big) & \frac{1}{\tau}\big(k+\frac{\kappa}{4}\big) & -\frac{\kappa}{2\tau} \\ -\frac{\kappa}{2\nu} & -\frac{\kappa}{2\nu} & \frac{\kappa}{\nu} \end{pmatrix} \qquad B = \begin{pmatrix} 0 & 0 & 0 \\ 0 & 0 & 0 \\ 0 & 0 & \sqrt{\Gamma} \end{pmatrix}. \tag{2.9}$$

[2] E_{ij} denotes the matrix with a 1 at its ith row and jth column and zeros otherwise. $E_{N\times N}$ denotes the unit matrix in N dimensions.

The eigensystem of e^{-At} is given by $\lambda = \big(\lambda_1, \lambda_2, \lambda_3\big) = \big(1, e^{-2k\frac{t}{\tau}}, e^{-\kappa\left(\frac{\tau}{\nu}+\frac{1}{2}\right)\frac{t}{\tau}}\big)$ and $\mathbf{e}_1 = \big(1,1,1\big)$, $\mathbf{e}_2 = \big(-1,1,0\big)$ as well as $\mathbf{e}_3 = \big(-\frac{\nu}{2\tau}, -\frac{\nu}{2\tau}, 1\big)$.

With the mean value of the initial conditions $\langle \mathbf{x}(0)\rangle = \big(q_{10}, q_{20}, \langle R_0\rangle\big)$, eq. (2.8) gives the expected value of the solution expressed in the eigensystem:

$$\langle \mathbf{x}(t)\rangle = a_1\mathbf{e}_1 + a_2\mathbf{e}_2 + a_3\mathbf{e}_3, \tag{2.10}$$

with $a_1 = \lambda_1\left(\frac{1}{2\tau+\nu}\big(q_{10}\tau+q_{20}\tau+\langle R_0\rangle\nu\big)+\big(\frac{\frac{\nu}{\tau}}{2+\frac{\nu}{\tau}}\big)v_{max}t\right)$, $a_2 = \lambda_2\frac{1}{2}\big(q_{20}-q_{10}\big)+\frac{l}{2}\big(1-\lambda_2\big)$ and $a_3 = -\lambda_3\frac{\tau}{2\tau+\nu}\big(q_{10}+q_{20}-2\langle R_0\rangle\big) + \frac{4\tau^2\nu}{\kappa(2\tau+\nu)^2}v_{\max}\big(1-\lambda_3\big)$.

In the asymptotic limit of t, the coefficients a_2 and a_3 in the eq. (2.10) become constants, independent of the initial condition, as $\lim_{t\to\infty}\lambda_{2,3}(t) \to 0$

$$\begin{aligned} a_1 &\propto \frac{1}{2\tau+\nu}\big(q_{10}\tau + q_{20}\tau + \langle R_0\rangle\nu\big) + \frac{\frac{\nu}{\tau}}{2+\frac{\nu}{\tau}}v_{max}t \\ a_2 &\propto \frac{l}{2} \\ a_3 &\propto \frac{4\tau\nu}{\kappa(2\tau+\nu)^2}v_{max}. \end{aligned}$$

Thus, up to the constant contributions of a_2 and a_3, the expected value drifts linearly with time away from the initial condition. The velocity is given by $v_{drift} = \frac{\nu}{\tau}/\big(2+\frac{\nu}{\tau}\big)v_{\max}$, thus it depends on the maximum velocity v_{max} of the attachment points by a load function of the ratio of the time scales for the dynamics of the attachment points and the vertex relaxation.

Fast mechanics limit

Measurements of relaxation of mechanical configuration of cellular networks show that this process appears on a faster timescale as displacement of cells. Thus one may consider the limit $\tau \to 0$, where the lattice immediately relaxes. Then the configuration of the lattice may be obtained by minimisation of the energy function given by eq. (2.4) and the update rule for attachment points remains. In simulations, with N_C cells with attachment points $\mathbf{R} = (R_1, \ldots, R_{N_C})$, vertices $\mathbf{q} = (q_1, \ldots, q_{N_C+1})$

and intrinsic lengths $\mathcal{L} = (l_1, \ldots, l_{N_C})$ one then considers the following algorithm

$$\begin{aligned} E(\mathbf{q}, \mathbf{R}) &= \frac{k}{2}\left(L^T\mathbf{q} - \mathcal{L}\right)^T\left(L^T\mathbf{q} - \mathcal{L}\right) + \frac{\kappa}{2}\left(\mathbf{R} - \frac{1}{2}C\mathbf{q}\right)^T\left(\mathbf{R} - \frac{1}{2}C\mathbf{q}\right) \\ \mathbf{q} &= M^{-1}\left(\frac{\kappa}{2}C^T\mathbf{R} + L\mathcal{L}\right) \\ \dot{\mathbf{R}} &= -\frac{1}{\nu}grad_{\mathbf{R}}(E(\mathbf{q}, \mathbf{R})) + \mathbf{v}_{max} + \xi, \end{aligned}$$

where the lattice configuration is obtained by minimisation of the energy, which is given by solving the inverse problem $grad_{\mathbf{q}}(E) = \mathbf{0}$, and subsequently the attachment points are updated. Note that this procedure also works in two dimensional lattices, where the minimisation of the energy is done by use of the conjugate gradients algorithm [Press07].

Using the general result for a single cell as given by eq. (2.10), we see the following asymptotic behaviour of the expected value of the cell in the fast mechanics limit $\tau \to 0$:

$$\langle x(t)\rangle \propto \begin{pmatrix} q1(t) \\ q2(t) \\ R(t) \end{pmatrix} = \begin{pmatrix} \langle R_0\rangle - \frac{l}{2} + v_{max}t \\ \langle R_0\rangle + \frac{l}{2} + v_{max}t \\ \langle R_0\rangle + v_{max}t \end{pmatrix}, \tag{2.11}$$

which is entirely determined by the dynamics of the attachment points.

2.3.2 Growing colony of adherent cells

Non-adherent cell collectives are known to be able to proliferate at a uniform growth rate [Shraiman05]. Here we want to study the changes appearing in the pattern of growth due to attachment to a substrate. The model described and analysed so far does not include cell division. We incorporate a size dependent cell division to the framework of a one dimensional chain of adherent cells, in order to understand in more detail to which extend the arguments developed above can account for the measured results of a growing colony.

The probability for a given cell to divide in a small time step dt is assumed to depend on the length of that cell $\Delta q_i = q_{i+1} - q_i$. Below a minimal length $\Delta q_i \leq l_{min}$,

cells don't divide, whereas cells above a maximal length $\Delta q_i \geq l_{max}$ divide at a fixed mitotic rate γ, with a linear increase for $l_{min} < \Delta q_i < l_{max}$:

$$p(\Delta q_i) = \gamma\left(\frac{\Delta q_i - l_{min}}{l_{max} - l_{min}} H(l_{max} - l_i) + H(l_i - l_{max})\right) H(l_i - l_{min})dt. \tag{2.12}$$

$H(x)$ denotes the heaviside function, with the convention that $H(x) = 0$ for $x \leq 0$ and $H(x) = 1$ for $x > 0$. Cells are chosen to divide, if a uniform random distributed number not exceeding $p(\Delta q_i)$ is drawn.

Cell division is a discrete event. Given a dividing cell, a cleavage vertex is introduced in the cell, that separates it in two halves. The connection between the formerly neighbouring vertices is then replaced by a connection with the new vertex. The two cells are then assigned attachment points at their respective centre of mass. The rest lengths l_i of the newly introduced cells are set to half the rest length of the dividing cell and assumed to grow according to two different scenarios: 1) The simplest scenario is defined by constant growth at rate η. Once the cell has reached the upper bound for the rest length l_{max}, it stops growing, i.e. $\dot{l}_i(t) = \eta H(l_{max} - l_i)$. 2) An alternative scenario considers plastic cell growth, where the rest length only increases in response to tensile stress and remains constant under compressive or stress free states. Again, once the cell has reached the upper bound for the rest length l_{max}, it stops growing thus $\dot{l}_i(t) = \eta H(\Delta q_i - l_i)H(l_{max} - l_i)$. Note that we neglect removal of cells from the model, as experiments suggest that the rate of apoptosis in the growth of a colony is small compared to the growth rates of cells.

Attachment points dynamics are as described in the previous section with a random force $\xi_i(t)$ driving their motility. Boundary cells have an outwards directed motion, which may be described by a maximum velocity $\mathbf{v}_{max} = (-v_{max}, 0, \ldots, 0, v_{max})^T$.

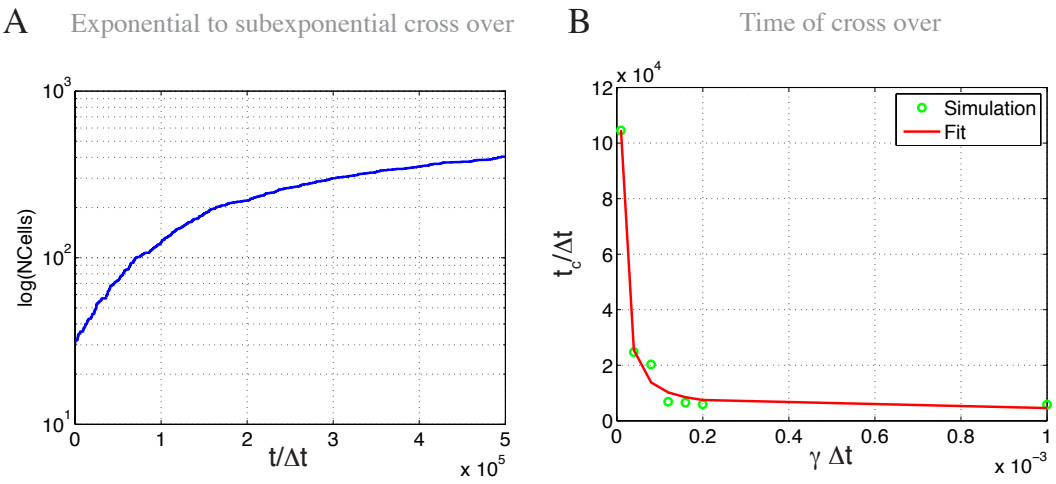

Figure 2.5: Cross over from exponential to subexponential growth. A) Number of cells on semilog scale against simulation runs $t/\Delta t$. Initial exponential increase becomes subexponential with time. B) Cross over time $t_c/\Delta t$ against mitotic rate $\gamma\Delta t$ obtained from simulations shown in green. Fit of $\log\big((2\nu v_{max})/(\gamma l_{max} N_0)\big)/\gamma$ shown in red.

Thus the model is described by the following set of coupled equations:

$$E(\mathbf{q},\mathbf{R}) = \frac{k}{2}\left(L^T\mathbf{q}-\mathcal{L}\right)^T\left(L^T\mathbf{q}-\mathcal{L}\right) + \frac{\kappa}{2}\left(\mathbf{R}-\frac{1}{2}C\mathbf{q}\right)^T\left(\mathbf{R}-\frac{1}{2}C\mathbf{q}\right) \tag{2.13}$$

$$\mathbf{q} = M^{-1}\left(\frac{\kappa}{2}C^T\mathbf{R} + L\mathcal{L}\right) \tag{2.14}$$

$$\dot{\mathbf{R}} = -\frac{\kappa}{\nu}\left(\mathbf{R}-\frac{1}{2}C\mathbf{q}\right) + \mathbf{v}_{max} + \xi \tag{2.15}$$

$$\dot{\mathcal{L}} = \eta H(O\mathbf{q}-\mathcal{L})H(\mathcal{L}_{max}-\mathcal{L}), \tag{2.16}$$

with the probability of a cell to divide defined in eq. (2.12). As an alternative to eq. (2.16) we also consider constant cell growth $\dot{\mathcal{L}} = \eta H(\mathcal{L}_{max}-\mathcal{L})$.

Cross over time

To study the long term dynamics of the above system describing a growing colony of adherent cells, we integrate the equations of motion numerically, with the initial condition, that the attachment points are located at the centre of the corresponding cell, and the cells are at their rest length. Fig. 2.5 A) shows the number of cells as a function of simulation time steps on a semi-log scale. Initially, an exponential increase in cell number is observed, until a cross over to subexponential growth of cell number occurs, in agreement with our experimental results. Cross over from exponential to subexponential increase in cell numbers occurs due to competition between mitotic rate γ and subsequent increase of the colony extension on the one hand, and the inability of the boundary to advance fast enough to accommodate the new born cells without reduction of preferred length on the other hand, leading to the following argument.

The colony grows exponentially as long as the mitotic rate γ remains unchanged, which according to eq. (2.12) is the case as as long as the length of a cell doesn't drop below l_{max}. Lets assume a colony in an exponential growth regime. In a small time step dt, the boundary of the colony may only advance as much as the attachment points of the cells on the boundary, that is $\nu dR = \nu v_{max} dt$. On the other hand, in the same time step dt, the number of cells adding to the colony due to division is given by $N\gamma dt$. Thus the colony size increases by $l_{max} N\gamma dt$ and the boundary cells advance by $\frac{l_{max}}{2} N\gamma dt$. From this it is clear that a critical number N_c of cells in a colony exists, above which the advancement of the boundary due to addition of new cells given by $\frac{l_{max}}{2} N\gamma dt$ exceeds the maximum step size of the boundary cells given by $\nu v_{max} dt$. Equalising the two conditions for the front advancement and solving for N gives the critical number of cells $N_c = \frac{2\nu v_{max}}{l_{max}\gamma}$. As the boundary cells adhere to the substrate, addition of new cells leads to a shortening of cells and according to eq. (2.12) a reduction of the mitotic rate. The critical time of the cross over from exponential to subexponential growth may be determined directly from N_c. As the colony grows exponentially as long as $N \leq N_c$, the critical time is proportional to

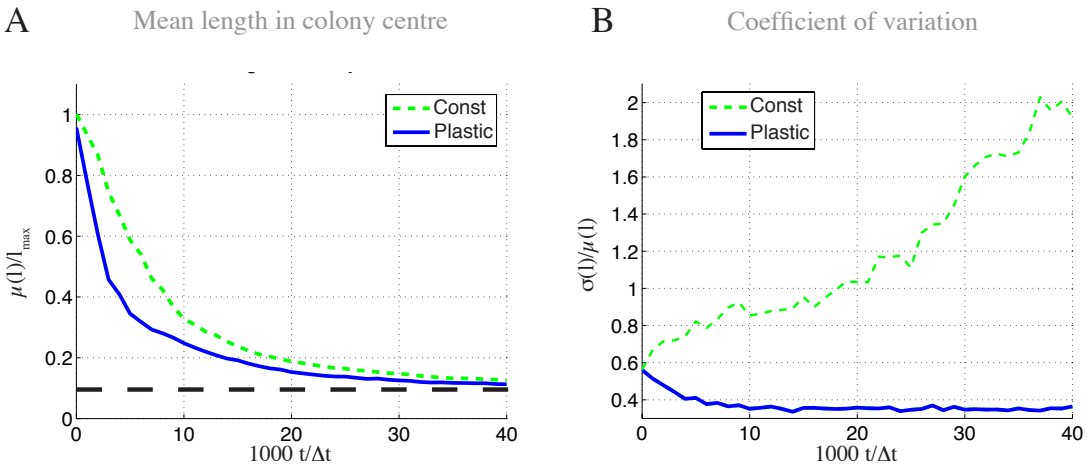

Figure 2.6: Mean cell size and coefficient of variation for plastic and constant cell growth. A) Mean length of cells in colony centre measured in units of maximum length l_{max} against simulation times. Result from stress dependant growth shown as solid blue line and constant growth shown as green dashed line. Dashed black line indicates l_{min}. B) Coefficient of variation for stress dependant growth shown as solid blue line and constant growth shown as green dashed line.

$\gamma^{-1}\log(N_c/N_0)$, thus we have

$$t_c \simeq \frac{1}{\gamma}\log\Big(\frac{\nu}{\gamma}\frac{2v_{max}}{l_{max}N_0}\Big). \tag{2.17}$$

For $t > t_c$, the length of cells will deviate from the preferred length and with it the increase in cell numbers from exponential. Fig. 2.5 B) shows a fit of the approximated cross over time from eq. (2.17) in red to cross over time points identified from simulation as a function of mitotic rate γ shown as green circles. The approximation of the cross over time accurately fits the data points for various mitotic rates γ.

Area distribution

The mean length of cells in the centre of a colony starting at t_c is shown in fig. 2.6 A). Constant size increase is shown as a green dashed line and plastic rest-length

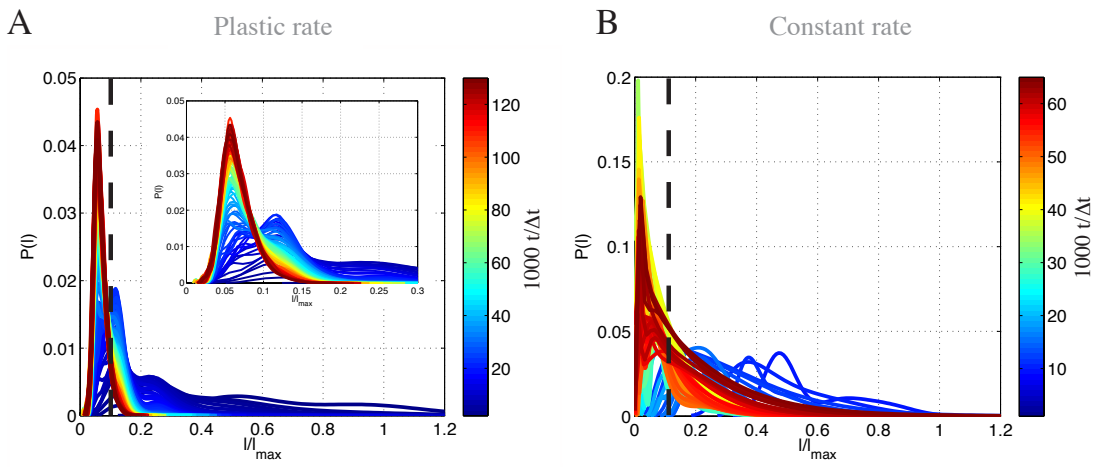

Figure 2.7: Cell size distribution for plastic and constant cell growth. A) Probability density function of cell lengths in colony centre with stress dependent rest-length growth. Colour codes for simulation runs. Dashed black line indicates l_{min}. The distributions evolve from broad at high mean to narrow with mean values below l_{min}. Inset shows zoom on the stationary distribution. B) Probability density function of length of cells in colony centre with constant rest-length growth. Colour codes for simulation runs. Dashed black line indicates l_{min}. Distributions shifting to lower mean with little change in standard deviation are observed.

increase as a solid blue line. In both cases, the initial mean length is approximately l_{max} and asymptotically the mean length approaches l_{min}.

The coefficient of variation of cell lengths $\sigma(l)/\mu(l)$ is shown as a solid blue line for plastic growth and as a dashed green line for constant growth in fig. 2.6 B). In the constant case, the coefficient of variation increases, indicating, that the standard deviation $\sigma(l)$ at least decreases less than the mean value $\mu(l)$. For plastic growth, the coefficient of variation drops, to finally reach a constant value.

The empirical probability density function of the lengths of cells in the colony center is shown in fig. 2.7 A) for plastic growth. The colour code indicates time steps, which lead to a narrowing of the distribution accompanied by a shift of the mean to lower values, converging against the dark red distribution with the majority of cells having rest lengths $l_i(t) < l_{min}$. The case of constant rest-length increase is

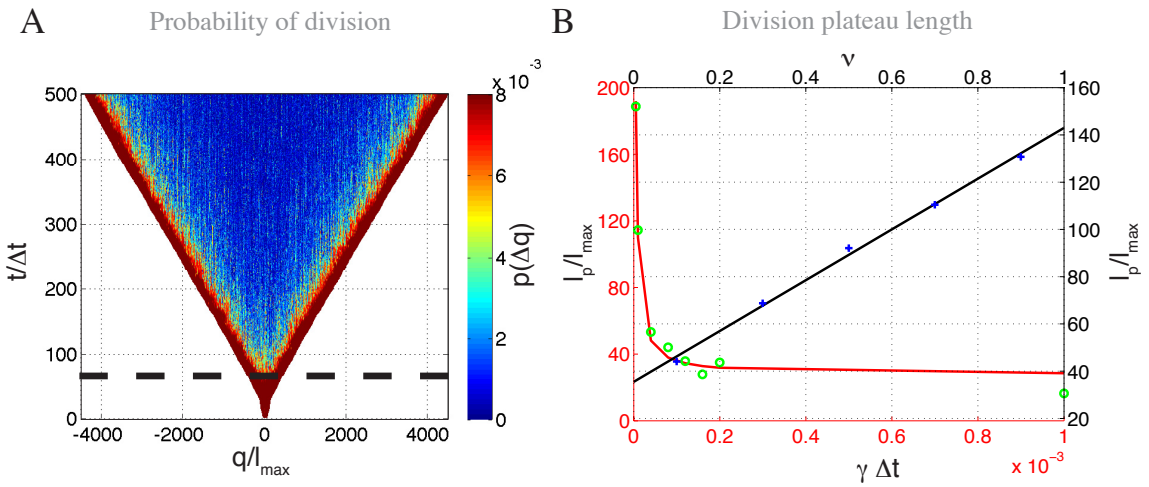

Figure 2.8: Spatial pattern of probability of division in a growing lattice. A) Y-axis shows time measured in simulation time steps and x-axis shows distance around centre of colony measured in l_{max}. Colour codes for $p(\Delta q)$ according to eq. (2.12). Black dashed line indicates critical time of transition t_c. B) Length of plateau of high probability of division l_p/l_{max}. Red line shows γ^1 fit to green circles from various $\gamma\Delta t$ obtained by simulation. Black line shows a linear fit to blue crosses for various ν obtained by simulation.

shown in fig. 2.7 B). One observes a sequence of distributions shifting to lower values with similar standard deviations. In the long term this case also converges against a steady distribution.

Spatial division patterns of growing colonies

The spatio-temporal pattern of the division probability $p(\Delta q)$ from eq. (2.12) of cells to divide around the centre of the colony indicated by 0 is shown in fig. 2.8 A). The colour codes for the probability of a cell in the colony to divide, where dark blue stands for division arrest and dark red for maximum probability. Initially, the entire colony has the same probability to divide until the critical time t_c is reached, where the colony enters the subexponential regime indicated by a black dashed line. For $t > t_c$ cells in the centre of the colony have a low probability of division compared

to cells on the boundary. Here a narrow band characterised by a high probability of division builds up. Note that the above result is essentially the same for both scenarios of the increase of the intrinsic length. We refer to the state of cells in the centre of the colony with high density and low division probability as dense.

The extension of the plateau of high probability of division may be deduced as follows. Figure 2.8 A) shows that after the time of transition, the rest length of cells in the centre of the colony becomes reduced, and divides the growing colony in two halves, with high proliferation rate at its respective ends. At time of cross over t_c, the two bands of high proliferation rate are still joined. Thus from knowledge of the critical number of cells in the colony when subexponential growth starts, we can get the size of the band, as approximately half the size of the colony with N_c cells that have the rest length l_{max}. In the derivation of eq. (2.17), we found $N_c = \frac{2\nu v_{max}}{l_{max}\gamma}$ and thus the length of each plateau l_p scales as

$$l_p \simeq \frac{\nu v_{max}}{\gamma}. \tag{2.18}$$

A fit of this scaling law of the plateau length against various γ and ν is shown in fig. 2.8 B), confirming the inverse relation to γ and the linear relation to ν.

The different scenarios for the growth of the rest length result in different distributions of cell lengths, which is also reflected in the stress present in the lattice, as shown in fig. 2.9 A) in case of constant rest-length increase and B) for the plastic scenario. For constant growth, cells in the centre of the colony rapidly enter a state of compressive stress, as the length available for each cell is much smaller compared to intrinsic length. Moving out towards the boundary, the compressive stress reduces and changes into a tensile stress, due to the outward directed motion of the boundary cells. For plastic growth, cells in the centre of the colony are in an almost stress free state, indicating that the cells length matches the corresponding rest-length. On the boundaries, a tensile stress is observed.

Measurements of the physical forces during colony growth revealed tensile stress present not only at the leader cells but also deep in the colony with no compression observed [Trepat09]. In both growth cases, the colony is under tensile stress on the

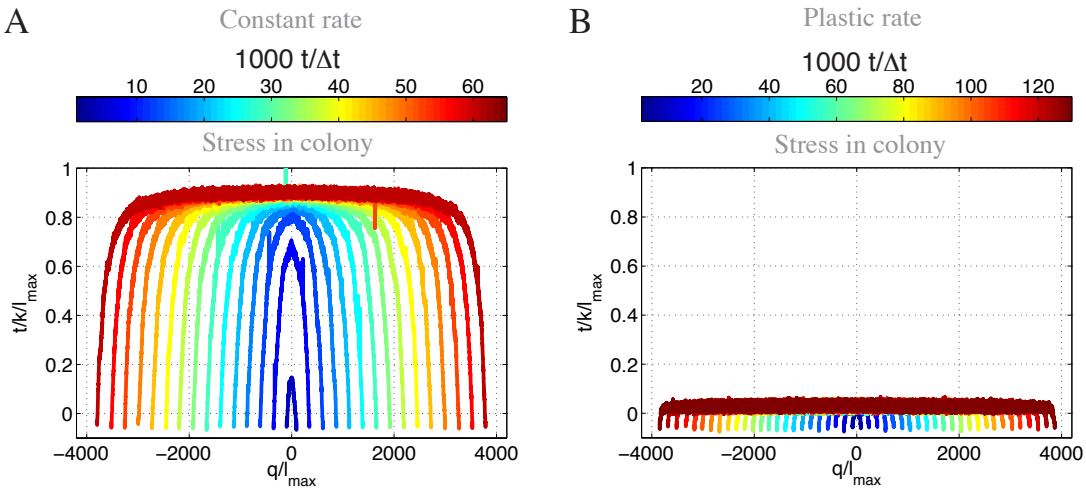

Figure 2.9: Stress distribution for plastic and constant cell growth. A) Spatial distribution of stress in constant growth model measured in units of kl_{max} round centre of colony. Colour code indicates temporal evolution. B) As A) with stress dependent growth.

boundary, whereas in the centre, the linear growth case results in a highly compressive state in contrast to the nearly unstressed cells in the centre of a colony with plastic growth. Comparing the measured empirical pdf of areas shown in fig. 2.3 B) as well as the coefficient of variation to the predicted results shown in fig. 2.7 and fig. 2.6 B) respectively, it is immediately clear, that the constant growth of the rest length deviates more from the observed data than the plastic growth of cells, which is in good agreement with measurements.

2.4 Mechanical aspects of epithelial to mesenchymal transition

In the previous section, we have studied the morphological transition and subsequent formation of an epithelium. Cancers have the ability to undergo a transition back to a mobile state, characterised by mesenchymal properties at the forefront of the

moving cancer. This process is called EMT [Baum08]. Here, we want to study this reversal, by growing a colony against a barrier and wait until it has undergone contact-inhibition of proliferation. From classical wounding experiments, it is known that cells can re-enter the cell cycle, when the barrier becomes removed [Fenteany00, Nikolic06, Poujade07], allowing to monitor the dynamics of EMT. Studying the role of proliferation in the advancement of the boundary, requires precise understanding of the spatio-temporal dynamics of the division pattern. What drives the epithelial to mesenchymal transition and reversal of contact inhibition, i.e. which cues make the cell synthesize DNA is a crucial step in the determination of such proliferation patterns and thus of outstanding interest.

Once the tissue has grown dense, cells cease to divide and enter $G0$-phase. Upon release of the PDMS barrier, the tissue invades the free space accompanied by cell proliferation [Poujade07]. Cell division can be easily identified by monitoring the dynamics of a nuclear marker, such as $H2A - RFP$. Here we want to have a closer look at the cell cycle re-entrance. A novel dynamic read-out of cell cycle state called fluorescent ubiquination-based cell cycle indicator (FUCCI) [Sakaue-Sawano08] allows to separate the five steps of the cell cycle $G0$, $G1$, S, $G2$ and M as shown in fig. 2.10 A) into a set during $G0/G1$ separated from $S/G2/M$-phase. Furthermore, it provides a good proxy for the contact inhibition of proliferation of the tissue as cells in $G0$ appear in a different colour from cells in $S/G2/M$.

An MDCK cell line expressing the FUCCI cell cycle marker is shown in fig. 2.10 B). Cells cycling through $G0$ or $G1$ express an RFP and upon entrance to S-phase upregulate a GFP and down regulate the RFP. This results in a short overlap of the flurophores at the beginning of S-phase followed by a high GFP signal throughout the rest of S and $G2$ until the end of M-phase, as indicated in the schematic at fig. 2.10 A).

The temporal evolution of a scratch wound essay with the FUCCI -MDCK cell line is shown in fig. 2.11 A1)-A4). The initial condition comprises cells almost exclusively in $G0/G1$-phase, i.e. in the state of contact inhibition of proliferation, grown against a PDMS barrier, which is ripped off of the dish at the start of the experiment fig. 2.11 A1). After 40 hours, the front has advanced into the free space

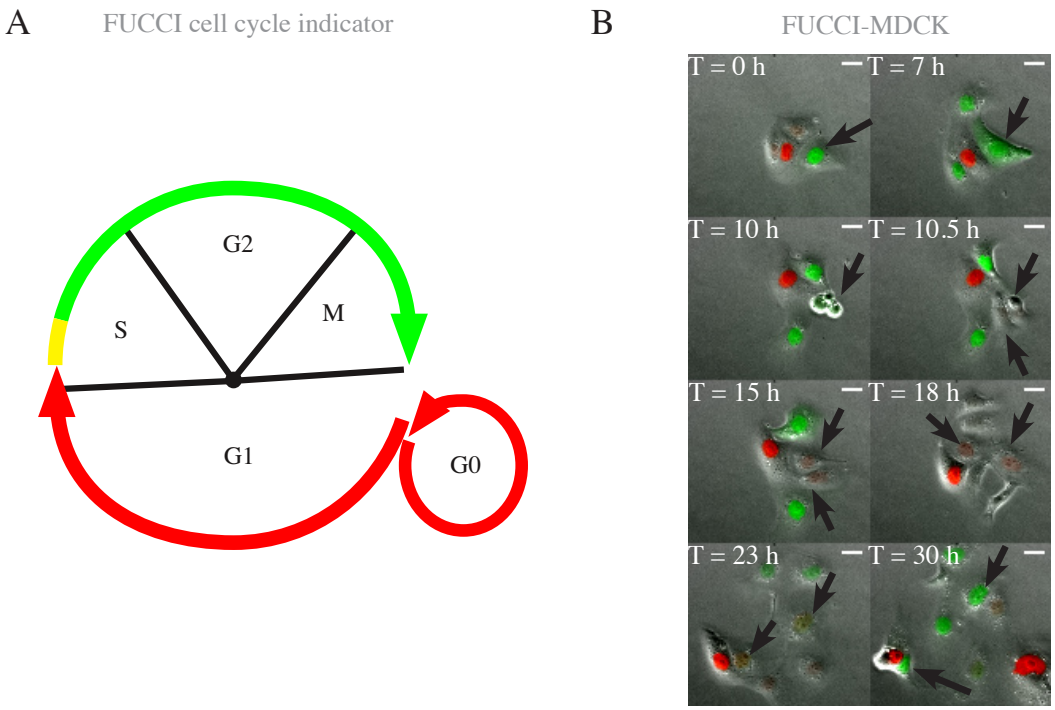

Figure 2.10: Dynamic cell cycle read-out. A) Cell cycle as labelled by the FUCCI marker. Cells in $G0$ and $G1$-phase express red flurophores. Upon entrance to S-phase, green flurophores begin to be expressed and, whilst red flurophores become down regulated, resulting in a transition of yellow to green during S-phase. Continuing through S over $G2$ until the end of M-phase before nuclear break down, green flurophores are expressed. Between end of M-phase and start of $G1$ of the daughter cells, no signal is detected. B) Stills of MDCK cells expressing the FUCCI cell-cycle marker in the nucleus. Scale bar 10 μm. Dividing cells show no signal and are distinguished from the other cells by a bright signal in the transmission channel. Black arrow indicates the position of a cell along the cell cycle and the position of daughter cells after division.

and a large number of cells entered S-phase, especially in the vicinity of the boundary as observed in fig. 2.11 A2). Groups of cells forming finger like structures entering the free space, as observed in previous studies [Poujade07], are also present in this case. After 80 hours, the band of cells in $S/G2/M$-phase has increased its extension, mainly restricted to the newly covered space. The leading edge becomes increasingly ruffled. It continues expanding and after 120 hours left the field of view. The former

wound is then covered by cells in $S/G2/M$-phase, where also a number of cells in $G0/G1$-phase appeared.

The temporal evolution of the boundary advancement into open space is better understood in form of a kymograph showing the fluorescent signal over time along a line as shown in fig. 2.11 B). Invasion is initially approximately parabolic, as previously observed, but then switches to a constant boundary velocity. Entrance to S-phase as indicated by the colour-switch of nuclei from red to green is largely restricted to newly covered parts, with little back propagation into the tissue. As time advances, cells far behind the tissue stop moving, divide and enter $G0/G1$-phase, whereas cells in a band of approximately 400 μm remain largely in $S/G2/M$-phase, as indicated by the schematic in fig. 2.11 C).

The given qualitative description of the scratch wound essay must be cast into a quantitive form, for further understanding and hypothesis testing. Therefore, we developed a computer based segmentation routine for the nuclei as described in the appendix E. Fig. 2.12 A1) shows an example segmentation of the original image shown in fig. 2.12 A). During the segmentation of individual nuclei, the state of a nucleus is noted. From the centroids, a Voronoi tessellation is constructed used to obtain a proxy for the area covered by an individual cell. Thus for each object, we have a set of numbers (S, C, A, t), describing the state in the cell cycle $S \in \{G0/G1, S/G2/M\}$, the position of the nucleus $C = (x, y)$, the area covered by the cell A and the time of the observation t.

Signal for S-phase entrance scales with boundary velocity.

Comparing the images of nuclei at the boundary and in the bulk after 40 hours shown in fig. 2.12 A) and B) respectively, it is clear that cells on the boundary have an increased cross-section as compared to bulk cells. A quantification of the area plotted against the x-coordinate of the nucleus in the image, shown in fig. 2.12 C) for the boundary and E) for the bulk reveals that the area covered by boundary cells is increased by a factor of 2 compared to cells in the bulk, which is similar to the area of boundary near cells at the beginning of the experiment (see fig. 2.15 A)).

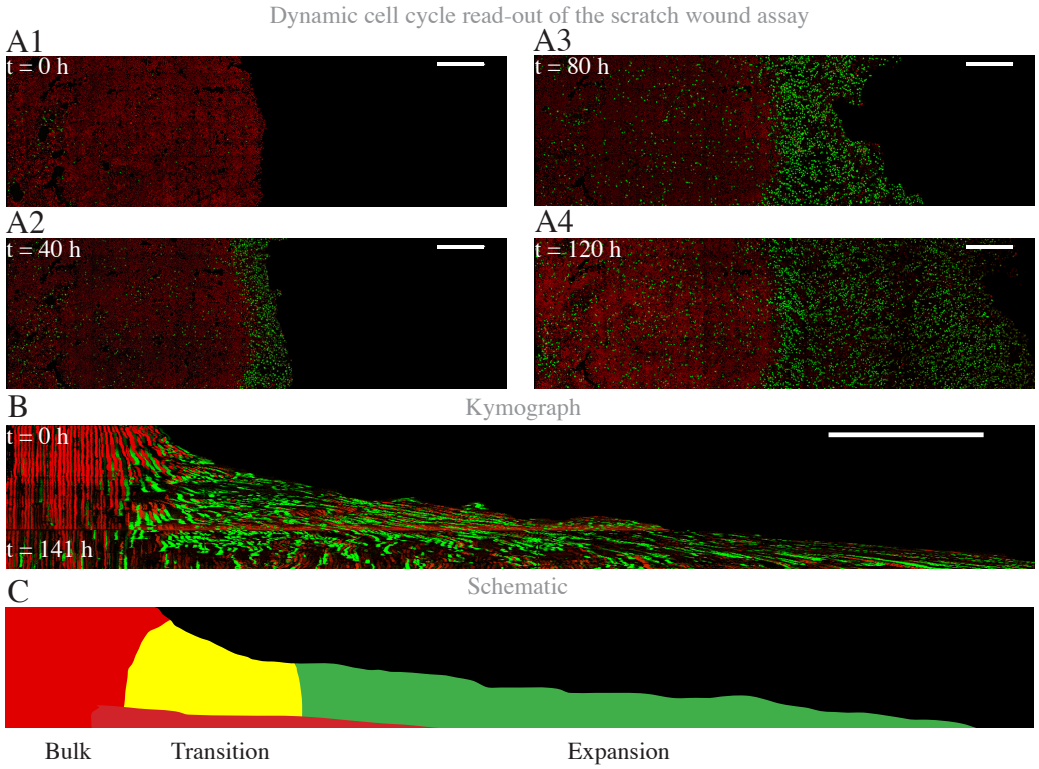

Figure 2.11: Cell cycle progression upon boundary release. A) Stitched stills from 30×9 image frames showing scratch wound essay with MDCK cells expressing the FUCCI cell cycle marker. Scale bar 500 μm. A1) $t = 0$ h: Cells in a state of contact inhibited of proliferation. The majority of cells is in $G0/G1$-phase. Black space indicates free space after removing PDMS barrier. A2) At $t = 40$ h, the tissue invades the free space. Cells around the boundary begin to express green fluorescence indicating advancement to S-phase. A3) At $t = 80$ h, the boundary has continued to advance. More cells advanced to $S/G2/M$-phase. A4) At $t = 120$ h, the boundary is largely out of the frame. An increasing number of cells in $G0/G1$ is observed among cells in $S/G2/M$-phase. B) Kymograph of the scratch wound essay showing time running from $t = 0$ h at the top to $t = 141$ h on the bottom of the y-axis and the normal direction of the initial wound along the x-axis. A melting of the boundary into the free space and switch of cells from $G1$ to S-phase is observed. At later times close to 141 h, cells away from the boundary become immobile and then divide. C) Schematic of the kymograph separated into the bulk zone shown in red where most cells are in $G0/G1$-phase, a transition zone from $G1$-phase to S-phase in yellow and an expansion phase of the tissue shown in green with most cells in $S/G2/M$-phase.

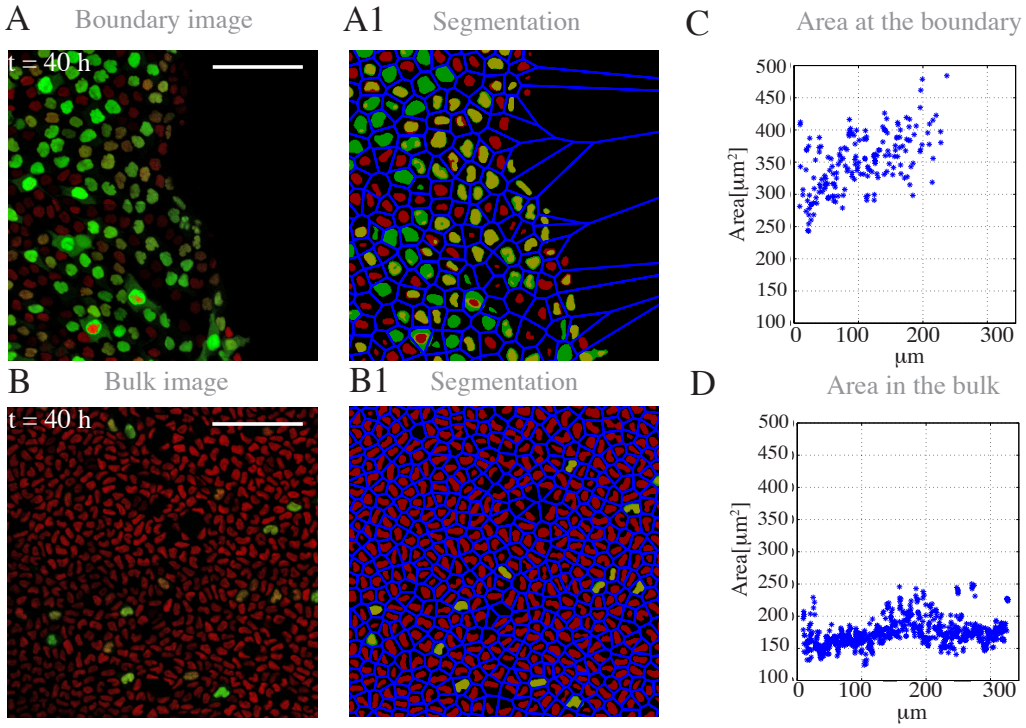

Figure 2.12: Boundary melting. A) Close-up on cells on the boundary. 4 stitched frames down-sampled by factor 2 are shown. Scale bar is 100 μm. A1) Segmentation of A) with voronoi tessellation based on centroids of nuclei. B) Close-up on cells in the bulk. Scale bar and down-sampling as in A). B1) as A1) for B). C) Area of polygons from voronoi tessellation against X-position in A). D) As C) for B).

Thus the tissue melts from the boundary into the open space.

To obtain the velocity of cells, we used nearest neighbour tracking to reconstruct the track of individual cells. Subsequently we approximated the velocity of a cell as the distance travelled between following time-points divided by the duration of one time step $v \approx \frac{C(t)-C(t-1)}{\Delta t}$. Fig. 2.13 A) shows example tracks of cells along the first 40 hours in a window of 500×500 μm around the leading edge, where the colour indicates the state in the cell cycle. One observes that the cells on the boundary move into the free space and enter S-phase. In contrast, cells in the bulk are fluctuating around their initial position and largely remain in $G0/G1$-phase.

The velocity of the leading edge is obtained from the velocity of individual cells

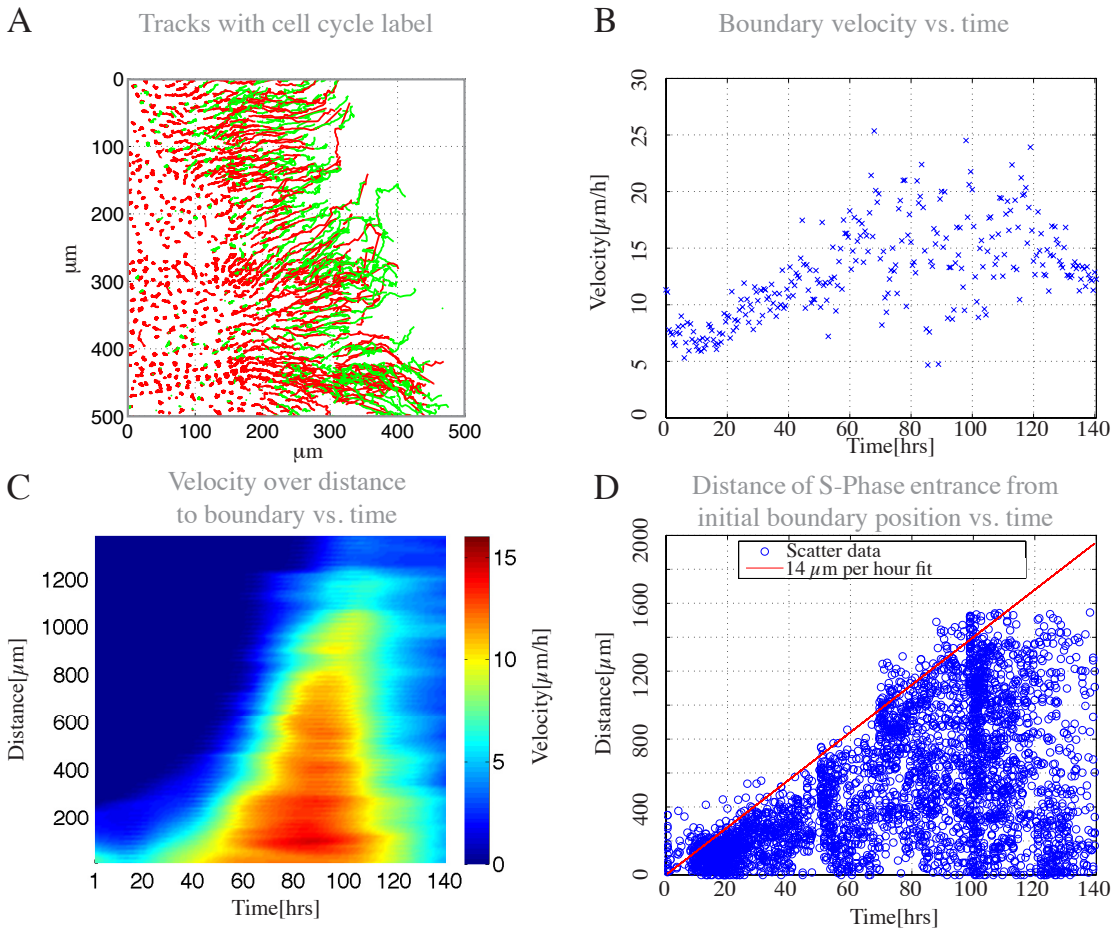

Figure 2.13: Quantitative characterisation of invasive migration. A) Tracks of segmented image, with state of nucleus along the track colour coded. B) Boundary velocity against time. C) Velocity over distance to boundary versus time. For each nucleus and time point, the distance to the boundary and the averaged velocity of all nuclei at this distance is noted and the averaged velocity of all nuclei at this distance is plotted. Colour code shows velocities around 15 $\mu m/h$ in red and 0 $\mu m/h$ in dark blue. D) Distance of entrance into S-phase from initial boundary. Each spot shows the distance to the initial boundary of a nucleus entering S-phase at a given time.

on the boundary of the tissue towards the wound. Fig 2.13 B) shows the averaged velocity of boundary cells against time. Consistent with previous findings, the initial velocity increases linearly, indicating a constant acceleration of cells. After 60 hours,

this linear increase is then replaced by an approximately constant velocity fluctuating around 15 $\mu m/h$.

As the boundary advances, an increasing number of cells behind the leading edge also move towards the open space. Fig. 2.13 C) shows that with time, a plateau of constant high velocity around 15 $\mu m/h$ builds up from the leading edge, lasting up to 1000 μm deep into the tissue. After about 100 hours, the part in the tissue between 400 and 1000 μm away from the boundary simultaneously drops the velocity and soon reaches a halt, consistent with observations based on the kymograph.

Position of S-phase entrance with respect to the front as a function of time provides a read-out for the propagation of the proliferation signal through the tissue, triggering advancement in the cell cycle. Fig. 2.13 D) shows that the distance to the leading edge of cells entering S-phase increases with time. The red line is a guide for the eye showing that the signal for entrance into S-phase is travelling at a velocity of 14 $\mu m/h$ through the tissue, roughly coinciding with the velocity of the boundary.

The data suggests that not only the boundary moves to close the wound but also cells deep in the tissue move in the direction of the wound to cover the free space. In the long term, a plateau of cells with velocities fluctuating around 15 $\mu m/h$ builds up. As the cells move, they advance in cell cycle and the position where cells decide to do so can increase in distance to the boundary at the same velocity as the boundary moves forward. In the next section, we will study the role of cell proliferation in the advancement of the boundary.

2.4.1 Dissecting the role of cell division in front propagation

As observed in the previous section, the tissue melts into the free space after wounding, cells at the boundary increase the area they cover. This is one possible factor playing a role in boundary advancement. Another factor is given by cell proliferation, as daughter cells can grow, and eventually require more space. We decided to uncouple the melting process from proliferation by treating the tissue with a drug that blocks cell division via the MAPK signalling pathway, prior to wounding [Goueli98]. After wounding, the tissue was kept in the blocked state for 28 hours, which marked

the point of drug washout.

Fig. 2.14 A) shows a kymograph of a wounded tissue treated with MEK cell cycle blocker. The tissue invades the free space and after some time slows down significantly. After drug washout, the tissue boundary initially remains at its position, to then rapidly switch to a constant motion. This is accompanied by a switch in cell cycle also deeper in the tissue.

A quantification of the boundary velocity based on tracking data of boundary cells is shown in fig. 2.14 B) as red circles. Acceleration of the boundary similar to untreated tissues is followed by a slow down of cell velocities. After drug washout, the cells remain at the low velocity and then within one hour switch to a velocity that is not to be distinguished from the velocity of an untreated tissue shown as reference.

The initial acceleration of the boundary is hardly followed by the bulk as shown in fig. 2.14 C). After drug washout, accompanied by the switch in motion of the boundary, the bulk also starts to move, as can be seen in fig. 2.14 C), where a plateau of velocities similar to what is observed in the untreated case begins to build up.

Advancement of cells into S-phase has lost the correlation to the boundary velocity observed in the WT but still seems to be restricted to a position at some distance of the boundary, as can be seen in fig. 2.14 D). After start of the experiment, a few cells enter S-phase, due to incomplete cell cycle blockage. Here the entrance is restricted to close proximity of about 100 μm to the boundary and after washout of the drug, rapidly cells at a distance as far as 650 μm enter S-phase.

Blocking cell cycle progression shows that without proliferation the tissue boundary is unable to advance beyond a point it can reach by melting into the open space. This suggests that the acceleration is driven by cell expansion and motion into the free space but not proliferation. On the other hand, this expansion of the boundary can only accelerate the leading edge until a state is reached where the boundary seems to be held back by the bulk, manifested in a significant reduction of the boundary velocity. Upon washout of the drug and subsequent reinstallation of cell division, the slow leading edge makes a leap to velocities reached at the same time by an

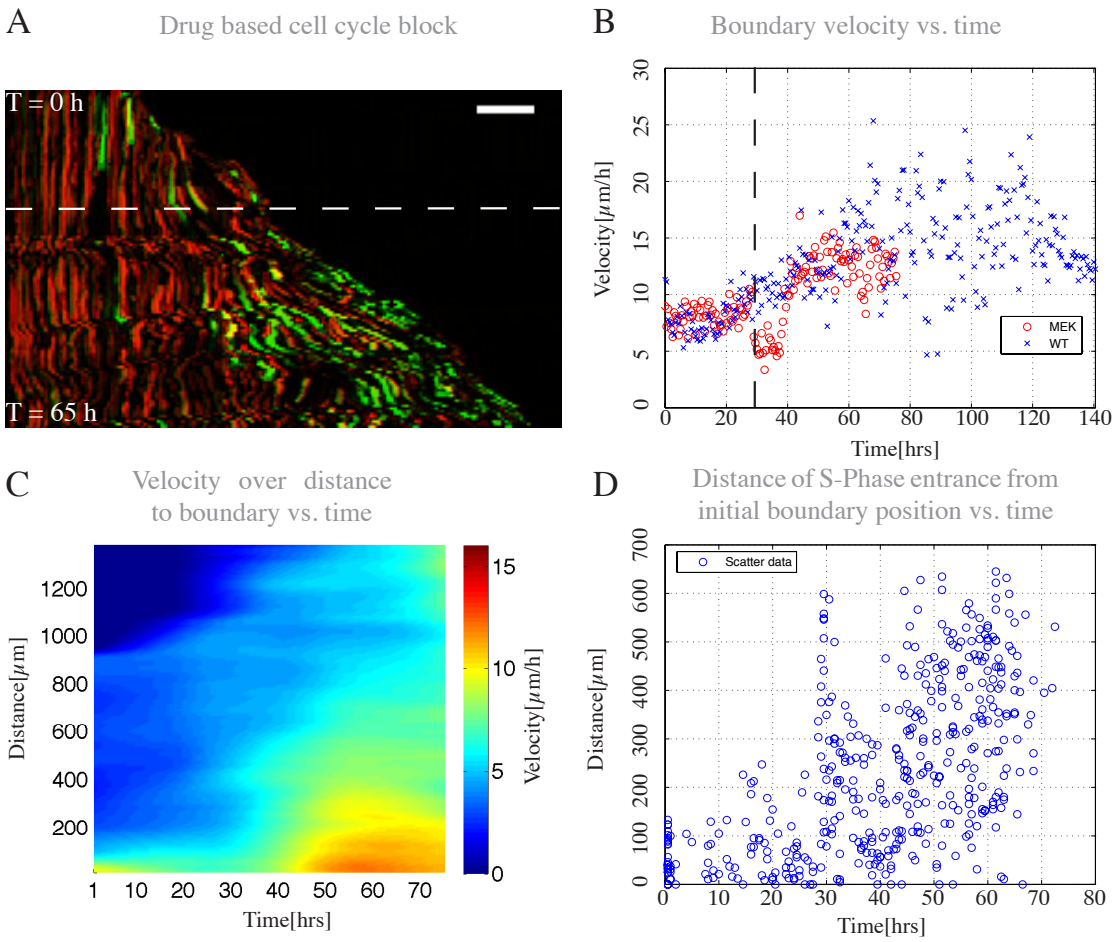

Figure 2.14: Dynamics of boundary release with cell cycle blocker. A) Kymograph of scratch wound experiment with MEK cell cycle blocker leading to proliferation arrest. Time of drug washout is indicated by white dashed line. Scale bar is 100 μm. B) Boundary velocity of blocked case shown as red dots, time of drug washout indicated by black dashed line. Wild type case is shown in blue crosses as reference. C) Velocity over distance to boundary versus time for drug treated tissue. For each nucleus and time point, the distance to the boundary and the averaged velocity of all nuclei at this distance is plotted. Colour code shows velocities around 15 $\mu m/h$ in red and 0 $\mu m/h$ in dark blue. D) Distance of entrance into S-phase from initial boundary. Each spot shows the distance to the initial boundary of a nucleus entering S-phase at a given time.

untreated tissue. Thus proliferation seems to be necessary for the tissue to reach the maximal crawling velocity of the boundary. In the next section, we will investigate the melting of the boundary in some more detail.

2.4.2 Characterising S-phase entrance

Our previous analysis showed that not only the boundary velocity increases, but also gradually a plateau of cells characterised by high velocity directed towards the wound is built-up as can be seen in fig. 2.13 C). As observed in fig. 2.12 with time, the average area of cells on the boundary increases compared to the area of cells in the bulk.

After releasing the boundary constraint, the areas of boundary cells begin to increase, whereas deeper in the tissue, cell areas remain low as can be seen in fig. 2.15 A). As time advances, due to boundary advancement, cells at an increasing distance of the boundary also increase their area, leading to a reduction of density from the leading edge. Similar to the plateau of cells with high characteristic velocity, a plateau of cells characterised by high area emerges. Also after about 100 hours, cells density becomes simultaneously increased over long distances, as can be seen by the reduced area. Comparing the velocity plot to the area plot, one observes that in the WT case, the area and the velocity plateau coincide to a large extend and cells are characterised by both increased outbound velocity and low density.

The area distribution of cells in a tissue that is chemically blocked in cell cycle at the $G1/S$-interface is shown in fig. 2.15 B). Area of individual cells behind the boundary increases gradually and after drug washout the melting continues until a plateau of cells with high area of almost constant length emerges. Stationary waves of high and low density with a wavelength of approximately 200 μm emerge behind this plateau, also observed in the long term dynamics of the wild type tissue.

As observed from the images in fig. 2.11 as well as fig. 2.13 D), most of the cells entering S-phase are located outside of the initial collective before wounding. This also coincides with the positions, where cell density is low as discussed above. Fig. 2.15 C) shows the empirical probability density function of areas of cells in $G0/G1$-

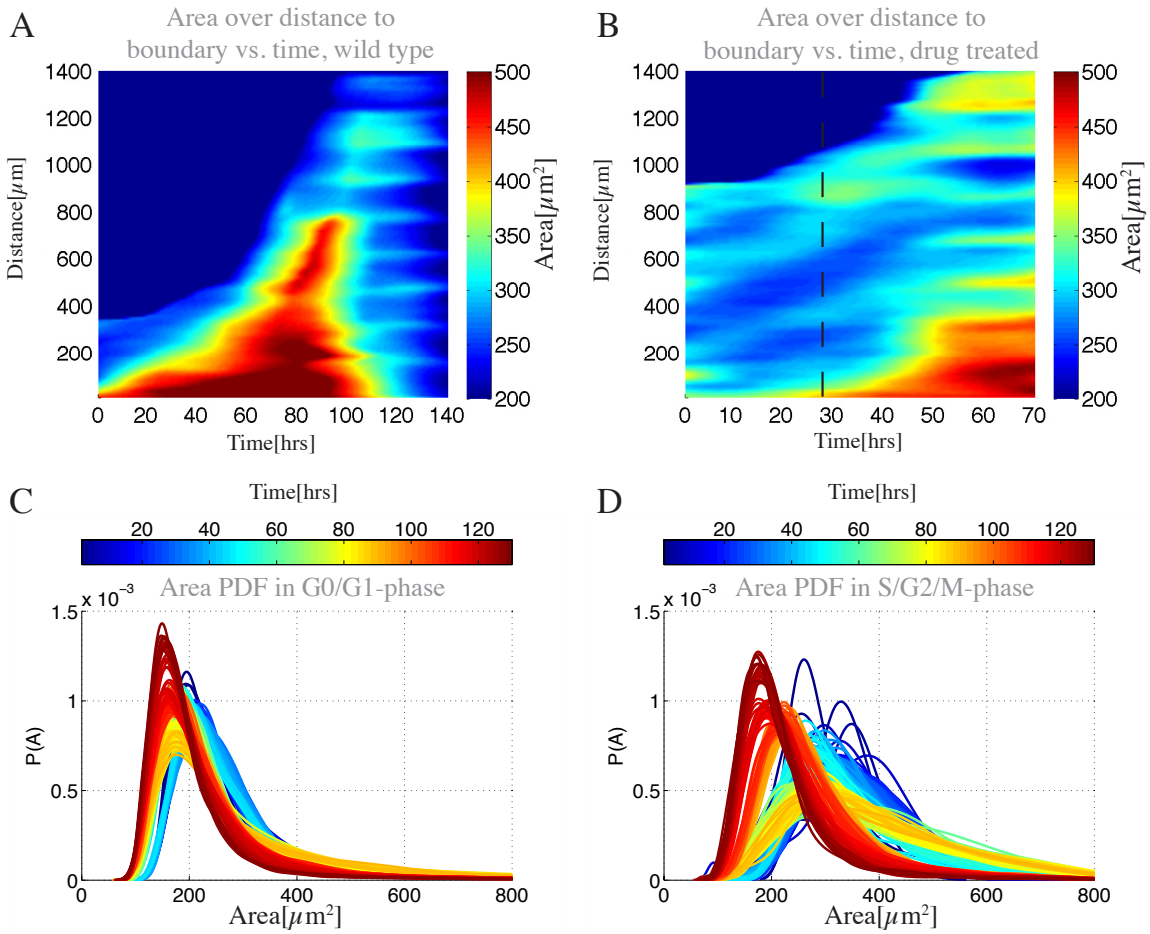

Figure 2.15: Quantitative characterisation of tissue melting. A) Area over distance to boundary versus time. For each nucleus and time point, the distance to the boundary and the averaged area of all nuclei at this distance is plotted. Colour code shows areas around 500 μm^2 in red and 200 μm^2 in dark blue. B) as A) for cell cycle blocked tissue. Black dashed line denotes time of drug washout. C) Empirical PDF of area of cells in $G0/G1$-phase. Colour codes for time. D) Empirical PDF of area of cells in $S/G2/M$-phase. Colour codes for time.

phase taken from a field starting 200 μm behind the original wound and into the open space. The median of the distribution fluctuates around 200 μm^2, the mean around 270 μm^2. Towards the end of the experiment the distribution converges again

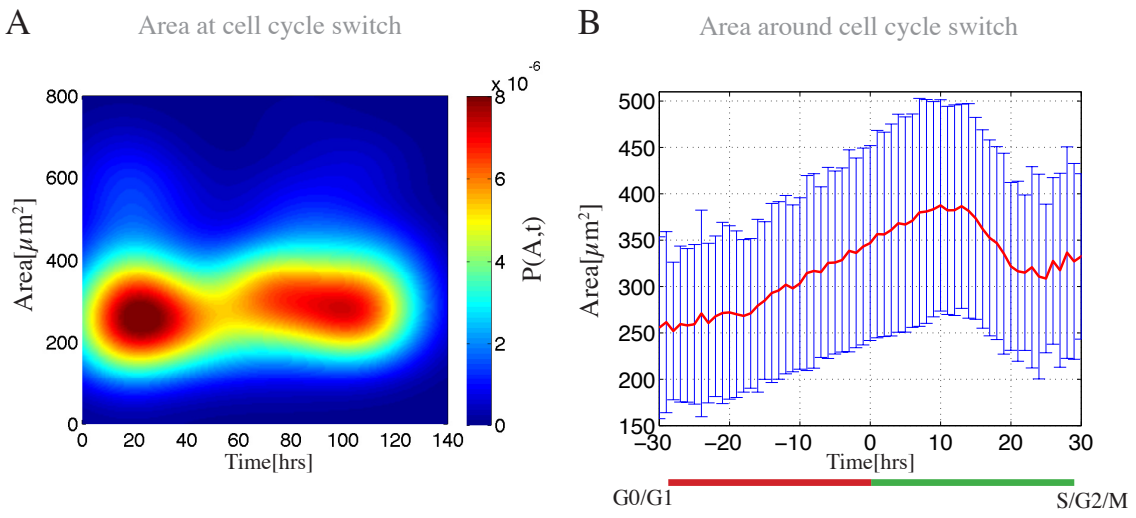

Figure 2.16: Quantitative characterisation of cell cycle advancement. A) Area distribution of cells at entrance of S-phase against experiment time. B). Average area of cells against time shifted around cell cycle switch. For each observation, time is shifted, such that 0 indicates entrance to S-phase, i.e. switch from red to green. Negative time values correspond to times in $G0/G1$. Error-bar denotes standard deviation around mean.

to the stationary distribution of bulk areas.

The area distribution of cells in $S/G2/M$-phase for the same field of view as above is shown in fig. 2.15 D). Compared to cells in $G0/G1$, the distribution is shifted to greater areas already at the start of the experiment, continuing to increase for 20 hours. Then, the median fluctuates around 350 μm and the mean around 370 μm. Towards the end of the experiment, the distribution again becomes narrower approaching a distribution with median below 200 μm^2, accompanied by a reduction of the number of cells in $S/G2/M$-phase due to division.

The observed increased area of cells in $S/G2/M$ compared to cells in $G0/G1$ lead us to study the area of cells along the track, as they switch from $G1$ to S-phase. The distribution of areas at the time of S-phase entrance against time is shown in fig. 2.16 A). At all recorded time points, the distributions median is found around 300 μm^2 and the mean is located at about 350 μm^2.

The average area of cells along the cell cycle aligned in time, such that 0 is defined

as the time of S-phase entrance is shown in fig. 2.16 B). As cells begin in $G0/G1$ characterised by negative times, area increases linearly by a rate of $4\mu m^2/h$ and upon S-phase entrance a mean area of 350 μm is observed. As the cells continue in S-phase, the area continuously increases, reaching a maximum after about 10 hours past S-phase entrance.

The data supports an area check-point characterised by a critical area that cells have to cover in oder to enter S-phase. This is independent of the initial melting of the tissue, as the area distribution of cells entering S-phase undergoes little change. It also explains why the distribution of cell areas in $G0/G1$-phase is concentrated around lower areas than the distribution of cells in $S/G2/M$, as cells at the high end of the $G0/G1$ area distribution are more likely to switch to S-phase. Furthermore, it is consistent with the simultaneous S-phase entrance of cells after washout of cell cycle blocker. Cell density in the tissue is reduced enabling cells to overcome the area checkpoint. Cells entering S-phase on average continue growing at the same rate as before S-phase entry and eventually divide. In the next section, we will study cell areas and the time spent in M-phase.

2.4.3 Characterising M-phase completion

Motivated by the note of a fast progression of cells through $S/G2/M$-phase in the blocked tissues after drug washout, we studied the time cells spend in $S/G2/M$-phase until division, as shown in fig. 2.17. In all cases, the two dimensional empirical probability density function of observing a cell at a given distance to the boundary taking a given amount of time through $S/G2/M$ is shown.

In the case of wild type experiments, shown in fig. 2.17 A), two different clusters of cells are identified, characterised by the different time taken to complete the cell cycle after synthesis. One group is focused around 6 hours, showing no correlation with the distance to the front. The other group is focused around 17 hours and has a linear correlation with the distance to the boundary, where cells closest to the boundary take 15 hours and cells at 300 μm distance take up to 20 hours.

A separation of the tracks into a group of cells already observed in the first 20

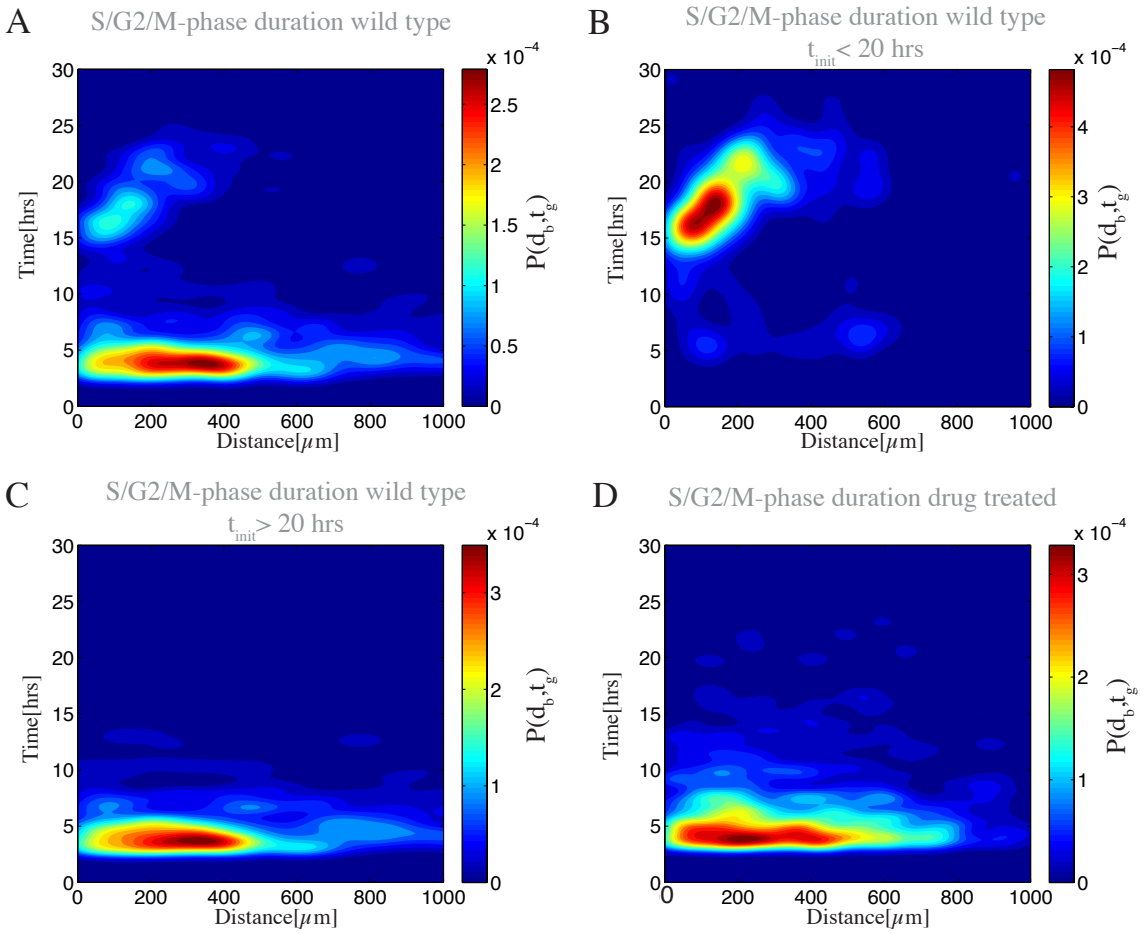

Figure 2.17: Quantitative characterisation of cell cycle duration after synthesis. A) Time spent in $S/G2/M$-phase in hours against distance to the boundary in μm. Colour codes for the empirical probability of cells spending a given time in $S/G2/M$-phase at a given distance. B) As A) but exclusively cells present from the start of the experiment. C) As A) but exclusively cells with first observation $t > 20$ hours. D) As A) for cells in tissue after washout of MEK cell cycle blocker, preventing division.

hours and a group of cells with first observation after more than 20 hours is shown in fig. 2.17 B) and C). The distribution seems to be split into two time-halves, suggesting that the cluster with $S/G2/M$-phase duration showing linear correlation with the distance to the boundary is formed by cells present at the beginning of the

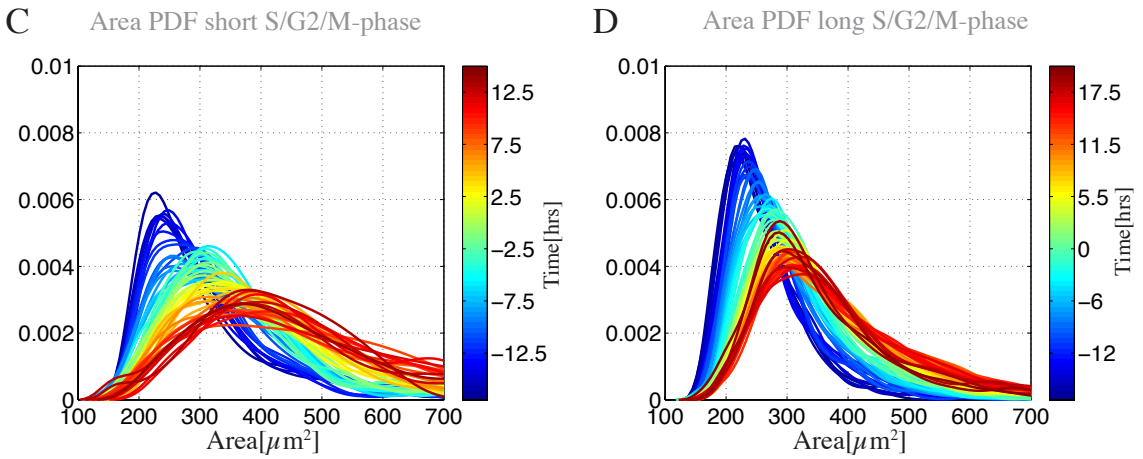

Figure 2.18: Cell cycle duration after synthesis is correlated to cell size. A) Empirical PDF of area of cells passing through $S/G2/M$-phase in less than 13 hours. Colour codes for time spent in $S/G2/M$-phase, with 0 indicating entrance into S-phase. Negative time values correspond to times in $G0/G1$. B) Empirical PDF of area of cells passing through $S/G2/M$-phase in more than 13 hours. Colour coding as A).

experiment, whereas the cluster showing no correlation is formed by cells appearing later, very similar to the observed pattern of the division inhibited tissue shown in fig. 2.17 D). Here, the majority of cells takes 6 hours to complete mitosis after entering S-phase, with little correlation to the distance to the boundary.

The two clusters of cells characterised by different $S/G2/M$-phase duration are further analysed, by separating the tracks of cells into a fast cluster of cells, defined by taking less than 15 hours to finish M-phase and a slow cluster containing the rest. Fig. 2.18 A) shows the area distribution of the fast cluster of cells, where the colour code denotes the time around S-phase entrance, which serves as a reference point $t = 0$. Negative times again correspond to $G0/G1$ and positive to $S/G2/M$-phase. The median of the cell distributions rapidly shifts to increasing areas, cells enter S-phase and the distributions median continue to shift, until cells divide.

For the slow cluster of cells shown in fig. 2.18 B), the initial shift of the distributions median towards increasing areas is also observed, until the cells enter S-phase. Subsequently, in contrast to the fast cluster, the distributions median remains closer

to the median of the distribution observed at S-phase entrance.

Taken together, this suggests a second area check point in the cell cycle, required for M-phase completion. Cells at low density pass faster through M-phase than cells at high density. It also explains the increasing duration for $S/G2/M$-phase with increasing distance to the boundary, observed at the beginning of the experiment, as the tissue gradually melts into the open space. The loss of correlation to the distance from the boundary, observed with cells present at later time points may also be understood as those cells have more space to cover. A Similar argument holds for the inhibited tissue.

2.4.4 Simulation of boundary release of dense adherent cells

We have observed, that once cells in a tissue have undergone contact inhibition of proliferation, they can re-enter the cell cycle and found that the boundary advances with a linear velocity. Chemical induced cell cycle blockage results in an altered boundary advancement dynamics, where after melting, the boundary slows down. Upon release of the blocker, many cells in the tissue simultaneously advance in cell cycle and the boundary rapidly increases its velocity to the wild type velocity.

We use the description of motile adherent cells developed above and restrict to the plastic growth of cells given by eq. (2.16). To generate the initial condition for the boundary release, we consider a lattice of a few one hundred cells each with initial intrinsic length $l(0) = l_{max}$. Division is assumed to be size dependant as describe in the discussion of eq. (2.12). The boundary against which the lattice grows is represented by the constraint that the total force acting on boundary vertices of the lattice vanishes. This results in a fixed position of the boundary with cells on the inside free to move and corresponds to cells seeded at high density, covering the entire free space. Fig. 2.19 A) shows the initial lattice evolving with time. The boundary remains at the same position and the probability of cells to divide reduces with increasing number of proliferation steps resulting in a lattice with $p(\Delta q_i) = 0$ for all cells i.

In order to understand the contribution of cell division to the boundary advance-

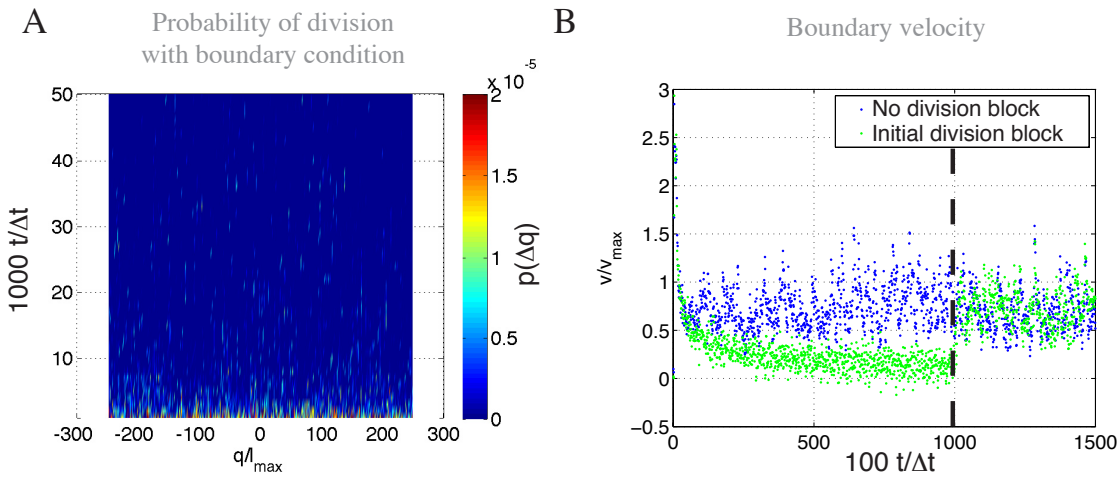

Figure 2.19: Boundary velocity of growing and blocked lattices. A) Probability of division. Colour codes for probability of division, blue indicating low and red high. x-axis shows position measured in units of l_{max} and y-axis shows time measured in simulation steps. B) Velocity of boundary after release of constraint on one end. Blue spots are from simulation with no change in mitotic rate and green spots from initially blocked mitotic rate $\gamma H(t - t_{block})$, with $t_{block}/\Delta t = 10^6$.

ment, we study two different scenarios of cell division after boundary release. The blocked case, where cell cell cycle progression is arrested, even if the probability of division according to eq. (2.12) doesn't vanish, reflecting the cell cycle blocker in the experiment. In this scenario, for times $t \geq t_{block}$, the division blockage becomes released, reflecting the washout of the chemical in the experiment. The alternative scenario is the free dividing case, where cells divide depending on their length Δq_i. If a uniformly distributed random number less than $p(\Delta q_i)$ is drawn, cell i divides as described in eq (2.12).

For the free dividing case, upon release of the boundary constraint at one of the boundary cells, the lattice invades the free space and the boundary rapidly reaches a velocity fluctuating around a constant value as can be seen by blue dots in fig. 2.19 B). The probability of division is shown in fig. 2.20 A). The lattice melts into the free space at an on average constant speed and a narrow band of high probability of

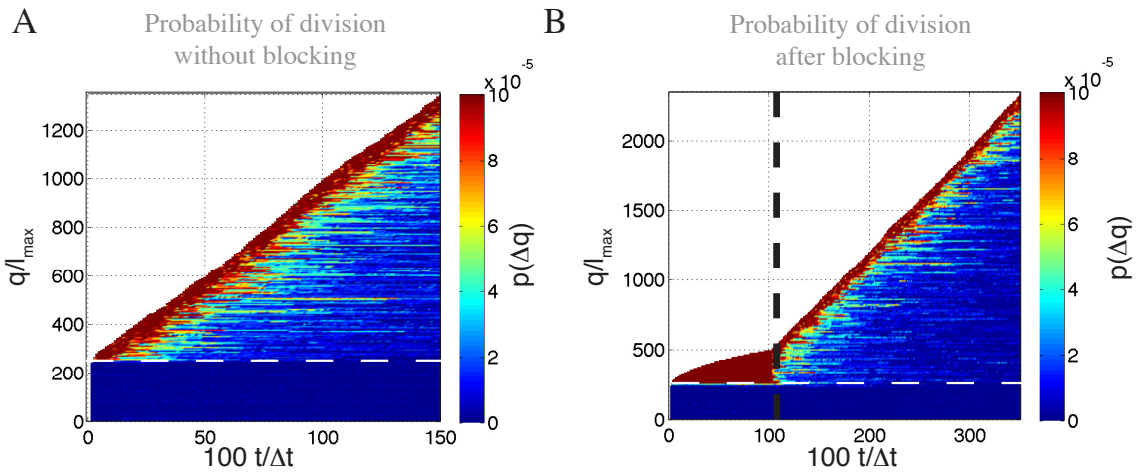

Figure 2.20: Division probability in growing lattices upon boundary constraint release. A) Colour codes for probability of division, blue indicating low and red high. y-axis shows position measured in units of l_{max} and x-axis shows time measured in simulation steps. White indicates free space. Boundary condition becomes released and the lattice melts into the free space. A band of high probability of division builds up. White dashed line indicates boundary position. B). Probability of division as A), but with block of division until a critical time indicated by black dashed line is reached. The lattice melts at the free boundary and more and more cells in the tissue have increased length. After release of division block, rapid cell division is observed and a narrow band of high probability of division builds up.

division builds up with the same scaling law as determined by eq. (2.18). The white dashed line indicates the position of the boundary upon release and shows, that the majority of the bulk remains at a state of low likelihood of division.

In the division blocked case, one observes that the boundary slows down, and almost reaches a halt for $t < t_{block}$. For $t \geq t_{block}$, where division is not anymore blocked, the boundary rapidly accelerates and reaches a similar velocity as observed in case of an unaltered mitotic rate. The probability of division is shown in fig. 2.20 B). For $t < t_{block}$, the lattice melts into the open space, with increasing length of cells and probability of division. Once division division block becomes released for $t \geq t_{block}$, many cells rapidly divide and a narrow band of high probability of division

becomes installed.

We have seen that our model is able to reproduce the long term dynamics of boundary advancement in the scratch wound assay. Upon release of boundary constraints, a zone of high likelihood of division becomes established, as observed in the experiment. Mechanical relaxation of the lattice leads to division and subsequently boundary advancement. Blocking division results in continued mechanical relaxation, leading to a increased zone with high likelihood of division. Upon block release, cells divide, leading to a narrow zone of high likelihood of division and constant boundary velocity, as in the free division case.

2.5 Summary

We have studied the dynamics of growing colonies of adherent cells and identified two growth regimes. In the exponential regime, cells divide rapidly and the colony grows according to an exponential. As the colony increases in size, a transition away from the exponential regime is observed. This is accompanied by a gradual migration arrest and cell density increase. A morphological transition time-point characterised by increased order in the tissue marks a sharp transition from a state characterised by continuously decreasing velocity to a state characterised by steady topology except divisions. After this transition, cells continue to divide as indicated by a constantly shifting area distribution towards smaller cell sizes. Eventually, this cell size distribution converges against a steady distribution accompanied by proliferation arrest.

Furthermore, we have proposed and studied a model for migrating cell collectives. Based on the lattice model for epithelial cell collectives, we introduced attachment points representing the points of contact that cells form with the extracellular matrix. These attachment points are coupled elastically to the cell and obey a Langevin equation describing their motion in a harmonic potential around the centre of mass of the corresponding cell driven by a random force.

Under the assumption that the division rate depends on cell size, the model of a growing colony of adherent cells showed that mechanical constraints induced by

finite advancement of boundary cells results in observed cell size reduction in the bulk. A scaling law for the onset of reduction of cell sizes was identified and revealed an inverse proportionality to the unconstrained proliferation rate of cells as well as a logarithmic scaling with the maximum crawling velocity of cells and attachment point relaxation time scale. Addition of plastic cell size increase, in response to tension produces cell size distributions resembling the form of our measured distributions and results in a state of minimal compression in the bulk and tension at the boundary of the colony.

According to this model, a zone of low density and high proliferation at the boundary of the colony emerges. By growing a lattice in a confined region and subsequent release of boundary constraints on one side, the model predicts that a zone of low density with high proliferation rate re-merges from the boundary. Blocking of cell division showed, that cell proliferation is a major contributor to boundary advancement.

We investigated the scratch wound essay, considering the long term behaviour of the tissue focusing on the boundary advancement as well as the mechanical role in the control of cell proliferation. A line of MDCK cells expressing the FUCCI marker separating the cell cycle into two parts was used to study the cues of cell cycle advancement.

Single cell velocity analysis revealed that the boundary linearly accelerates and subsequently fluctuates around a constant velocity. Blocking of cell cycle progression at the $G1/S$ interface showed that initial boundary advancement is due to directed motion of the cells into the open space until the boundary significantly slows down. Releasing the cell cycle block showed that the boundary advancement rapidly reaches the same behaviour of fluctuating velocities around a constant velocity as in the wild type case. This suggest, that the long term dynamics is due to cell division. In both cases, in the long term dynamics, a plateau of cells with similar high velocity reaching deep into the tissue emerges.

Cells where identified to reduce density from the edge towards the inside, interpreted as a melting of the tissue. A plateau of low density, similar to the plateau of high velocity behind the leading edge was found to build-up. As this part coin-

cides with the part where the tissue proliferates most, the size distribution of cells in $G0/G1$ and $S/G2/M$-phase respectively was analysed, revealing a greater area covered by cells in $S/G2/M$-phase. A closer inspection of the size distribution of cells as they advance in cell cycle revealed that on average cells increase their area linearly while travelling through the cell cycle, with a critical area marking the entrance to S-phase. This gives rise to the hypothesis of a size checkpoint in $G1$-phase.

Analysis of the $S/G2/M$-phase of cells revealed two clusters of cells separated by different duration until M-phase completion. Inspection of the area distributions of the cells belonging to the two clusters revealed that cells requiring more time in $S/G2/M$ are smaller than cells passing fast through $S/G2/M$. This suggests, that another area checkpoint may exist, where cells check the area available and only pass through this check point at a high likelihood when minimal amount of space is available.

To directly test this hypothesis, we propose a direct mechanical manipulation of tissues. Cells placed on a relaxed extendible PDMS membrane, should be to a grown dense, such that the entire tissue is in a state of contact inhibition of proliferation. Then the membrane becomes stretched, which should lead to a number of cells entering S-phase, if the hypothesis of the first checkpoint holds. Measurement of the duration of $S/G2/M$-phase compared to tissues where the PDMS membrane becomes relaxed again after cells enter S-phase - subsequently leading to less space available to individual cells - should then result in cells taking a longer time in the compressed case, if the second threshold in M-phase holds.

Chapter 3

Biophysical aspects of guided tissue dynamics

The spatio-temporal control of growth and remodelling of tissues is known to underlie organogenesis. During embryogenesis, many things must be tightly controlled, legs or arms formed at the same times as the nervous system patterned. Example scenarios where the final location of the organ that is about to be formed does not yet exist or is not finished are easy to imagine. A sequential formation, where the formation of the organ has to await the completion of its final location seems an inefficient strategy, consuming time and introducing additional constraints. A solution that nature came up with to this problem is given by simultaneously growing the destination, whilst forming the organ at some other position and transporting it to the final locus.

A common strategy is provided by directional migration of tissues, that prepattern the organ, so called primordia, and move the organ to its final destination. An example is provided by the formation of the lateral line, a sequence of mechanosensory organs formed by a tissue, that sequentially deposits the organs en route. Directional migration of tissues involves at least a partial epithelial to mesenchymal transition at the leading part of the tissue. Cells at the forefront flatten, resulting in a wedged shape of the moving tissue. Such a strategy is employed by cancerous epithelia, as they move about in the organism to give rise to metastases. Even the signalling

pathways that guide the motion employed in the embryonic formation process are used by these cancers.

The seemingly simple question, how can cells perform directional migration in a tissue, turns out to be more complex than at first sight. The distance travelled by these tissues ranges up to the hundred fold of their size. Establishment of prepatterned signalling gradients on the scale of millimetres by cells on the scale of μm poses challenges to the organism. Are there alternative ways to induce the motion of the tissue? Looking at the level of the tissue, can cells in the tissues bulk become polarised or are they passively dragged along? Motile tissues are known to span considerable lengths and thus scenarios with cells experiencing different signalling molecule concentration gradients depending on their position within the tissue may be imagined. They also grow, to preform the organ forerunners. What is the cue that regulates the integrity of such tissues and how do they feedback into the motility? Here we approach the mechanical regulation of the interplay of growth and directional tissue dynamics.

3.1 Introduction: The lateral line primordium in Zebrafish

Formation of the lateral line in fish is divided in two parts, an anterior lateral line in the head and a posterior lateral line (pll) running down the tail along both flanks of the fish. The pll is formed by a group of about 100 cells, together called the posterior lateral line primordium (pLLP).

A Zebrafish embryo 32 hours post fertilisation (hpf) expressing a green membrane marker is shown in fig. 3.1 A). A zoom on the pLLP in fig. 3.1 B), shows the assembly of the tissue into discrete rosettes each comprising approximately 25 cells, so called pro-neuromasts, which are the forerunners of the later orang. A schematic of the clustering in form of contour lines projected on top of a schematic section through the tissue is shown in fig. 3.1 B). The tissue is about 150 μm long, 30 μm wide, 15 μm thick and moves at a speed of approximately 1 $\mu m/min$ through the fish,

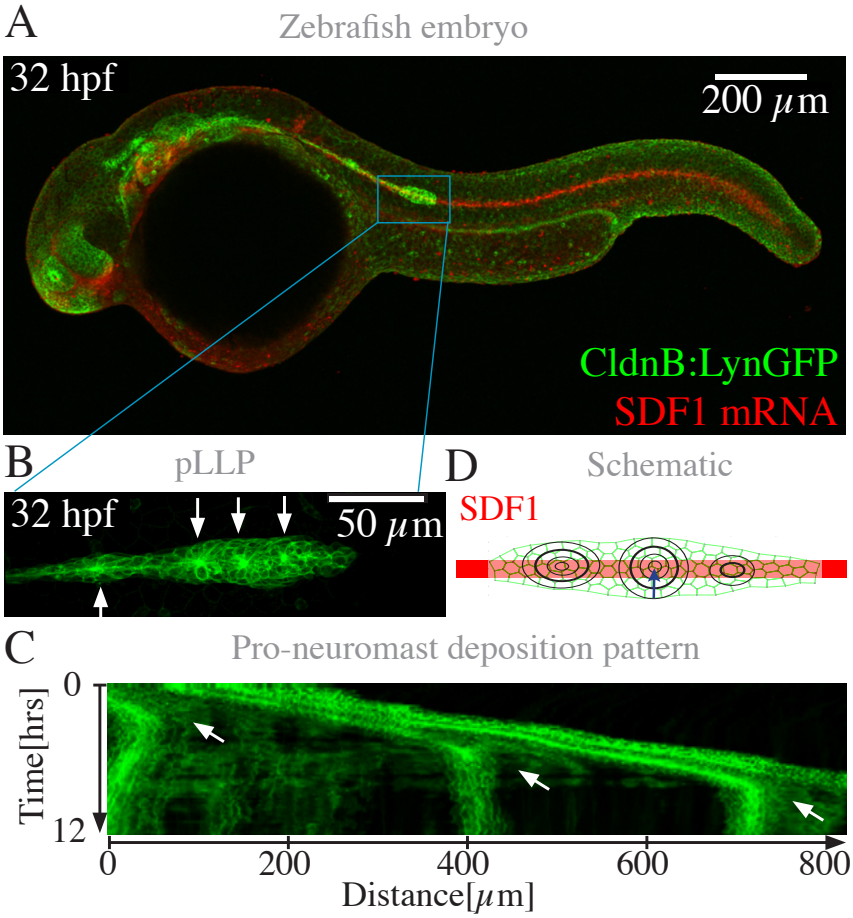

Figure 3.1: The posterior lateral line primordium of Zebrafish. A) Zebrafish embryo 32 hours post fertilisation (hpf). Scalebar indicates 200 μm. Membrane marker ClaudinB-Lyn-GFP [Haas06] shown in green and chemokine SDF1 mRNA shown in red. B) Zoom on pLLP with membrane marker ClaudinB-Lyn-GFP. A neuromast is about to be deposited at the rear (left most arrow) and two pro-neuromasts are already patterned (middle two arrows) in the tissue. Right most arrow indicates the formation zone of new neuromasts. C) Kymograph showing temporal evolution of fluorescent signal. Time is running from 0 *hours* at the top to 12 *hours* at the bottom. Along the 800 μm, 3 neuromast depositions, indicated by arrows are observed. Deposited cell clusters cease migration. D) Schematic of a cross-section through the tissue with contour lines superimposed, indicating the height increase in pro-neuromasts, which form discrete subunits of the tissue.

starting its journey at the ear 22 hpf. The migration process is finished after 48 hpf, when the tissue has reached the tails end, with on average 6 deposited organs regularly spaced along each flank.

As the pLLP moves through the fish, pro-neuromasts are repeatedly deposited en route. Deposition happens at the rear of the tissue, where the most mature organ forerunners slow down and leave the tissue, as shown in a kymograph, that maps the temporal evolution of fluorescence signal along a line, plotted in fig. 3.1 C). The rest of the tissue continues migration. Pro-neuromasts assembly happens de-novo at an interface between the tip and the front most pro-neuromast with respect to the direction of motion [Gompel01].

It was shown to strongly depend on the fibroblast growth factor family (FGF) [Nechiporuk08] [LecaudeyCakan08] [Cakan09]. Genetic or pharmaceutical inhibition of FGF signalling results in disassembly of pro-neuromasts accompanied by a migration defect, which both become reinstalled upon reactivation of signalling.

Migration of the tissue strongly depends on the presence of the chemokine receptors CXCR4/7 and the corresponding ligand SDF1 [David02, Haas06, Valentin07, Valentin09]. The tissue follows a line of chemokine SDF1, expressed by cells that the tissue migrates on, shown in red in fig. 3.1 A). Primordia in mutant fish, lacking the chemokine or the receptor, show a characteristic loss of tissue motility. Thus chemokine signalling promotes the migration of the tissue.

The standard chemotaxis mechanism, proposing a prepatterned graded ligand field from the head down to the tail, was challenged by an interesting genetic experiment where the ligand expression was altered, resulting in a guidance stripe, that is significantly shorter than normal. Once the pLLP reached the end of the ligand expressing line in these mutants, it performed a U-turn and continued migration in the opposing direction, like a motorist driving against traffic. This and other findings render a prepatterned graded ligand distribution as source of tissues directionality unlikely.

While much about the signalling pathways involved in tissue guidance is known, the clear mechanism how the tissue obtains its polarity remains to be shown. In the chemokine signalling mutants the preferred direction appears lost, which may be

explained by a loss of the coordinated polarisation or loss of mobility of individuals. Migration is a necessary requirement for pro-neuromast deposition. Cell division seems to play an important role in the deposition process, as reduced proliferation results in reduced number of deposited neuromasts. How is the migration of the collective coupled to proliferation and the major task of organ formation in form of pro-neuromast deposition? What are the mechanical consequences arising from proliferation in a directionally migrating collective and how do they feedback to organ deposition?

3.2 Chemokine signalling guided tissue dynamics

Motion is key to the organ formation process, thus a detailed study of the mechanism of migration required. SDF1 dependant CXCR4 signalling was identified as the guidance cue of the tissue, as knockout of one of the two molecules results in a migration defect. We therefore decided to consider the quantitative differences between the normal primordia and CXCR4 mutants, which are deficient in SDF1 signalling. An example maximum intensity projection of an optically sectioned wild type pLLP with membrane and nuclear markers is shown in fig. 3.2 A), a migration deficient pLLP is shown in fig. 3.2 B). Scale bars indicate 20 μm. The WT primordia have an elliptic shape with major axis in the direction of migration and two pro-neuromasts are observed in the last two thirds of the tissue. The mutants are shorter in the direction of migration and broader compared to wild type. Two larger constrictions are present in the maximum intensity projection of fig. 3.2 B).

The apparent difference in the form of the tissues can be induced by repositioning cells in the tissue, or by stretching the tissue induced by motion. To analyse this in more detail, we performed quantitative analysis of the migration process by automated segmentation and tracking of cell nuclei over time. An example segmentation with detected individual nuclei on top of a maximum intensity projection of the original image is shown in fig. 3.2 C). Temporal evolution of segmented nuclei colour coded for time are shown in fig. 3.2 D) and E) for wild type and mutant background respectively. The detected WT objects collectively move in direction of

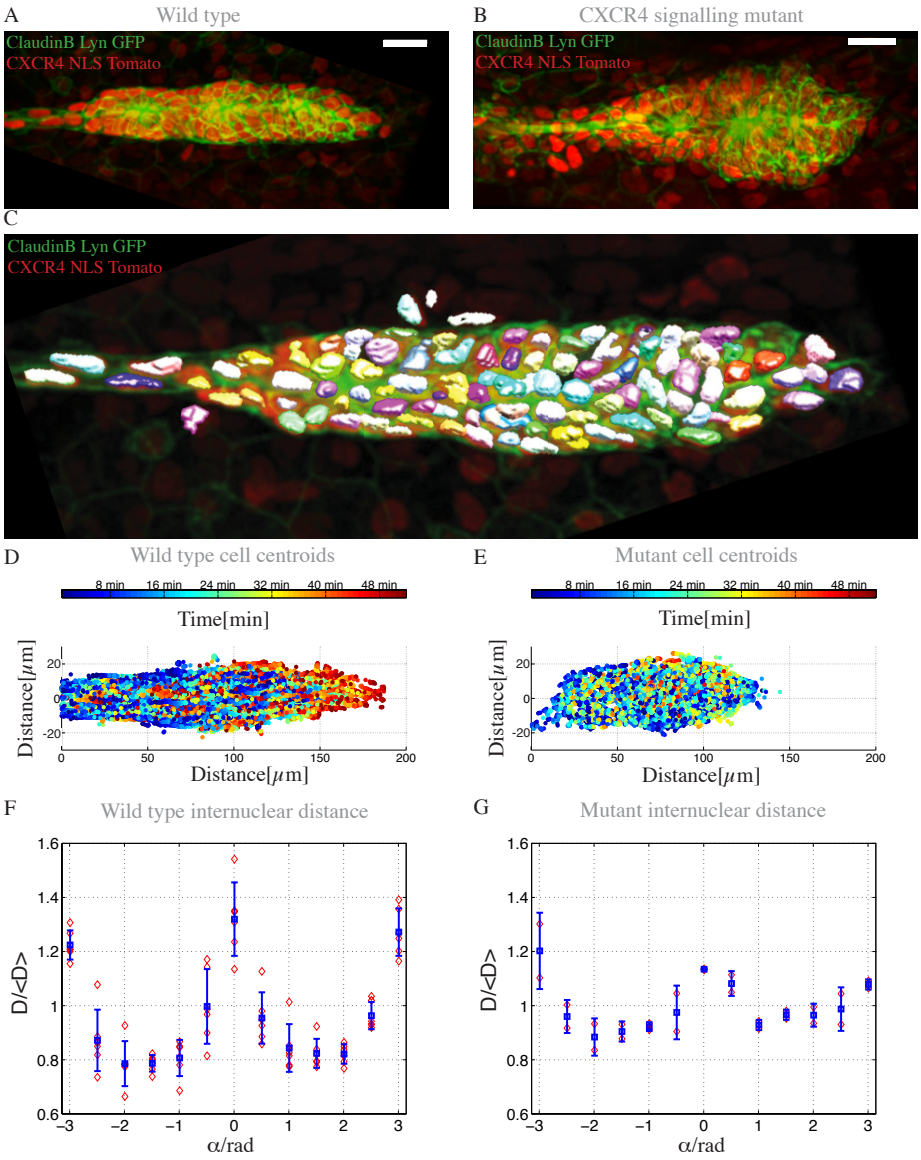

Figure 3.2: Response of epithelia to directional motion. A) WT lateral line primordium with ClaudinB Lyn GFP membrane and CXCR4 NLS Tomato nuclear marker. Scale bar indicates 20 μm. B) CXCR4 mutant as A). C) Segmented Nuclei projected on A). Detected individual non-connected nuclei are assigned random colours. D) WT lateral view of centroids of segmented nuclei. Colour codes for time. E) CXCR4 mutant as D). F) Topology for six WT samples shown as red diamonds. Mean and standard deviation denoted by blue box and error bar. 0 indicates direction of migration. G) as F) for two CXCR4 mutant samples.

migration, tracks of individuals may be identified. Considering the centroids in the mutant background, no clear preferred direction is identified, identification of tracks by visual inspection is more difficult due to crowding and lack of directionality.

The ratio of the distance between neighbouring nuclei D against the average distance of neighbouring nuclei $\langle D \rangle$ throughout the tissue as a function of the angle, which the connecting line between nuclei forms with the direction of migration provides a measure for deformation of the tissue and is shown in fig. 3.2 F) and G) for wild type and mutant respectively. In both cases, maxima are observed for angles around $0, \pm\pi$ and minima are observed around $\pm\frac{\pi}{2}$. Thus the distance of nuclei along the long axis of the tissue is increased compared to the distance of nuclei along the short axis. At the maxima, the wild type internuclear distance is increased by 32 per cent, whereas the mutant internuclear distance is increased only by 13 per cent. Note that also the distance along the minor axis between neighbours is less in case of wild type tissues as compared to mutants. Thus motion induces an increase of internuclear distance along the major axis.

Nearest neighbour tracks for wild type and mutant primordia are shown in fig. 3.3 A) and B) respectively, with colour coding for the position of the individual nuclei along the minor axis. Over the duration of the experiment, the tracks do not mix, indicating that little neighbour exchange takes place. The WT tracks are straight lines, whereas the mutant tracks fluctuate around a preferred position. Based on the tracks, velocities $\mathbf{v}_i(t)$ for individual nuclei i at time point t are reconstructed. A measure for order of the migration in the collective is given by the sum of the complex unit vectors with polar angle $\alpha_i(t) = atan(\frac{v_{iy}(t)}{v_{ix}(t)})$. $O(t) = \|\frac{1}{N}\sum_i^N e^{i\alpha_i(t)}\|$ provides an order parameter, which is a number between 0 and 1, where 0 denotes complete disorder and 1 resulting from all vectors pointing in the same direction, i.e. complete order [Kuramoto84]. The temporal evolution of the order parameter for wild type and mutant primordia is shown in fig. 3.3 C). Wild type migration has a high order fluctuating around .8 over the experiments duration, whereas order in mutants is significantly reduced, fluctuating around 0.2. This suggests that the

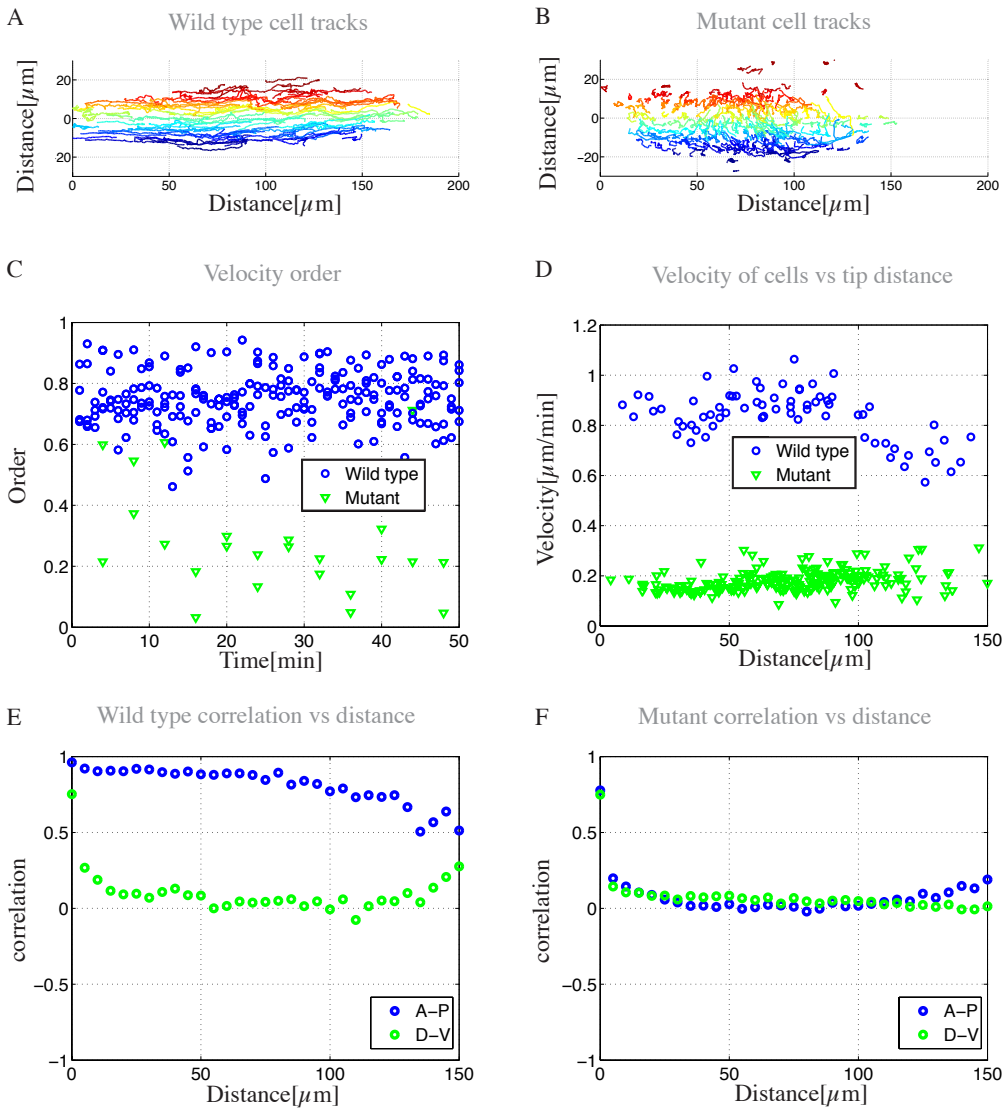

Figure 3.3: Highly ordered motion characterises the directional migration of epithelia. A) Wild type tracks. Individual nuclei colour coded for position. Red dorsal most, blue ventral most. B) CXCR4 mutant tracks. Colour codes as A). C) Order versus time. Blue circles are wild type from six different samples. Green triangles are from two CXCR4 mutant samples. D) Velocity as a function of distance to the front. Blue circles are WT, green triangles CXCR4 mutant. E) Cross-correlation of tracks as a function of pairwise distance. Distances are binned in groups of 5 μm and average cross-correlation is calculated for each bin. Blue dots denote the cross-correlation along the anterior-posterior axis, i.e. direction of migration. Green dots denote cross-correlation along minor axis. F) as E) for migration mutants.

individual nuclei are highly coordinated in case of WT and loose the coordination in the mutant background.

The magnitude of the average velocity $\langle \mathbf{v}_i \rangle = \frac{1}{N_T} \sum_{t=1}^{N_T} \mathbf{v}_i(t)$ is plotted against the distance of the nucleus from the tip in fig. 3.3 D). WT nuclei show a velocity around 0.9 $\frac{\mu m}{min}$, decreasing after approximately 100 μm, which marks a transition zone in the tissue, where a pro neuromast becomes deposited. The mutants show a significantly decreased velocity around 0.2 $\frac{\mu m}{min}$ with no obvious difference along the tissue.

Cross-correlation of tracks along the major and minor axis of the tissue provides a measure for similarity of the motion of two nuclei in the respective directions. A plot of the cross-correlation against the distance between nuclei is shown in fig. 3.3 E) for wild type and F) for signalling mutant primordia. Wild type primordia show a strong correlation in the direction of migration, that slowly drops over the distances ranging from 0 to 150 μm. Along the tissues minor axis, the correlation drops quickly and is close to zero after 15 μm. Mutant primordia show a similar drop as WT tissues in the short axis with increasing distance along both long and short axis.

Thus, wild type tissues, with active chemokine signalling are highly ordered and move in a well coordinated fashion. Signalling mutants are still able to move, as their velocity doesn't vanish, but their polarisation appears lost, which is indicated by significantly reduced order of the velocities. This is reflected in the topology of the tissue, which is stretched in the wild type case. Based on these observations, we will develop a novel chemokine signalling model, in the next section.

3.3 Travelling waves with constant attractant expression

Parts of this and the following section are accepted for publication in Physical Biology [Streichan11].

The previous section has shown that chemokine signalling is able to promote order in a migrating tissue. Here we want to pursue the question how this order may be achieved. There is a series of models on chemotaxis that was initiated by the famous Keller-Segel model, which approach polarisation of cells via chemokines [Keller71, Horstmann04, Painter09]. Such models rely on a graded expression of the chemoattractant from the source to the cell collective, which is in contrast to previous studies in the pLLP of Zebrafish that support the hypothesis that directional migration in the absence of a graded guidance molecule distribution may be a commonly used mechanism. We propose a dynamically maintained mechanism for the migration of a cell collective in a setting with constant ligand expression, where the cells encode an initial symmetry breaking in their velocity to shape the ligand and maintain the preferred direction of motion.

Cells migrating in an epithelium may be described using a 2 dimensional approximation: A cell is understood as a polygon in a lattice and the tissue consists of the collection of cells. The position of individual cells α is described by the centre of mass c_α:

$$\begin{aligned} c_\alpha : \mathbf{R} &\to \mathbf{R}^2 \\ (t) &\mapsto c_\alpha(x,y). \end{aligned}$$

Lets define $H_\alpha(x,y) := \begin{cases} 1 & \text{if } (x,y) \in \alpha \\ 0 & \text{else} \end{cases}$ as the domain of cell α. Furthermore, we

assume for simplicity that cells express receptor

$$\begin{aligned} r_\alpha : \mathbf{R}^2 \times \mathbf{R} &\to \mathbf{R}^+ \\ (x, y, t) &\mapsto r_\alpha(x, y, t) = H_\alpha(x, y) r_\alpha(t) \end{aligned}$$

only on the basal membrane at a rate ν and degrade it at a rate σ_r. Let s denote the ligand. It is a function of space and time

$$\begin{aligned} s : \mathbf{R}^2 \times \mathbf{R} &\to \mathbf{R}^+ \\ (x, y, t) &\mapsto s(x, y, t), \end{aligned}$$

has a diffusion coefficient D, is expressed at a rate γ along a stripe of fixed width 2ϵ and degrades at a rate σ. In the vicinity of cell α, the receptor and the ligand are co-internalised at a rate ρ. Written as a simple system of coupled differential equations, we have

$$\begin{aligned} \partial_t s &= D\Delta s - \sum_\alpha \big(\sigma + \rho r_\alpha\big) s + \gamma \delta(|y| < \epsilon) \\ \partial_t r_\alpha &= \nu - \big(\sigma_r + \rho s\big) r_\alpha, \end{aligned} \tag{3.1}$$

where

$$\delta(|y| < \epsilon) := \begin{cases} 1 & \text{if } |y| < \epsilon \\ 0 & \text{else} \end{cases} .$$

We assume that cells move to greater concentrations of ligand, such that the position of the cells c_α is updated along the average gradient in ligand

$$\dot{c}_\alpha = \zeta \langle \nabla s \rangle_\alpha. \tag{3.2}$$

where

$$\langle \nabla s \rangle_\alpha(t) \quad = \frac{\int \nabla s(x,y,t) H_\alpha(x,y) dx dy}{\int H_\alpha(x,y) dx dy}$$

denotes averaging of the gradient in ligand along cell α and ζ the strength of the translation of the gradient.

Taking the limit of a small expression pattern ϵ relative to the extension of the cell collective, we may reduce the problem to 1 dimension and consider it a motion along a line of constantly expressed ligand. All the above entities that are functions on $\mathbf{R}^2$ are now functions on $\mathbf{R}$. The cell collective may be considered as a rod of finite length $2L$ with constant receptor concentration along the rod. Then the system reads as

$$\partial_t s = D\partial_{xx} s - \mu(x-c)s + \gamma \tag{3.3}$$

$$\dot{c} = \zeta\langle\partial_x s\rangle = \zeta\frac{\int_{-L}^{L}\partial_x s dx}{2L}, \tag{3.4}$$

where c denotes the centre of mass of the rod and $\mu(x-c) = \sigma+\rho H(-(x-c)+L)H(x-c+L)$ describes the degradation of the substrate and additional consumption by the receptor. $H(x)$ is the heaviside function where $H(x) = 1$ if $x \geq 0$ and $H(x) = 0$ if $x < 0$.

There are three length scales in the system, (i) the length of the rod L, (ii) the diffusion based spread of the ligand on the time scale of ligand degradation $\lambda_D := \sqrt{\frac{D}{\sigma}}$ and (iii) the distance the rod travels on the time scale of the ligand degradation $\lambda_v := \frac{v}{\sigma}$. The timescales may also be related to get a comparison of the synthesis $\tilde{\gamma} := \frac{\gamma}{\sigma}$ and consumption rate $\tilde{\rho} := \frac{\rho}{\sigma}$ with the degradation rate of the ligand. A combination of timescales and length scales yields the scale for the velocity of the rod, which we defined as $v_\sigma = \lambda_D\sigma$.

Written with the natural length scales in the reference frame of the rod, which is defined as $\xi := x - c.$, eqs. 3.3 and 3.4 may be transposed into an in-homogeneous ordinary differential equation

$$-\lambda_v u'(\xi) = \lambda_D^2 u''(\xi) - \big(1 + \tilde{\rho}H(-\xi+L)H(\xi+L)\big)u(\xi) + \tilde{\gamma}. \tag{3.5}$$

Note that for a solution to exist, eq. (3.4) must be self-consistently checked. The

moving frame is partitioned in 3 regimes: Behind the Rod 1 := $\{\xi \mid \xi < -L\}$, in the vicinity of the rod 2 := $\{\xi \mid L \geq \xi \geq -L\}$ and before the rod 3 := $\{\xi \mid \xi > L\}$. For $\dot{c} = v = const$, the general solution of the system described by eq. (3.5) in each regime $\{1, 2, 3\}$ is then given by

$$u^{(i)}(\xi) = \frac{\lambda_D^2}{1+\tilde{\rho}}\Big(\frac{\tilde{\gamma}}{\lambda_D} - A^{(i)}\lambda_+^{(i)}e^{\lambda_-^{(i)}\xi} - B^{(i)}\lambda_-^{(i)}e^{\lambda_+^{(i)}\xi}\Big), \tag{3.6}$$

with $\lambda_\mp^{(i)} = -\frac{\lambda_v}{2\lambda_D^2} \mp \sqrt{\frac{1+\tilde{\rho}}{\lambda_D^2} + \frac{\lambda_v^2}{4\lambda_D^4}})$ as the eigenvalues of the corresponding linear system, where $i = 1, 2, 3$ denotes the respective regimes in the moving frame. Note that behind and before the rod, $\tilde{\rho} = 0$, whereas at the position of the rod $\tilde{\rho} \neq 0$ and thus the eigenvalues take different values in the individual regimes.

The eigenvalues describe, how the velocity alters the intrinsic length scale. For vanishing velocities behind and before the rod, the absolute value of the reciprocal of the eigenvalues coincides with the ligand spread and in the vicinity it coincides with the ligand spread altered by co-internalisation. For $v > 0$ we have $\lambda_v > 0$ and thus the absolute value of the inverse of $\lambda_-^{(i)}$ is less than λ_D and for $v < 0$ it exceeds the scale of the ligand spread. In the case of the second eigenvalue $\lambda_+^{(i)}$ the pattern is swapped between $v < 0$ and $v > 0$.

Considering that in the limits $\xi \to \pm\infty$ the solution should be finite and reach the steady sate $\tilde{\gamma}$, we demand in regime 1 the constant $A^{(1)} = 0$, similarly in regime 3 $B^{(3)} = 0$. Demanding continuity of the solution on the boundaries of the rod gives $B^{(1)}$ and $A^{(3)}$. If we also demand the derivative of the solution to be continuous, we fix $B^{(2)}$ and $A^{(2)}$. The resulting $A^{(i)}$ and $B^{(i)}$ for continuity of the solution and of the derivative are shown in the appendix. From now on we make the identification $A = A^{(2)}$ and $B = B^{(2)}$.

The averaged ligand gradient along the position of the rod must equal the velocity of the rod for a self-consistent solution to exist.

$$g(v) = \zeta\Big(\frac{A(v)}{\lambda_-^{(2)}(v)L}\sinh(\lambda_-^{(2)}(v)L) + \frac{B(v)}{\lambda_+^{(2)}(v)L}\sinh(\lambda_+^{(2)}(v)L)\Big) \overset{!}{=} v. \tag{3.7}$$

From this it immediately follows that if $v = 0$ then the constants must obey

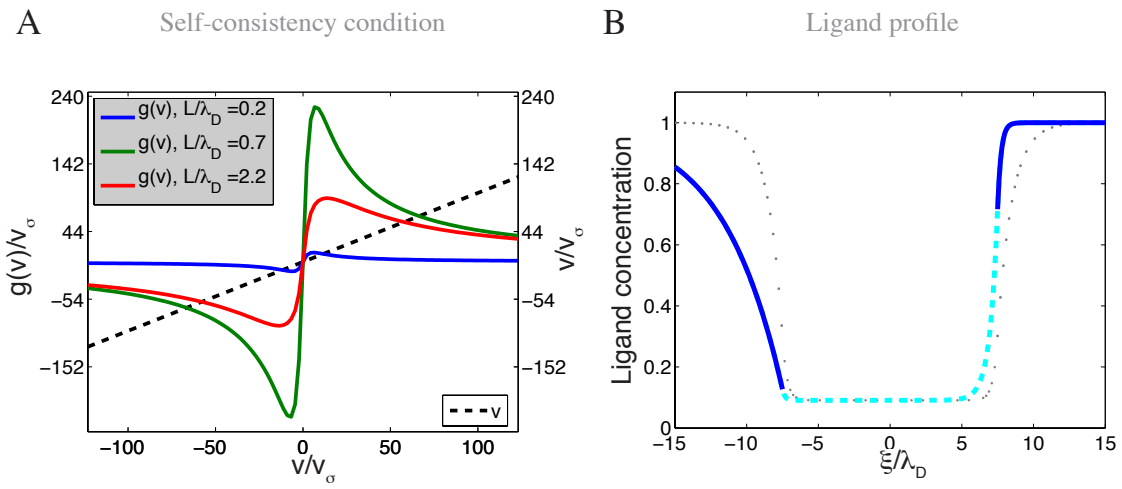

Figure 3.4: Self consistent solutions for dynamically maintained gradients. A) Self-consistent solutions of eq. (3.7) exist: Dashed line denotes v and coloured lines are the lhs of eq. (3.7) for various L. The intersections with the dashed line are the self-consistent v. The profile shows that 0 is always a solution and positive as well as negative solutions exist. B) Typical ligand concentration in vicinity of rod with $v > 0$ solution shown as dashed cyan line and in free space as solid blue. Green line between domain 1 and 2 denotes the rods rear and the line between 2 and 3 the front. A strong gradient at the front of the rod is observed, whereas in the centre of the rod the new steady state ligand concentration is reached. Dotted grey profile indicates the symmetric $v = 0$ solution.

$B = -A$, and on the other hand if $B = -A$ a self-consistent solution is given by $v = 0$. For $B > -A > 0$ the function $g(v)$ is a monotonously decreasing function of v and also $g(v) > 0$ for $v < 0$. Thus self-consistent solutions exist and obey $v > 0$ in this regime. The case $-A > B > 0$ gives roots $v < 0$. Fig. 3.4 A shows the rhs of eq. (3.7) as a black dashed line and the lhs of eq. (3.7) for various L. One observes multiple self-consistent solutions: $v = 0$ which is always included, since $A\,|_{v=0} = -B\,|_{v=0}$, a positive and a negative v.

Figure 3.4 B shows a typical profile of a $v > 0$ solution and a $v = 0$ solution. Green bars indicate the front and the back of the rod respectively . The symmetric $v = 0$ solution is shown as grey dots. At the centre of the rod, the ligand concentration

drops to the altered steady state - determined by ligand synthesis, degradation and uptake - and reaches the steady state concentration - given by degradation and synthesis - outside the rod. For the $v > 0$ solution, the ligand concentration along the position of the cell collective is marked as a cyan dashed line and in the adjacent unoccupied space plotted as a solid blue line . One observes a non-symmetric profile in ligand concentration and a slope increasing in the direction of migration at the front of the rod. The ligand drops to the altered steady state concentration at the centre of the rod and reaches the steady state concentration behind the rod. Similar to the change of the wavelength in a Doppler effect the spread of the ligand at the front and at the back of the rod are changed. Before the rod, $\lambda_-^{(3)}$ gives the dominant term in eq. (3.6), which explains the steep slope in regime 3, as this leads to an effectively decreased ligand spread due to the motion of the rod. In the limit of $\lambda_v \to 0$, $|\lambda_-^{(3)}|$ approaches λ_D^{-1} and the blue curve in regime 3 approaches the grey dotted curve. A similar argument holds for the shallow slope at the back.

3.3.1 Velocity approximation and numerical analysis

Written in implicit form, eq. (3.7) reads $g(v) - v = 0$. A linearisation of this eq. for velocities with $v \approx v_\epsilon$ by Taylor expansion around v_ϵ and subsequent solution for v of the eq. $g(v_\epsilon) - v_\epsilon + \big(g'(v_\epsilon) - 1\big)(v - v_\epsilon) = 0$ gives the first order approximation of the rod's velocity.

To validate the approximations, the root of eq. (3.7) was studied numerically by use of the trust-region dogleg method implemented in Matlab [More80].

The velocity as a function of the rod's extension is shown in fig. 3.5 A. The linear approximation from the implicit version of eq. (3.7) is plotted in blue, the numerical solution of eq. (3.7) as yellow asterisks. The velocity approximation $v_\epsilon = 25.3 v_\sigma$ is valid, as the two curves coincide well. In both cases, one observes an initial increase in velocity with increasing length until a critical length L_{max} is reached. Then the velocity drops with increasing length. This is due to the averaging procedure during the determination of the velocity, since for $L > \lambda_D$, the gradient flattens out in the centre.

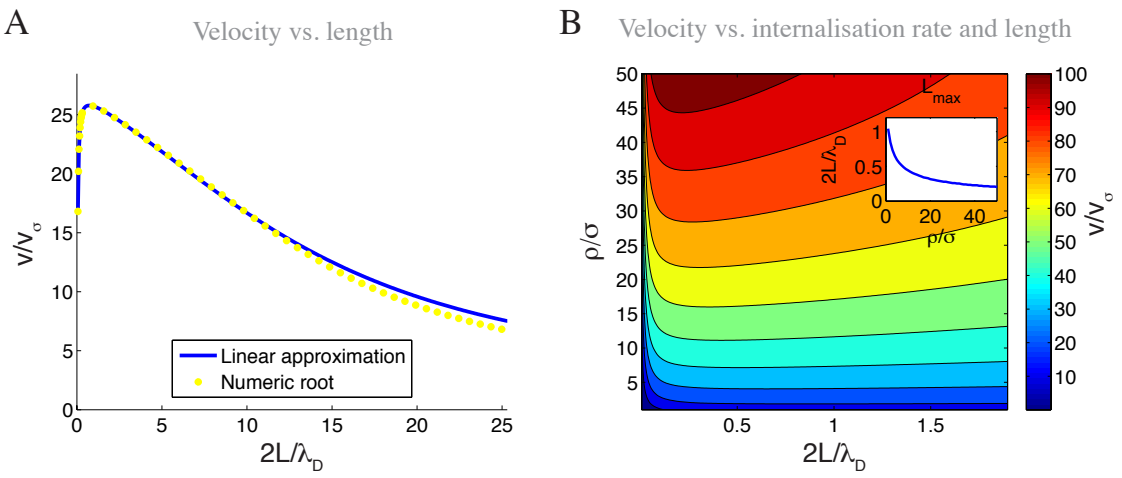

Figure 3.5: Velocity is length dependant. A) Velocity over length. Linear approximation from eq. (3.7) with $v_\epsilon = 25.3 v_\sigma$ in blue solid line and numerical root of eq. (3.7) shown as yellow asterisk. B) Contours of velocity as a function of ρ versus length $2L$. Inset shows the optimal length L_{max} that maximises the velocity as a function of ρ.

Figure 3.5 B shows velocity contours as a function of additional consumption of ligand ρ over the extension of the cell collective. One observes that the velocity of the tissue increases with increasing ρ, as the gradient at the front becomes steeper with increasing ρ. The inset shows that the optimal length L_{max} at which the maximum velocity occurs is shifted to smaller extensions with increasing ρ, since a steeper gradient results in a smaller fraction of the rod that contributes to the averaging process.

From eq. (3.7) it follows that the velocity also depends on the length of the rod. Therefore, the profile of the ligand also depends on the rods extension as shown in fig. 3.6 A. Here, the gradient of the ligand profile at the position of the rod is plotted over the size of the rod. The location along the rod is shown on the x-axis, where 1 denotes the front and -1 the rear of the rod. The y axis shows increasing rod length. It is observed, that with increasing length, the ligand gradient increases at the front, whereas it becomes shallower at the rear. In the next section, we will analyse a tissue

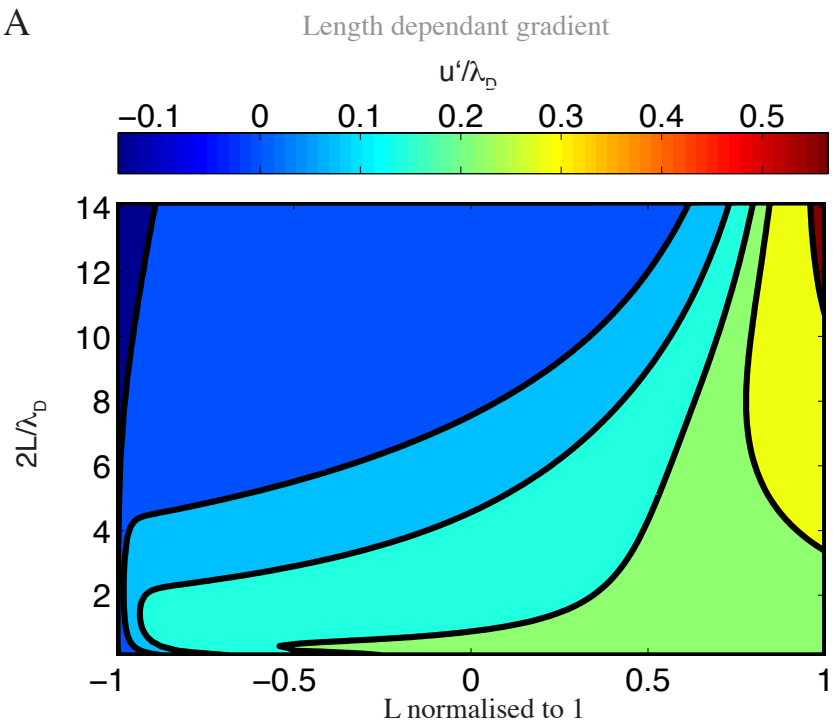

Figure 3.6: Ligand distribution results in local differences of directionality inducing gradient. A) Gradient of ligand as a function of rod length: x-axis shows the normalised extension of the rod, where 1 denotes the rod's front and -1 the rod's rear. y-axis shows various lengths of the rod. With increasing L, the gradient in direction of motion increases. At a threshold a gradient in the opposite of the direction of motion builds up at the rod's rear.

growth model, which utilises the length dependent migration to deposit cells as the tissue migrates.

3.3.2 Coupling tissue growth to migration and organ deposition

As described earlier, migrating tissues can deposit cell groups as they move along their path. The loss of cells due to deposition is in parts compensated by cell division in case of the pLLP. Our dynamically maintained gradients model predicts that the

gradient profile is a function of length. With increasing length a zone of shallow gradient profile emerges at the back. To test, whether the identified length-dependent gradient can be used for the deposition of cells, we consider a coupling of this model to our previously developed model for motility of mechanically coupled adherent cells in a growing lattice. The rationale is, that a growing lattice will increase its length and thereby the ligand profile experienced by cells will change. As the lattice size increases, cells in the rear will experience a shallow ligand profile and become less oriented. It is this effect, we will employ to study the deposition of organs.

In chapter 2.3, we have introduced a description for the migration machinery of individual cells by use of attachment points. This description integrates the search behaviour of the cells, formation of focal adhesions and their elastic coupling to the cell body. By extension of the energy of the lattice model, coupling of the lattice and vertices was established. Vertex configurations obtained by minimisation of the energy and the attachment points dynamics was assumed to be subject to a random force. This framework allows to couple directional migration of cells as described here. For simplicity, we remove the random forces and consider the deterministic equations.

We consider a lattice with N cells α connected with their nearest neighbour by a spring with spring constant k that is relaxed at length l_0 as shown in fig. 3.7 A) and previously developed in eq. (2.4). An individual cell α comprises two elastically coupled vertices q_i, q_{i+1}, where the cell centre is elastically coupled to the attachment points R_i, reflecting the contractile acto-myosin filaments involved in migration, that are connected to the focal adhesions. Together we have $\mathbf{q} = (q_1, \ldots, q_{N+1})$, $\mathbf{R} = (R_1, \ldots, R_N)$ and rest lengths $\mathcal{L} = (l_0, \ldots, l_0)$. Attachment points are directed along the gradient of ligand via a coupling constant ζ, reflecting the translation of the gradient into a crawling velocity of the cells, i.e. $v_{max,\alpha} = \zeta \langle \nabla s \rangle_\alpha$. The gradient is averaged along the extension of an individual cell, and the dynamics are then given

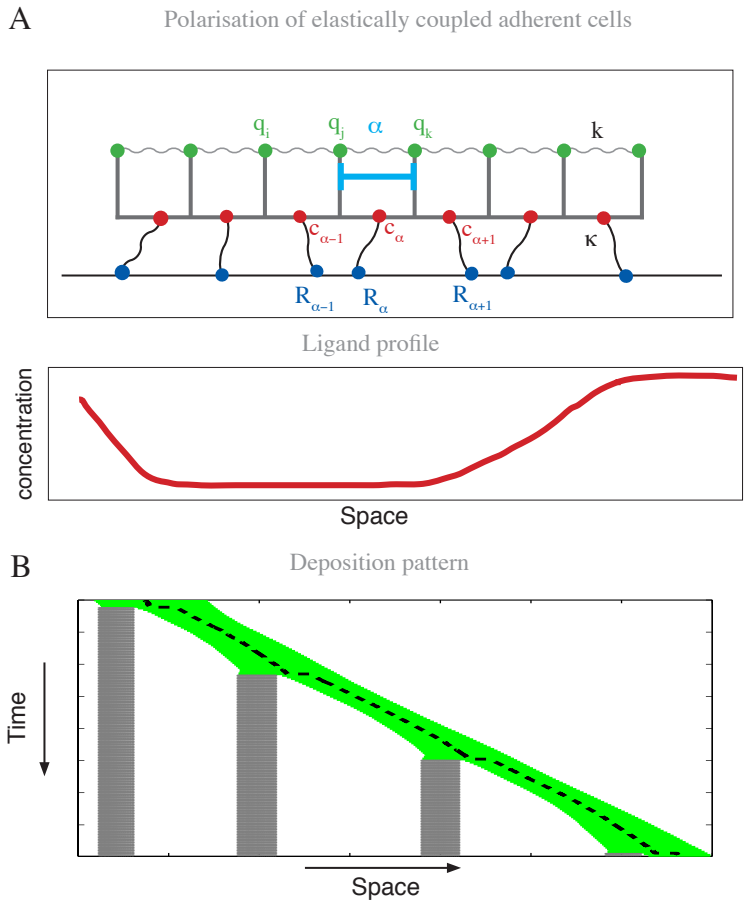

Figure 3.7: Deposition of cell clusters due to local differences in guidance information. A) One dimensional approximation of cell collective as previously developed. Elastic cells described by vertices q_α are coupled to attachment points R_α, which move in a polarisation field provided by the ligand. Lower panel shows the ligand profile concentration, that provides the directional information for attachment points depending on their position in the collective B) Simulation results with deposition. Deposited parts are dotted grey, lattice shown as solid green lines and centre of mass of the lattice as a dashed black line. The lattice moves to the right and grows at a rate η until a critical length is reached, which leads to deposition of cells. The vertices of the cells are considered removed from the lattice. The remainder continues migration.

by the following coupled system of equations:[1]

$$
\begin{aligned}
E(\mathbf{q},\mathbf{R}) &= \frac{1}{2}\sum_{i=1}^{N}\left\{k\left(q_{i+1}-q_i-l_0\right)^2+\kappa\left(R_i-\frac{q_{i+1}+q_i}{2}\right)^2\right\}\\
\mathbf{q} &= M^{-1}\left(\frac{\kappa}{2}C^T\mathbf{R}+L\mathcal{L}\right)\\
\dot{R}_i &= -\frac{\kappa}{\nu}\left(R_i-\frac{q_{i+1}+q_i}{2}\right)+\zeta\langle\nabla s\rangle_\alpha\\
\partial_t s &= D\partial_{xx}s-\sum_{i=1}^{N}\mu(x-\frac{q_{i+1}+q_i}{2})s+\gamma.
\end{aligned}
$$

Vertex positions $\mathbf{q}$ are subject to minimisation of the energy $E(\mathbf{q},\mathbf{R})$, which results in the above equation as discussed earlier. $(q_{i+1}+q_i)/2$ describes the centre of mass for each cell, and thus, we have to sum over all cells, to describe the interactions between lattice and ligand. Cell-division is incorporated with rate η equal over all positions along the lattice and constant. A new cell is introduced between two existing cells if a uniform distributed random number less than η is drawn. Given a dividing cell, a cleavage point, describing the division process is introduced in the lattice and the connection between the two adjacent old vertices is then on each end replaced with the new vertex and a new attachment point assigned to the new cells at its centre position. For simplicity, we neglect cell growth and assume the rest length of the daughter cells is given by that of the mother. To describe the deposition process, we assume that once the averaged gradient along the m rear most points falls below a threshold ϑ, these cells are considered deposited and removed from the lattice. The initial condition is given by a fixed number of cells at rest length with attachment points at the cells centre of mass and an anisotropic preformed ligand profile.

We performed simulations of a growing lattice moving along dynamically maintained gradients. A resulting deposition pattern is shown in fig. 3.7 B). The y-axis shows the time running from top to bottom and the x-axis denotes the position of the lattice, which is plotted as a green line in space. The ejected points are shown

[1]Expression for M, C and L are in the appendix

as grey dots and the centre of mass of the lattice is plotted as a black dashed line. Here, one observes deposition of the last third of cells in a regular pattern.

To study the pattern of deposition in more detail, we return to the continuous description of the rod and consider the rear most part a, where $0 \leq a \leq 2L(t)$. The rod is assumed to grow according to $L(t) = L_0 e^{\eta t}$, where L_0 denotes the initial length. The condition for a deposition of the rear most part a to occur is reached if the averaged gradient between $-L(t)$ and $-L(t) + a$ coincides with ϑ

$$D(L) := \int_{-L(t)}^{-L(t)+a} (Ae^{\lambda_-^{(2)}\xi} + Be^{\lambda_+^{(2)}\xi})d\xi = a\vartheta. \tag{3.8}$$

Eq. (3.8) gives a transcendental equation for the critical length L_{dep}, at which deposition occurs

$$\frac{2A(L_{dep})}{\lambda_-^{(2)}} e^{\lambda_-^{(2)}(\frac{a}{2}-L_{dep})} \sinh\left(\frac{\lambda_-^{(2)}a}{2}\right) + \frac{2B(L_{dep})}{\lambda_+^{(2)}} e^{\lambda_+^{(2)}(\frac{a}{2}-L_{dep})} \sinh\left(\frac{\lambda_+^{(2)}a}{2}\right) = a\vartheta. \tag{3.9}$$

A linearised version of the lhs of eq. (3.9), which is given by $D(0) + LD'(0) = a\vartheta$ may be solved for L_{dep}, which is shown in the appendix. Solving $L_{dep} = L_0 e^{\eta t_{dep}}$ for t_{dep} we obtain a critical time

$$t_{dep} = \frac{1}{\eta} \ln\left(\frac{L_{dep}}{L_0}\right),$$

which describes when the deposition of the rear part a will happen. The first order approximation of the deposition time t_{dep} is inversely proportional to the division rate η, i.e. the longer it takes for cells to divide, the longer it will take to reach the critical length for deposition. Furthermore it depends only logarithmically on the ratio between the length critical for deposition and the initial length L_0. Negative deposition times as they occur for $L_0 > L_{dep}$ simply indicated that the deposition requirement was already reached before. If the velocity remains roughly constant during the growth process, we may write the distance until a deposition occurs as $\Delta_{dep} = vt_{dep}$, which suggests that the deposited groups are spaced further away from

each other if the division rate of cells is reduced.

We have observed, that a tissue is able to store its velocity in the ligands' profile by actively shaping it in a one dimensional approximation. In the next section, we will discuss the two dimensional case.

3.3.3 Stress induced by dynamically maintained gradients

The one dimensional version of our ligand receptor model showed that many solutions supporting establishment and maintenance of gradients by the tissue exist. We have coupled it to the one dimensional description of a motile lattice and numerical simulations showed that the system is stable and able to deposit clusters.

We have observed that an exponential profile becomes established, which approaches a steady state value in the bulk of the tissue. Motion along the gradient of such a profile will result in different displacement strengths of the individuals, stress should build up. We will discuss this in the two dimensional case by numerical simulation and consider the resulting consequences of motion along dynamically maintained gradients on the mechanics of the tissue. Thus, we couple the two dimensional version of our model to the two dimensional version of the motile lattice model as developed in 2.3.

Extension of the one dimensional model for mechanically coupled cells with attachment points directionality imposed by chemical signalling fields to the two dimensional lattice model is as follows. Attachment point $\mathbf{R}_\alpha$ update in the direction of the mean gradient along the tissues extension, that is eq. (3.2) is replaced by

$$\dot{\mathbf{R}}_\alpha = -\frac{1}{\nu} grad_{\mathbf{R}_\alpha}(E) + \zeta \langle \nabla s \rangle_\alpha + \xi_\alpha, \tag{3.10}$$

and the vertices' dynamics are subject to minimisation of an energy function that involves the elastic properties of an epithelium coupled to attachment points as described in chapter 2.3:

$$E(q_1, \ldots, q_{N_V}) = \frac{1}{2} \sum_\alpha \left\{ \Lambda \varrho_\alpha + p \left(A_\alpha - A_0 \right)^2 + \kappa \left(\mathbf{R}_\alpha - \mathbf{C}_\alpha \right)^T \left(\mathbf{R}_\alpha - \mathbf{C}_\alpha \right) \right\}, \tag{3.11}$$

where $\mathbf{C}_\alpha$ denotes the centre of mass of cell α. The displacement of the attachment points is governed by the gradient of the ligand profile, which is determined by

$$\partial_t s(x,y) = D\Delta s(x,y) - \sum_\alpha \big(\sigma(x,y) + \rho H_\alpha(x,y)\big) s(x,y) + \gamma\delta(|y| < \epsilon), \qquad (3.12)$$

as described in the previous section. $H_\alpha(x,y)$ is one for $(x,y) \in Cell_\alpha$, vanishes otherwise and accounts with ρ for the increased ligand uptake due to internalisation by the cell. Without loss of generality, we confine the discussion to a fixed set of parameters governing the dynamics of the ligand. A hexagonal lattice in the ground state is chosen as a starting point for the subsequent simulations.

Fig. 3.8 shows a typical resulting ligand profile obtained by simulation with a given stripe width $\delta = 2\epsilon$. Along the migration axis of the lattice, similar to the one dimensional case, an exponentially dropping profile is observed. In addition, along the short axis, a gaussian shaped profile builds up for stripe widths δ smaller than or equal to the lattice width.

Migration along self generated gradients results in stronger displacements at the

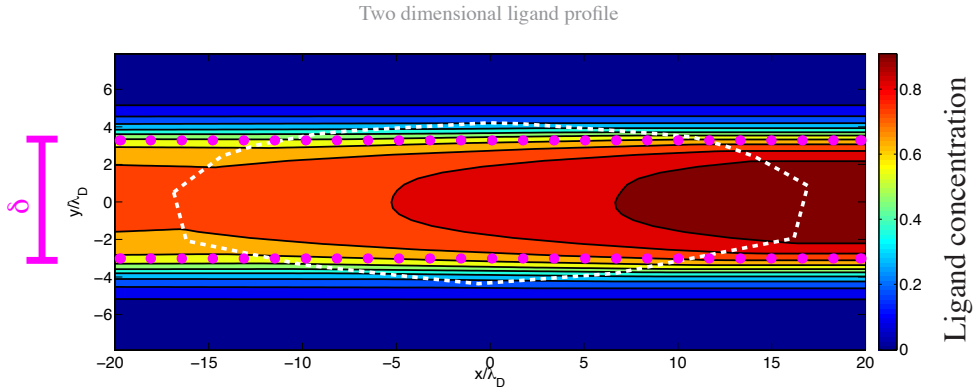

Figure 3.8: Ligand profile in two dimensions. Ligand profile over space in units of diffusion spread λ_D. Outline of lattice position indicated as white dashed line, production stripe extension δ indicated in magenta. Parallel to the direction of migration, the profile drops exponentially under the tissue, being highest at the tip. Orthogonal to the direction of migration, a gaussian shaped profile builds up.

front of the tissue than at the rear and subsequently to an elongation of the lattice and induce stress. Due to Cauchy's stress theorem, we can express the stress acting on a line at any point in the cell with unit normal $\mathbf{n}$ by $\mathbf{t} = \Sigma_\alpha \mathbf{n}$, where Σ_α denotes the symmetric stress tensor. According to [Landau91], the symmetric stress tensor Σ_α^{ab} for a cell α is given by the sum over all vertices in cell α and the forces acting on them

$$\Sigma_\alpha^{ab} = \frac{1}{2A_\alpha} \sum_{i \in \alpha} \left(q_i^a \frac{\partial E}{\partial q_i^b} + q_i^b \frac{\partial E}{\partial q_i^a} \right), \tag{3.13}$$

with a denoting the individual components of the vector $\mathbf{q}_i$.

As the energy function eq. (3.11), governing the mechanics of the lattice is a sum of the perimeter and area term, the stress tensor may be considered as a sum of the stress tensor due to the perimeter term $\Sigma_{\rho\alpha}$ and due to the areal term $\Sigma_{A\alpha}$, which are given by the following equations:

$$\Sigma_{\rho\alpha} = \frac{1}{2A_\alpha} \sum_{k \in \alpha} \frac{1}{q_{k,k-1}} \begin{pmatrix} (x_k - x_{k-1})^2 & (x_k - x_{k-1})(y_k - y_{k-1}) \\ (x_k - x_{k-1})(y_k - y_{k-1}) & (y_k - y_{k-1})^2 \end{pmatrix}$$

$$\Sigma_{A\alpha} = \frac{p(A_\alpha - A_0)}{2A_\alpha} \sum_{k \in \alpha} \begin{pmatrix} 2x_k(y_{k+1,k-1}) & x_k x_{k-1,k+1} + y_k(y_{k+1,k-1}) \\ x_k(x_{k-1,k+1}) + y_k(y_{k+1,k-1}) & 2y_k(x_{k-1,k+1}) \end{pmatrix},$$

with $q_{i,j} = |\mathbf{q}_i - \mathbf{q}_j|$ and the components of $q_i = (x_i, y_i)$, where $y_{i,j} = y_i - y_j$, $x_{i,j} = x_i - x_j$.

Fig. 3.9 A) shows an example of the magnitude of the mean stress in the tissue $||\langle t(\beta) \rangle||$ as a function of the line with normal vector $\mathbf{n}(\beta) = (\cos(\beta), \sin(\beta)))^T$ crossing through the cells, where $\langle \cdot \rangle$ denotes averaging of cells within the lattice and $\| \cdot \|$ the norm of a vector. The stress is anisotropic distributed with maxima around $\pm\pi, 0$ and minima observed at $\pm\frac{\pi}{2}$. A fit $A(t)\sin(2\beta + \phi(t))$ to the stress as a function of the angle β is shown as a red dashed line in fig. 3.9 A). Fig. 3.9 B) shows the temporal evolution of the amplitude and the phase of the fit measured in units of the number π. The amplitude vanishes at the beginning of the simulation, as there is no stress in the ground state, increasing with t until a saturation is reached after

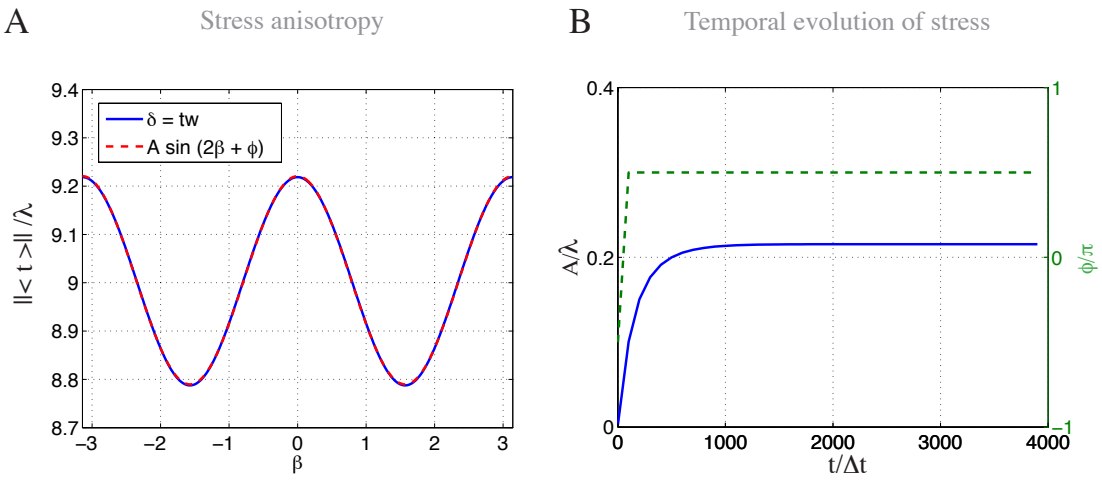

Figure 3.9: Stress distribution in response to response to directional motion. A) Example of mean stress of the cells in the lattice against normal vectors angle β with direction of migration shown in blue. A Fit of $A(t)\sin(2\beta + \phi(t))$ against mean stress shown as red dashed line. B) Temporal evolution of the fit parameters $A(t)/\lambda$ shown in blue and $\phi(t)$ shown in green. The ground state has no anisotropy, as $A(0)/\lambda = 0$. With increasing simulation runs, the stress increases and reaches a saturation after about 2000 runs. The phase $\phi(t)/\pi$ remains at the value of 0.5, indicating that stress is high in direction of migration and low in the transverse direction.

about 2000 simulation runs. $\phi(t)$ reaches a constant value of $\frac{\phi}{\pi} = 0.5$, indicating a high stress for $\beta = 0, \pm\pi$ and low stress for $\beta = \pm\frac{\pi}{2}$. From this we can conclude, that the migration induces a stress anisotropy in the tissue, with maximum in the direction of migration for the shown example. It is clear that with increasing ligand expression stripe width, that the stress distribution in the tissue will change. For values less or equal to the tissues width, we find agreement with the result presented here.

In the next section, we will experimentally probe the directionality of individual cells in the pLLP, followed by indirect measurements, on stress in the tissue.

3.4 Mechanics of directional migration

Our experimental analysis showed that the tissues motion is highly ordered, with an increased internuclear distance in the direction of migration. This is explained by our model, as it predicts a locally different signalling molecule concentration. Such a local difference should be reflected in the polarity of individual cells in the tissue. From the two dimensional profile of the ligand distribution, we would expect to observe polarisation of individuals depending on the position within the tissue, pointing towards the tissue midline. The model predicts that such a motion results in an anisotropic stress distribution. Here we will test this hypothesis by direct measurements of directionality of individual cells and stress on junctions.

3.4.1 Understanding directionality of individual cells

Motility of cells is based on an active rearrangement of the actin cytoskeleton, where the lamellipodium, an actin rich flat meshwork projects from the cell into the surrounding space [Alberts08]. Thin long spiky structures present in the lamellipodium are identified as filopodia if they extend beyond the lamellipodium. During the nucleation of lamellipodia and filopdia, the membrane of the cell is pushed forward and then focal adhesions form behind the leading edge of the cell, which then stabilise the cells new position. Live labelling of actin is allowed by the F-Actin marker lifeact [Riedl08] and provides a dynamic read out of the motility of individual cells.

In order to simplify identification of single cells, Lifeact-ruby-mRNA is injected into embryos with membrane marker at the single cell stage, and then labelled cells are transplanted into another primordium with only membrane marker, which results in a mosaic tissue with one or more isolated cell clones with Lifact-ruby-mRNA label. An example maximum intensity projection of a clone-cell with Lifeact-ruby-mRNA transplanted into a membrane labelled pLLP is shown in fig. 3.10 A) over four different time-points with a scale bar of 10 μm. The lifact label is present in the entire cell, but enriched along the leading edge], visible by a transient locally restricted increased lifact signal - so-called actin bursts - at the position of the lamellipodia. Filopodia point predominantly along the direction of migration for the presented cell.

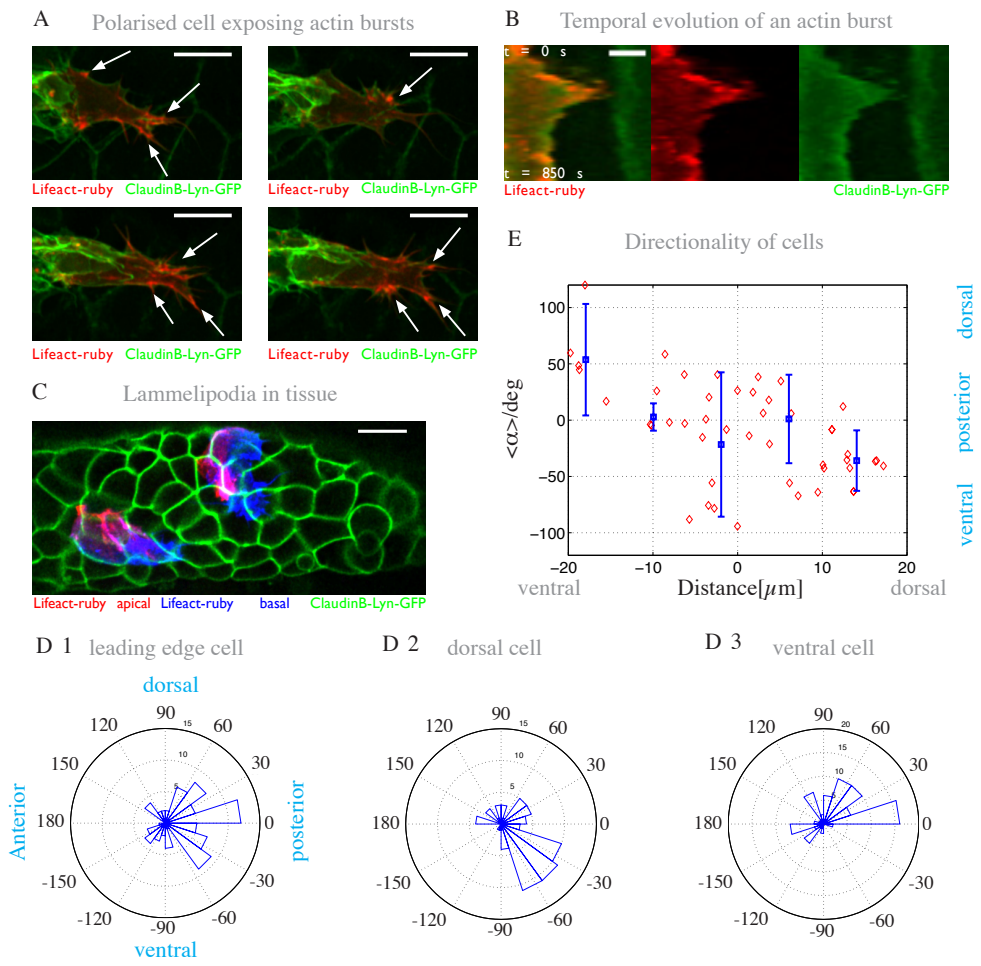

Figure 3.10: Protrusions of epithelial cells. A) Clone with lifeact-ruby cell at leading edge shown in the red channel and ClaudinB-lyn-GFP expressing cells shown in the green channel. Scale bar is 10 μm. White arrows are a guide for the eye. B) Kymograph of actin bursts. Red channel shows life-act ruby and green channel membrane signal. Scale bar is 3 μm, time runs from top starting at $t = 0$ *sec* to bottom finishing at $t = 850$ *sec*. C) Basal lifeact-ruby separated from apical lifeact-ruby. Plane of separation is shown in green with ClaudinB-lyn-GFP marker. Scale bar is 10 μm. D) Rose plots of angle of detected bursts for 3 representative cell positions: D1) Leading edge, D2) Dorsal and D3) ventral cell. Blue text at 0, ± 90, ± 180 degrees indicates anatomical direction in the fish. E) Mean angle $< \alpha >$ of cells' bursts against distance on dorso-ventral axis around midline of the pLLP. The distance from the midline for the part dorsal from the midline is positive, indicated by dorsal label along x-axis, ventral from the midline is negative indicated by ventral label along x-axis. Blue text as D).

A kymograph shows the temporal evolution of an actin burst in fig. 3.10 B), where the red channel shows the evolution of the lifact signal and the green channel shows the evolution of the membrane. The scale bar indicates 3 μm, time is running along the y-axis, with $t = 0\ s$ and $t = 850\ s$ indicating start and end of the experiment. Shortly after the beginning of the experiment, the enriched lifact signal extends forward, coinciding with an advancement of the membrane. Upon reaching a maximum extension of the membrane, the actin signal reduces again and the membrane retracts, until the actin and the cells membrane become stabilised again. Comparing the membrane position at the beginning of the experiment with the end of the experiment, a net displacement caused by localised transient actin enrichment is observed, showing that the actin bursts provide a read out for the directionality of an individual cell.

Cells at the leading edge are flat mesenchymal like, whereas cells in the trailing part of the pLLP show the character of tall epithelial cells. Fig. 3.10 C) shows a lifeact-ruby clone in the trailing part of the pLLP. Two cells on the dorsal part as well as ventral part of the tissue are labelled. In the apical part, lifeact is enriched along the membrane interfaces. Basally, so-called cryptic lamellipodia extend below the neighbouring cells. The direction of the lamellipodia of individual cells on the dorsal part is towards the midline and direction of migration. This demonstration of active protrusions in cells within epithelia is contrary to the suggestion that motility is contact inhibited within collectives.

In order to get rid of the moving but otherwise stationary signal, images of subsequent time point are shifted such that the correlation between the two time points is maximised. This corrects for the motion of the tissue and allows for a direct comparison of the signal for different times at the same position within the tissue. Taking the difference between the shift corrected image and its predecessor, a simple threshold allows to segment parts of the image, where the signal has increased above the given threshold, resulting in an accurate identification of bursts.

To analyse the direction of the lamellipodia extending from individual cells, a computerised segmentation of actin bursts was performed. For segmented bursts, the angle of the signal from the centre of mass of the corresponding cell is noted,

as well as the position of the cell within the tissue. Fig. 3.10 D) shows a rose plot of the angle α of the bursts for 3 representative cells within the tissue, D1) shows that cells on the leading edge predominantly enrich actin in the posterior direction, i.e. the direction of migration. Fig. 3.10 D2) provides an example of a dorsal cell, which send most protrusions in the superposition of ventral and posterior direction, whereas in fig 3.10 D3), one observes that ventral cells send most protrusions in the superposition of dorsal and posterior direction.

The compiled analysis of the mean direction of lamellipodia is shown in fig. 3.10 E) with original data points shown as red diamonds. 0 μm indicates the midline and positive distances the dorsal part, negative distances the ventral part of the tissue. The blue label is a guide for the direction where the cells point to, with respect to the anatomical directions of the fish. Ventral cells predominantly point in the dorsal and posterior direction, whereas dorsal cells preferentially point in the ventral and posterior direction. Cells around the midline point in the posterior direction, i.e. the direction of migration.

From this one may conclude, that individual cells have the desire to migrate towards the midline of the tissue. Cells on the midline nucleate lamellipodia in the direction of migration and cells away from the midline nucleate lamellipodia towards the midline and the direction of migration.

3.4.2 Probing the stress distribution in the posterior lateral line primordium

We have showed that cells point towards the midline of the tissue, as expected from the model. Now, we will test the stress distribution in the tissue. An approximation of the stress distribution in the tissue is provided by locally ablating cell junctions and measuring the relaxation between adjacent vertices, under the assumption that no tissue intrinsic stresses mediated by for instance preferential directions of the cytoskeleton exist [Farhadifar07, Rauzi08].

Furthermore, assuming mechanical equilibrium at each vertex, the forces pulling on the vertex at $t = 0$ before cut must cancel out, that is $\sum_i \mathbf{f}_i(t = 0) = \mathbf{0}$, as shown

in fig. 3.11 G). Upon cut of a junction, as indicated by a green dashed line in fig. 3.11 G), a vertex experiences the remaining forces $\mathbf{f}_1(t=0)+\mathbf{f}_2(t=0)$. Assuming a drag coefficient η, the maximal velocity after cut may be related to the remaining forces $v_{max} = \frac{\|\mathbf{f}_1(t=0)+\mathbf{f}_2(t=0)\|}{\eta}$ and hence it is related to tension in the cut junction just before the ablation. Thus under the above assumptions, v_{max} allows us to asses the relative difference of tension throughout the tissue.

In order to determine the relaxation speeds in the tissue, we performed diffraction limited laser ablation experiments. Junctions where cut using a UV laser light pulse, and the relaxation of the vertices formerly connected by that junction monitored. Fig. 3.11 A) shows a pLLP with a cut junction on the anterior part, the evolution of the vertices position is shown in fig. 3.11 B) and the distance between the vertices on each end of the junction as a function of time is plotted in fig. 3.11 C) as a blue line. $t = 0$ indicates the time just before cut and $\alpha = 7.3$ indicates the angle in degrees between the direction of migration and the junction, as indicated by the schematic in fig. 3.11 G). Before the cut, the distance between the vertices fluctuates around the mean position and after cut, the distance increases rapidly. After about 15 seconds, the distance between the vertices reduces again. Note that wound healing, a natural response to tissue damage triggered by the cut happens only on scales large compared to the relaxation scales observed here. Fig. 3.11 D) shows a pLLP with a cut junction in the middle of the tissue. The angle between the junction and the direction of migration is $\alpha = 54.5$ degrees and the relaxation after cut is shown in fig. 3.11 E) and F) respectively. Note that compared to the example in fig. 3.11 A)-C), the distance between the junctions increases significantly slower and also the magnitude of the increase is reduced.

The maximal velocity just after cut is obtained by a fit of a straight line to the relaxation curves, as shown in fig. 3.11 C) and F) as a red line. The velocity of the junction with a low angle compared to the direction of migration is significantly increased compared to the velocity of the junction with a high angle.

The cutting experiment was repeated over 34 wild type and 26 mutant primordia where the distance to the tip of the tissue, the angle of the junction and the maximal velocity was identified. Fig. 3.12 A) shows the maximal velocity against the angle

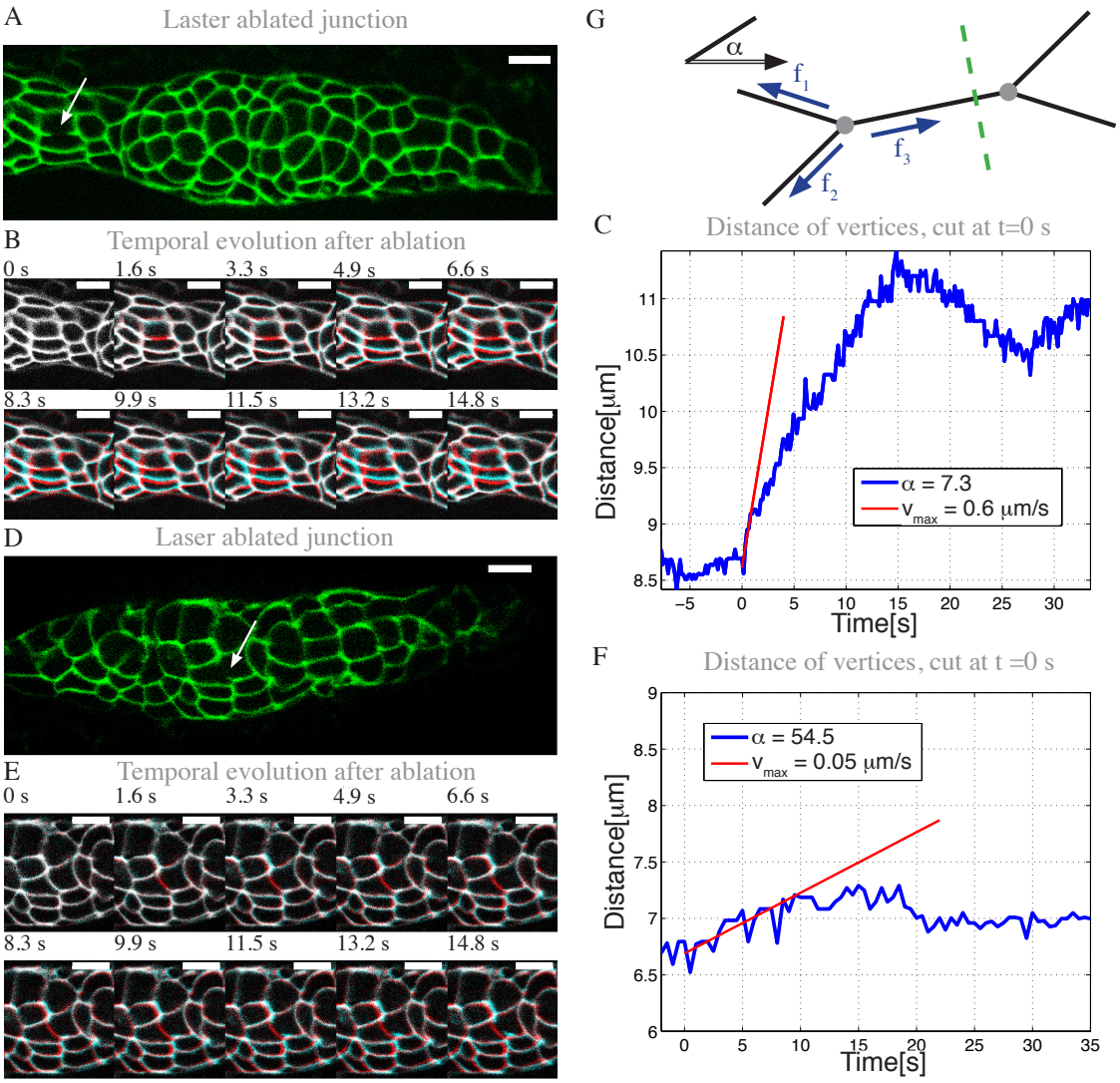

Figure 3.11: Stress distribution measurements. A) Scale Bar 10 μ m, arrow indicates site of ablation. B) Scale Bar 10 μ m. Red channel shows configuration before cut, cyan channel shows temporal evolution. 0 indicates last time point before cut. C) Relaxation between vertices in microns as function of time plotted as blue line. Angle $\alpha = 7.3$ degrees between direction of migration and junction. Red line shows linear fit to initial velocity. D) As A). E) As B). F) Relaxation between vertices in microns as function of time. Angle $\alpha = 54.5$ degrees between direction of migration and junction. G) Schematic of cutting procedure. Forces acting on vertices are indicated by blue arrows, dashed green line indicates cutting of junction, α denotes angle between junction and direction of migration.

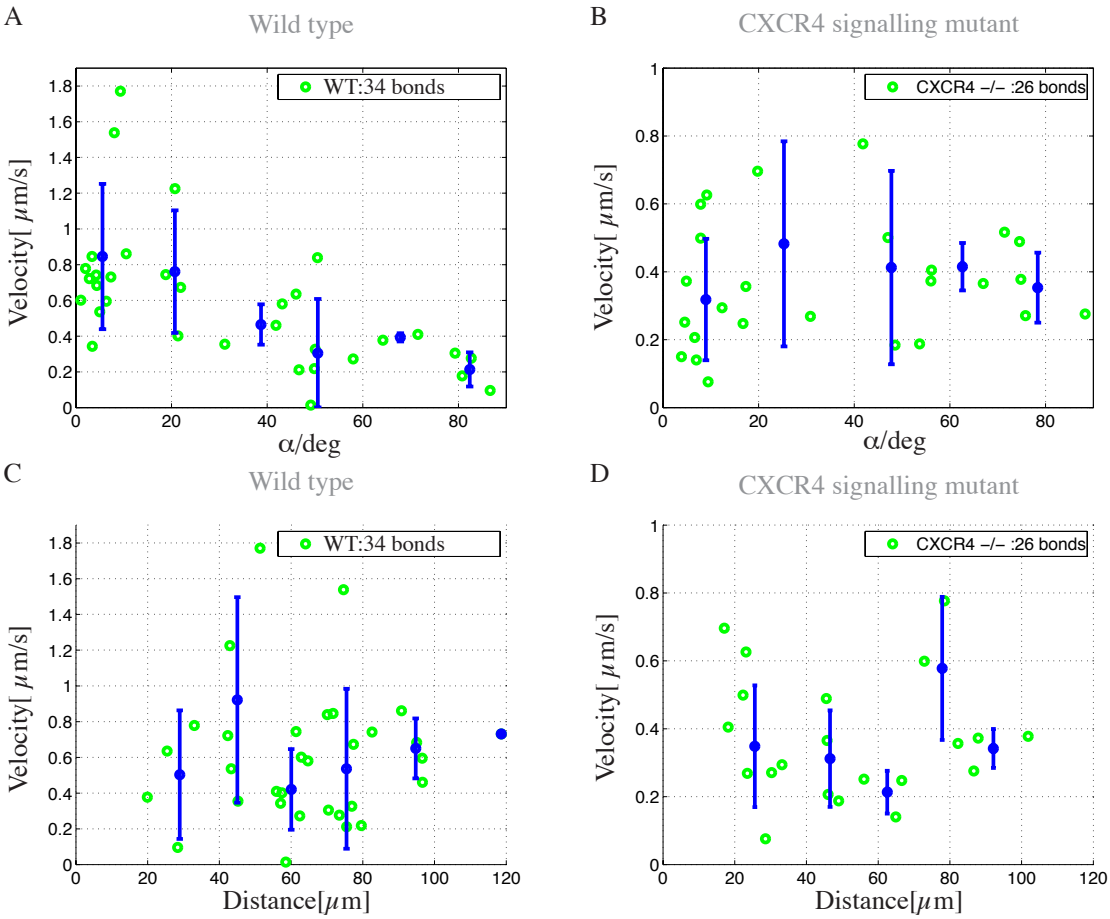

Figure 3.12: Anisotropic stress distribution due to directional migration of epithelia. A) Maximal relaxation speed v_{max} against α in degrees. Green dots are from 34 WT measurements, blue circles indicate mean in bins and errorbars indicate standard deviation. B) Maximal relaxation speed v_{max} against α in degrees. Green dots are from 26 CXCR4 mutant measurements, blue circles indicate mean in bin and bars indicate standard deviation. C) Maximal relaxation speed v_{max} against distance of cut junction from tip in μm. Green dots are from 34 WT measurements, blue circles indicate mean in bin and errorbars indicate standard deviation. D) Maximal relaxation speed v_{max} against distance of cut junction from tip in μm. Green dots are from 26 CXCR4 mutant measurements, blue circles indicate mean in bin and errorbars indicate standard deviation.

of the junction for wild type primordia. The maximal relaxation speed is highest for junctions with an angle $\alpha < 20$ fluctuating around 0.9 $\frac{\mu m}{s}$ and decreases with increasing angle to a value around 0.2 $\frac{\mu m}{s}$ for junctions with an angle $\alpha > 80$ degrees. This suggests, that the tension is distributed anisotropic along wild type tissues, with high tension on junctions parallel to the direction of migration and low tension in junctions parallel to the minor axis of the tissue.

The tension anisotropy observed in wild type tissues could be explained by a tissue intrinsic increase of tension for preferred junction angles, due to e.g. cell intrinsic shape constraints. Therefore, a similar analysis with migration deficient primordia is shown in fig. 3.12 B). Here, the relaxation speed for junctions with low angles is significantly reduced, and no clear trend as a function of the angle is observed. This, together with the observed tension anisotropy in the wild type case suggests, that the pLLP specific motion induces a tension anisotropy.

The maximum relaxation velocity as a function of the distance to the tip is plotted in fig. 3.12 C) as green dots with mean and standard deviation as error bar in blue for six bins. v_{max} initially increases with increasing distance to the tip, until at about 50 μm - a transition zone between the mesenchymal and epithelial part of the tissue - it drops again. At the position of about 100 μm, an increased tension is again observed, which corresponds to a transition zone between two pro-neuromasts, where deposition occurs. In case of immobile primordia, the maximum relaxation velocity initially drops with the distance, until around 80 μm a maximum is reached, as shown in fig. 3.12 D). The increased relaxation speed at the transition zones between pro-neuromasts and also between the mesenchymal tip and the pro-neuromasts suggests, that the tension in transition zones is increased compared to the tension in pro-neuromasts. This may be caused by an increased adhesion between cells in pro-neuromasts, which could also be useful for the deposition of neuromasts, where the intermediate cells elongate and the neuromasts maintain their shape. The view would be that once a neuromast is slowed down enough compared to its neighbours, the cells between the pro-neuromast and its neighbour elongate due to the stress that builds up. This may also induce stress dependant proliferation, which we didn't consider here.

3.5 Summary

We have studied chemokine signalling mediated directional migration and found that wild type tissues comprise cells characterised by highly ordered directional migration, that induces a stretching in the tissue. Migration mutants show significantly reduced order, in conjunction with a reduced but not vanishing velocity of individuals. In case of wild type primordia, the magnitude of the velocity remains high and drops after approximately 100 μm. The correlation in direction of migration is higher than the correlation of mutant tissues.

We investigated a mechanism for migration based on chemokines that maintains the polarity necessary for migration by translating it into the profile of the ligand. We formulated the system in two dimensions and derived a one dimensional version. Assuming a self-consistent constant velocity, we solved the system and showed that self-consistent solutions exist and discussed the resulting ligand profiles.

Numerical analysis of the velocity showed that an optimal length exists, maximising the tissues velocity. For tissues above this critical length, an inverse dependence of the velocity on the tissues length is identified. A one dimensional elastic model of the tissue was employed to couple growth of discrete cells and investigate its consequences on deposition of cells based on a threshold criterion for the ligand gradient. Simulations showed, that deposition of discrete subunits, similar to neuromast deposition observed in the posterior lateral line primordium of Zebrafish, is supported by the model. We identified a critical length for deposition and showed the time for the next deposition to occur to be proportional to the inverse of the growth rate, which is a natural assumption to avoid overcrowding of cells or the tissue running thin of cells. We showed that the system also moves in two dimensions. Stress analysis showed that the stress through the tissue becomes anisotropic, with a maximum in the direction of migration.

Individual cells are found to be attracted to the centre of the tissue, identified by preferential formation of transient actin bursts at the edge of cells towards the centre and direction of migration. Motivated from the findings on the non-homogeneous motion and the inwards directed motion of individuals, we tested the stress distri-

bution throughout the tissue. We found that stress is anisotropic distributed in wild type tissues, with increased tension in the direction of migration and reduced tension in the transverse direction. Mutant tissues lack this anisotropy from which we concluded that the directed motion induces the tension anisotropy. Considering the relaxation speed as a function of distance from the tip, we identified regions of increased tension in the tissue, corresponding to transition zones between the mesenchymal part at the front and the rosettes on the one hand, and the position of intermediate cells, where the neuromasts become deposited on the other hand.

Chapter 4

Image analysis methods

Since the advent of the use of green fluorescent protein as a marker for the spatio temporal dynamics of specific proteins, fluorescence based imaging has emerged as a standard tool of studies spanning a number of length scales from the subcellular to tissue level [Chalfie94, Heim95, Lippincott-Schwartz03]. Extensive use is made of optical sectioning microscopes such as selective plane illumination microscopes or confocal microscopes in order to obtain images of a specimen. Images of the fluorescence emitted by the fluorescent protein upon excitation are recorded, resulting in a digital raster of the fluorescence distribution in the specimen [Huisken09, Krzic09].

It is desirable to obtain an automated identification of objects in the image volume, characterised by certain properties, usually high intensity. This is subject to the domain of image processing and segmentation. A multitude of segmentation methods exists, such as edge detection, thresholding methods or watershed segmentation [Gonzalez03]. In general, these methods discard physically imposed relationship among pixels belonging to an object, are sensitive to noise or require prior information of the position of the objects to be segmented provided in form of seeds.

Here, we will discuss an alternative segmentation of images, based on an integral approach, thus reducing sensitivity to noise, namely active contours. We will use similar methods that serve to describe epithelial tissues as a descriptor of objects in the image.

4.1 Variational active contours

The nucleus of a cell provides an excellent object to detect the position of a cell, necessary in order to reconstruct the path a cell takes. Nuclei tagged with a nuclear localisation signal provide a homogeneously labelled confined object. Examples are shown in fig. 2.12 A) and B). Optical sectioning provides a two or three dimensional grid of greyscale intensities representing the distribution of flurophores. The nuclei are then characterised by membership in a particular part of that distribution. The grid can also be understood as a subset of $\mathbb{R}^N$, $\Omega \subset \mathbb{R}^N$ with $N \in \{2, 3\}$ called the image plane or volume. Then the map $I : \Omega \to \mathbb{R}$, where each point in $\mathbf{x} \in \Omega$ is assigned an intensity value $\mathbf{x} \mapsto I(\mathbf{x})$ is called an image. Objects are characterised as connected subsets of the image plane or volume, which may be described by a curve or surface defining their boundary.

Active contours

Let $\Omega \subset \mathbb{R}^2$ be the image plane and $I : \Omega \to \mathbb{R}$, $(x, y) \mapsto I(x, y)$ denote an image. Assume for simplicity, that only one object in the image plane should be segmented, i.e. separated from the rest of the image. Such a separation of the image plane can be achieved by a closed curve $\gamma : [0, 1] \to \mathbb{R}^2$. Variational image segmentation methods or active contours consider suitably chosen energy functionals of such curves $E(\gamma)$, to obtain a formal definition of the notion of an optimal segmentation of the image. The curve is assumed to take a sequence of configurations, that subsequently reduce the energy approaching a minimum [Mitiche10].

The energy functionals considered are typically broken down in an image or data term, a curve intrinsic term and possible constraints, giving $E(\gamma) = E_{image}(\gamma) + E_{intrinsic}(\gamma) + E_{cons}(\gamma)$. The most common example is the Mumford-Shah model, that considers the partitioning of the image into N different objects

$$E_{MS} = \sum_{i=1}^{N} \left\{ \int_{int(\gamma_i)} (I(x, y) - \mu_i)^2 dxdy + el(\gamma_i) \right\} = E_{MS,image} + E_{MS,intrinsic}, \quad (4.1)$$

where $l(\gamma_i)$ is the length of the $i-th$ curve, μ_i a parameter describing the desired intensity of the pixels that belong to the interior of the curve denoted $int(\gamma_i)$ and e a free parameter [Mumford89]. According to [Paragios02, Cremers07], there is a nice interpretation for the configuration of the contours which minimises eq. (4.1) as the partitioning of the image plane $P(\Omega)$ with maximum a posterior probability

$$e^{-\beta E_{MS,image}} e^{-\beta E_{MS,intrinsic}} = \mathbb{P}(I \mid P(\Omega))\mathbb{P}(P(\Omega)).$$

This gives rise to the view of gaussian distributed intensity values around mean μ and a prior that favours minimised curve length characterising the objects. It also provides a very robust object description, that is less prone to noise than differentiation based methods, as it integrates over the interior of the curve. The prior may be understood as a constraint that enforces the curve to be smooth depending on the parameter e.

Implicit curve definition via level sets

Explicit parametrisation of the contours turns splitting and merging of objects in a difficult to computerise task. A way out of this is provided by an implicit definition of the curve via level sets [Caselles97, Osher03, Sethian08]. The curve is understood as the zero level of a higher dimensional function, the level sets function $\phi : \Omega \rightarrow \mathbb{R}$, that is

$$\gamma := \{\mathbf{x} \in \Omega \mid \phi(\mathbf{x}) = 0\} \tag{4.2}$$

$$\gamma_{in} := \{\mathbf{x} \in \Omega \mid \phi(\mathbf{x}) < 0\} \tag{4.3}$$

$$\gamma_{ext} := \{\mathbf{x} \in \Omega \mid \phi(\mathbf{x}) > 0\}, \tag{4.4}$$

where the signed distance function that computes the distance to the contour and assigns a minus to the interior provides an example. This allows for the reformulation of the energy functionals based on the curve in terms of the level sets function $E(\phi)$, which in case of the Mumford-Shah model eq. (4.1) with two regions in the image is

referred to as the Chan-Vese energy [Chan01]:

$$E_{CV}(\phi) = \int_{\Omega} \Big((I-\mu_1)^2 H(\phi) + (I-\mu_2)^2 (1-H(\phi)) + e\delta(\phi)\|\nabla\phi\| \Big) d\Omega, \qquad (4.5)$$

where $H(\phi)$ is the heaviside function, that vanishes on the exterior and equals one on the interior. μ_i denotes the mean foreground and background intensity and the first and second term compare the intensity of the image in the foreground to the foreground mean intensity or the background to the background mean intensity respectively. The third term is the curves measure expressed in the level sets formulation and gives the length of the zero level set upon integration over the image plane [Chang96]. A variational framework provides the equations of motion for the level sets function via gradient descent that guarantees a minimisation of the energy functional $E(\phi)$ [Caselles97, Solem05]:

$$\frac{\partial\phi}{\partial t} = -grad\Big(E(\phi)\Big)\|\nabla\phi\|. \qquad (4.6)$$

Variational active contours in the level sets framework provide a number of useful aspects for segmentation of the nuclei of a cell collective. Splitting or merging of objects does not require reparametrisation of the contours, useful in particular when the number of objects in the image is not known. The energy considered integrates over the image and thus is less noise sensitive an effect commonly present when imaging over short time scales. Furthermore, the interpretation as a model for gaussian distributed pixels around a mean seems natural for the homogeneously labelled nuclei as shown in fig. 2.12 A),B) and fig.3.2 A),B). Also the modular structure of the energy functional allows for intuitive extensions of the energy functional in order to improve the segmentation model. In the next section we will discuss extensions going beyond the prior that just constraints the zero level set to be of minimal size.

4.2 Biophysical image model

Active contours in the level sets framework provide a very powerful image analysis technique for biological images, as described above. Some limitations are reached especially in case of touching objects, heterogeneous foreground markers or out of focus imaging. Touching objects or out of focus imaging result in an overlap of objects, that is hard to separate in the above image model. Heterogeneity of objects can result in actual foreground objects to be assigned to the background. This may be overcome by segmenting the image with stepwise raising fore and background mean intensities and removing objects of the desired size. Alternatively, each object may be assigned its own level sets function as proposed in [Vese02]. This is also a key step in the following more natural approach to separation of overlapping objects.

The type of foreground objects that is considered here is characterised by a strict confinement of the foreground signal to a well defined volume. Thus image segmentation with active contours applied to such a class of images may be improved by considering shape priors, as reviewed in [Cremers07]. Inspired by the mechanics of epithelial cells as described in [Käfer07, Hufnagel07, Farhadifar07], which considers an energy functional comprising elasticity and a area constraint, we consider an extension of the energy functionals used for the evolution of active contours, that incorporates a description of elastic and confined objects such as nuclei.

Let $\gamma_0 \subset \mathbb{R}^n$ be the hypersurface defined by a level sets function $\phi_0 : \mathbb{R}^{n+1} \to \mathbb{R}$ representing the boundary of a given object, that is $\gamma_0 : \{\mathbf{x} \mid \phi_0(\mathbf{x}) = 0\}$. Then the perimeter of that object is the integral over the surface γ_0 with the surface measure $d\sigma$

$$E_{per}(\gamma) = \int_{\gamma_0} d\sigma. \tag{4.7}$$

The chan-vese energy [Chan01] already considers the perimeter of the enclosed object, there used to ensure smoothness of the surface. The level set expression of such a surface term is due to [Chang96] and given by

$$E_{per}(\phi) = e \int_{\mathbb{R}^{n+1}} \delta(\phi_0(\mathbf{x})) \|\nabla \phi_0(\mathbf{x})\| d\mathbf{x}. \tag{4.8}$$

and may be interpreted as analogue of a surface tension. The volume enclosed by the surface is given by $V = \int_{\mathbb{R}^{n+1}} H(\phi_0(\mathbf{x}))d\mathbf{x}$. Let V_0 denote the intrinsic volume that an objects is assumed to take, then the continuous analogue of the volume term of the lattice model is given by

$$E_{vol}(\phi) = \frac{p}{2}\Big(V - V_0\Big)^2 = \frac{p}{2}\Big(\int_{\mathbb{R}^{n+1}} H(\phi_0(\mathbf{x}))d\mathbf{x} - V_0\Big)^2. \tag{4.9}$$

An image usually consists of more than one object. In case of the lattice model, a collection of polygons in the lattice is considered, with well defined position, in particular individual polygons don't overlap. Description of multiple objects in the level sets framework requires the introduction of a family of level set functions $\phi_i : \mathbb{R}^{n+1} \to \mathbb{R}$ one for each object, where $i \in \{0, \ldots, N\}$. [Zhao96] consider the problem of multiple level sets functions and identify, that additional constraints must be implemented in order to ensure proper description of the objects. In the simplest case of two objects, a description with a single level sets function is sufficient, and the surface γ defines the boundary between one object, which is on the interior and the other object, which is on the exterior. There the motion of the interface is well defined and the objects always separated. If the two objects become described by separate level set functions, then there are two contours γ_1 and γ_2, as shown in fig. 4.1. These contours can in principle move independently from one another, which results in vacuum or overlaps. [Zhao96] solve the problem by introduction of the constraint, that each point in space should be covered such that it is interior of exactly one level sets function

$$E_{cons}(\phi_0, \ldots, \phi_N) = \frac{\lambda}{2}\int_{\mathbb{R}^{n+1}} \Bigg(\sum_{i=0}^{N} H\big(\phi_i(\mathbf{x})\big) - 1\Bigg)^2 d\mathbf{x}. \tag{4.10}$$

Before turning to the the formulation of the full model, we give a formal definition of the gradient descent on $N + 1$ level sets functions.

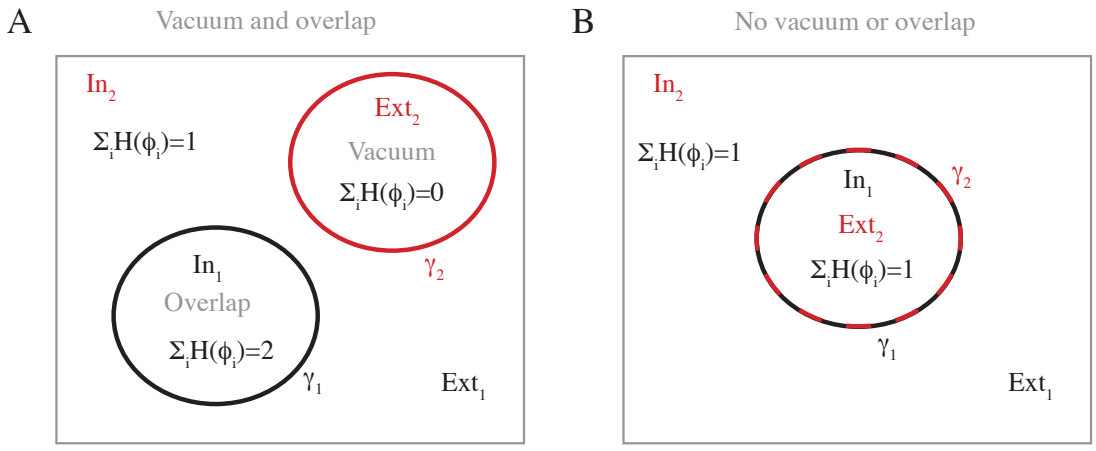

Figure 4.1: Prevention of vacuum and overlap. A) Two contours γ_1 and γ_2 are shown. The interior of γ_1, In_1 is enclosed by the black circle and the rest of the plane is the exterior Ext_1. The exterior Ext_2 of γ_2 is enclosed by the red circle and the interior In_2 is the rest of the plane. The contours don't overlap, and therefore $In_1 \cap In_2 \neq \emptyset$ interpreted as overlap of the regions , as indicated by $\sum_i H(\phi_i) = 2$ in that domain. $Ext_1 \cap Ext_2 \neq \emptyset$ is understood as vacuum, as $\sum_i H(\phi_i) = 0$ in that domain [Zhao96]. B) γ_1 and γ_2 overlap and no vacuum or overlap occurs as $Ext_1 \cap Ext_2 = \emptyset$ and $In_1 \cap In_2 = \emptyset$.

The manifold of multiple n-surfaces

Let $\phi_i : \mathbb{R}^{n+1} \times I \to \mathbb{R}$, $(\mathbf{x}, t) \mapsto \phi(\mathbf{x}, t)$ with $i \in \{0, \ldots, N\}$ be a family of level sets functions, each defining an evolving surface $\gamma_i(t) := \{\mathbf{x} \mid \phi_i(\mathbf{x}, t) = 0\}$. Let M denote the space of all possible evolutions of a surface γ_i with tangent space $T_{\gamma_i} M$ at the point $\gamma_i \in M$ as described in [Solem05], see appendix D. Then M^{N+1} is the space of all possible evolutions of $N+1$ surfaces with elements $\gamma \in M^{N+1}$ denoted as $\gamma = (\gamma_0, \ldots, \gamma_N)$ and tangent space at $\gamma \in M^{N+1}$ given by $T_\gamma M^{N+1} = T_{\gamma_0} M \times \ldots \times T_{\gamma_N} M$. To interpret a gradient of an energy functional in this space, we define the bilinear

form

$$\langle \cdot, \cdot \rangle_\gamma : T_\gamma M^{N+1} \times T_\gamma M^{N+1} \to \mathbb{R}$$
$$(\mathbf{v}, \mathbf{w}) \mapsto \langle \mathbf{v}, \mathbf{w} \rangle_\gamma := \sum_{i=0}^{N} \langle v_i, w_i \rangle_{\gamma_i},$$

with $v_i, w_i \in T_{\gamma_i} M$ and $\langle v, w \rangle_{\gamma_i} := \int_{\gamma_i} vw d\sigma$, where $d\sigma$ is the surface measure of $\gamma_i(t)$.

A biophysics based image energy

Now that we have the ingredients required to describe the $N+1$ level sets functions, we turn to the mechanics based image model. Let $I : \mathbb{R}^{n+1} \to \mathbb{R}$ be an image and $\mu_i(t) = \int_{\mathbb{R}^{n+1}} I(\mathbf{x}) H(\phi_i(\mathbf{x}, t)) d\mathbf{x} / \int_{\mathbb{R}^{n+1}} H(\phi_i(\mathbf{x}, t)) d\mathbf{x}$ denote the mean intensity of the image enclosed by the surface $\gamma_i(t)$. We choose the data term of the chan-vese energy [Chan01]

$$E_{image}(\phi_i) = \int_{\mathbb{R}^{n+1}} \big(I(\mathbf{x}) - \mu_i(t)\big)^2 H(\phi_i(\mathbf{x}, t)) d\mathbf{x} \tag{4.11}$$

and propose the following energy functional $E_{mech} : M^{N+1} \to \mathbb{R}$, with the mapping of evolving surfaces $(\gamma_0(t), \ldots, \gamma_N(t)) \mapsto E_{mech}(\gamma_0(t), \ldots, \gamma_N(t))$ to numbers, where $E_{mech}(\gamma_0, \ldots, \gamma_N)$ in the level sets frame work is defined as

$$\begin{aligned} E_{mech}(\phi) &= \sum_{i=0}^{N} \Big(E_{image}(\phi_i) + E_{per}(\phi_i) + E_{vol}(\phi_i) \Big) + E_{cons}(\phi_0, \ldots, \phi_N) \\ &= \sum_{i=0}^{N} \Big\{ \int_{\mathbb{R}^{n+1}} \big(I(\mathbf{x}) - \mu_i(t)\big)^2 H(\phi_i(\mathbf{x}, t)) + e\delta(\phi_i(\mathbf{x}, t)) \|\nabla \phi_i(\mathbf{x}, t)\| d\mathbf{x} \\ &\quad + \frac{p}{2} \Big(\int_{\mathbb{R}^{n+1}} H(\phi_i(\mathbf{x}, t)) d\mathbf{x} - V_{0,i} \Big)^2 \Big\} + \frac{\lambda}{2} \int_{\mathbb{R}^{n+1}} \Big(\sum_{i=0}^{N} H\big(\phi_i(\mathbf{x}, t)\big) - 1 \Big)^2 d\mathbf{x}. \end{aligned} \tag{4.12}$$

This describes gaussian distributed intensities around a mean μ_i subject to the prior that the contour is elastic, its volume around a preferred value $V_{0,i}$ and that no vacuum or overlaps exist. A similar functional without E_{vol} was successfully applied

to 2 dimensional images in [Samson99] as a classifier for objects of an a priori given μ_i. With the above defined bilinear form, we can use a generalised form of the gradient descent as described in the appendix D, to determine the descent evolution of the $N+1$ surfaces.

Derivation of equations of motion

To determine the gradient of the functional E_{mech} we consider a curve $\gamma(t)$ through a point $\gamma_0 \in M^{N+1}$ with $\dot{\gamma}(t) = v \in T_{\gamma(t)}M^{N+1}$, understood as a variation of the surface γ_0, that is $\gamma(0) = \gamma_0$. Then the gradient of E is defined as the unique vector, that satisfies $\langle gradE(\gamma(t)), \dot{\gamma}\rangle_\gamma = \frac{d}{dt}E_{mech}(\gamma(t))$. In the level sets formulation, we then have the following variation

$$\frac{d}{dt}E_{mech}(\phi(t)) = \frac{d}{dt}E_{image}(\phi(t)) + \frac{d}{dt}E_{per}(\phi(t)) + \frac{d}{dt}E_{vol}(\phi(t)) + \frac{d}{dt}E_{cons}(\phi(t)).$$

We now conduct the variation of the individual terms, starting with the image term. With $\frac{d}{dx}H(x) = \delta(x)$ as the delta function, we find

$$\begin{aligned}
\frac{d}{dt}E_{image}(\phi(t)) &= \int_{\mathbb{R}^{N+1}} \sum_{i=0}^{N} \big(I(\mathbf{x}) - \mu_i\big)^2 \delta(\phi_i(\mathbf{x},t))\dot{\phi}_i(\mathbf{x},t)d\mathbf{x} \\
&= \int_{\mathbb{R}^{N+1}} \sum_{i=0}^{N} \big(I(\mathbf{x}) - \mu_i\big)^2 \delta(\phi_i(\mathbf{x},t))\dot{\phi}_i(\mathbf{x},t)\frac{\|\nabla\phi_i(\mathbf{x},t)\|}{\|\nabla\phi_i(\mathbf{x},t)\|}d\mathbf{x} \\
&= -\int_{\mathbb{R}^{N+1}} \sum_{i=0}^{N} \big(I(\mathbf{x}) - \mu_i\big)^2 \dot{\gamma}_i(t)d\sigma_i = -\sum_{i=0}^{N} \langle \big(I - \mu_i\big)^2, \dot{\gamma}_i(t)\rangle_{\gamma_i},
\end{aligned} \tag{4.13}$$

where in the last step, the evolution equation for the surface $\gamma_i(t)$ due to the level sets equation $\frac{1}{\|\nabla\phi_i\|}\frac{\partial\phi(t)}{\partial t} = -\dot{\gamma}_i(t)$ (cf. eq. (D.2)), the measure on the surface $d\sigma_i$ as well as the definition of the bilinear form $\langle\cdot,\cdot\rangle_\gamma$ was used. Next we calculate the

variation of the constraint term

$$\begin{aligned}\frac{d}{dt}E_{cons}(\phi(t)) &= \lambda\int_{\mathbb{R}^{N+1}}\sum_{i=0}^{N}\Big(\sum_{k=0}^{N}H\big(\phi_k\big)-1\Big)\delta(\phi_i(\mathbf{x},t))\dot{\phi}_i(\mathbf{x},t)d\mathbf{x}\\ &= -\lambda\sum_{i=0}^{N}\langle\Big(\sum_{k=0}^{N}H\big(\phi_k\big)-1\Big),\dot{\gamma}_i(t)\rangle_{\gamma_i},\end{aligned} \tag{4.14}$$

where we used the same steps as previously. The volume term gives

$$\begin{aligned}\frac{d}{dt}E_{vol}(\phi(t)) &= p\int_{\mathbb{R}^{N+1}}\sum_{i=0}^{N}\Big(\int_{\mathbb{R}^{n+1}}H(\phi_i(\mathbf{x},t))d\mathbf{x}-V_{0,i}\Big)\delta(\phi_i(\mathbf{x},t))\dot{\phi}_i(\mathbf{x},t)d\mathbf{x}\\ &= -p\sum_{i=0}^{N}\langle V_i-V_{0,i},\dot{\gamma}_i(t)\rangle_{\gamma_i}\end{aligned} \tag{4.15}$$

and finally the perimeter term

$$\frac{d}{dt}E_{per}(\phi(t)) = \int_{\mathbb{R}^{N+1}}\sum_{i=0}^{N}\delta'(\phi_i(\mathbf{x},t))\|\nabla\phi_i(\mathbf{x},t)\|+\delta(\phi_i(\mathbf{x},t))\frac{d}{dt}\|\nabla\phi_i(\mathbf{x},t)\|d\mathbf{x}.$$

We have to calculate $\frac{d}{dt}\|\nabla\phi_i(\mathbf{x},t)\| = \sqrt{\nabla\phi_i(\mathbf{x},t)\cdot\nabla\phi_i(\mathbf{x},t)} = \frac{\nabla\phi_i(\mathbf{x},t)\cdot\nabla\dot{\phi}_i(\mathbf{x},t)}{\|\nabla\phi_i(\mathbf{x},t)\|}$. This gives

$$\begin{aligned}\frac{d}{dt}E_{per}(\phi(t)) &= e\int_{\mathbb{R}^{N+1}}\sum_{i=0}^{N}\delta'(\phi_i(\mathbf{x},t))\|\nabla\phi_i(\mathbf{x},t)\|\dot{\phi}_i+\delta(\phi_i(\mathbf{x},t))\frac{\nabla\phi_i(\mathbf{x},t)\cdot\nabla\dot{\phi}_i(\mathbf{x},t)}{\|\nabla\phi_i(\mathbf{x},t)\|}d\mathbf{x}\\ &= e\int_{\mathbb{R}^{N+1}}\sum_{i=0}^{N}\{\delta'(\phi_i)\|\nabla\phi_i\|\dot{\phi}_i-\delta'(\phi_i)\frac{\nabla\phi_i\cdot\nabla\phi_i}{\|\nabla\phi_i\|}\dot{\phi}_i-\delta(\phi_i)\nabla\Big(\frac{\nabla\phi_i}{\|\nabla\phi_i\|}\Big)\dot{\phi}_i\}d\mathbf{x}\\ &= -e\int_{\mathbb{R}^{N+1}}\sum_{i=0}^{N}\nabla\Big(\frac{\nabla\phi_i}{\|\nabla\phi_i\|}\Big)\frac{1}{\|\nabla\phi_i\|}\dot{\phi}_i\delta(\phi_i)\|\nabla\phi_i\|d\mathbf{x}\\ &= e\sum_{i=0}^{N}\langle\nabla\Big(\frac{\nabla\phi_i}{\|\nabla\phi_i\|}\Big),\dot{\gamma}_i(t)\rangle_{\gamma_i},\end{aligned} \tag{4.16}$$

where in the second step an integration by parts assuming that the variation of the level sets vanish on the boundaries was performed. For $N = 0$, the results for the perimeter and image term coincide with previously found results [Chan01, Solem05] and for $N > 0$ and $n = 1$, the image term, perimeter term and constraint term coincides with previous results [Zhao96, Samson99].$\kappa_i := -\nabla\left(\frac{\nabla\phi_i}{\|\nabla\phi_i\|}\right)$ is identified as the interfacial curvature. Assuming $p > 0$, the gradient of the volume term for the i-th surface is given by the difference between the volume enclosed by the surface and the reference volume $-p\big(V_i - V_{0,i}\big)$, decreasing if the intrinsic volume $V_{0,i}$ is smaller than the volume enclosed V_i. In the gradient descent scheme, which determines the motion of the contour, we thus get a positive contribution, leading to an increase of the value of the level set function, and thus a shrinking of the volume enclosed by the surface as desired.

Taking all terms together, the gradient of the functional in eq. 4.12 is given by

$$\langle grad\big(E_{mech}\big), \dot{\gamma}\rangle_\gamma = \\ -\sum_{i=0}^{N}\langle\big(I-\mu_i\big)^2 + e\kappa_i + p\big(V_i - V_{0,i}\big) + \lambda\left(\sum_{k=0}^{N}\big(\phi_k\big) - 1\right), \dot{\gamma}_i(t)\rangle_{\gamma_i},$$

and by gradient descent we have the following evolution equation for the level sets functions $\phi_i(\mathbf{x}, t)$

$$\dot{\phi}_i(\mathbf{x},t) = \|\nabla\phi_i\|\left(\big(I(\mathbf{x}) - \mu_i\big)^2 + e\kappa_i + p\big(V_i - V_0\big) + \lambda\left(\sum_{k=0}^{N} H\big(\phi_k\big) - 1\right)\right). \quad (4.17)$$

The curvature term in eq. (4.17) is proportional to $\sqrt[\frac{n+1}{2}]{V}$ and has the tendency to reduce the volume. The volume term in eq. (4.17) counter balances this tendency as for $V_i < V_0$, the volume enclosed by the zero level set of ϕ will increase. The data term $\big(I(\mathbf{x}) - \mu_i\big)^2$ ensures that parts of the image, which deviate much from μ_i will be removed from the interior of the i-th level sets function and the constraint term ensures that every point is partitioned such that it belongs to the interior of one and only one level sets function.

4.3 Biophysical image segmentation

The equations of motion of the mechanics based image functional eq. (4.17) is valid for any n, where in our case $n = 1$ for plane images and $n = 2$ for volumes may be considered. Keeping track of the entire level sets function family over all points in an image is cost intensive, as it requires evaluation of the update rule in the entire image volume. Sparse field methods employ the key to significantly reduce the amount of calculations. Using narrow bands, where the level sets function is evaluated on the contour and in two neighbouring bands - two inside and two outside - around the contour, reduce the amount of calculations to be in the range of the surface of the contour, thus speeding up the calculations significantly [Whitaker98, Lankton09].

Implementation of the equations of motions eq. (4.17) is based on an extension of the framework for sparse field methods explained and implemented in [Lankton09]. ϕ_i is chosen to be the signed distance function around the i-th contour and the $N+1$ contours as well as the two bands to the interior and exterior representing ϕ_i are initialised. Intrinsic volume for the N foreground objects is chosen to be constant V_0, whereas for the background object the intrinsic volume is updated at each time step to coincide with the volume enclosed by that surface. At each iteration step, in addition to the calculation of the update rule for each level set, connectivity of the objects using a connected components algorithm available in the matlab image processing toolbox is checked. When a level sets function splits according to the connectivity measure, a new level sets function becomes initialized, resulting in $N+2$ contours.

We then performed a synthetic test with three overlapping identical discs on the plane as shown in fig. 4.3 A). The initial condition is reached by the chan-vese level sets formulation [Chan01], which serves as definition point of two level sets functions one for the foreground and one for the background. The intrinsic area for the foreground objects is chosen to be $.8A_d$, with A_d as the area of an individual disc, the contour is considered soft, i.e. $e << 1$. This choice helps to split the curves more efficiently. The value of the functional E_{mech} as a function of simulation time steps is plotted in fig. 4.2 A). After the initiation process, the energy rapidly drops and

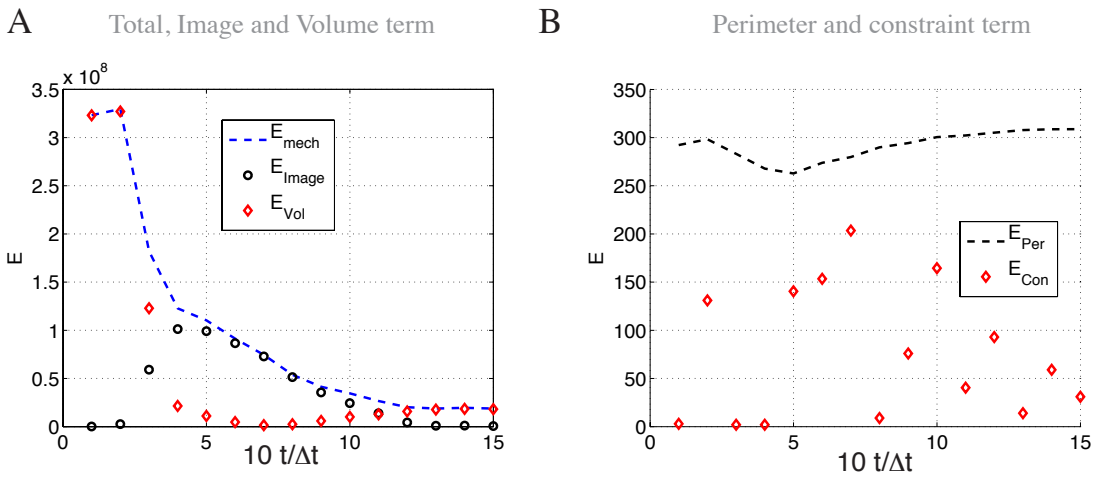

Figure 4.2: Image energy evolution. A) E_{mech} resulting from application to image shown in fig. 4.3 A), is shown as dashed blue line, data term E_{image} as black circles and E_{vol} ad red diamonds as a function of simulation time steps. B) E_{per} shown as black dashed line and E_{con} as red diamonds as function of simulation time steps.

converges towards the end of the segmentation process. The major contributions are from the image term E_{image} and the volume term E_{vol}, where the latter mostly drives the reduction in the beginning. As the area of the foreground object decreases, the contribution of the image term to the total energy increases. In the phase when the contours have split into individual objects as indicated in fig. 4.3 A), the largest term in the energy is that of the data term, and thus the deviation from the image value drives the contour. Finally, the energy converges to a constant value, where the data terms contribution is less than the contribution of the volume term.

As the contour here is modelled in the soft limit, i.e. small e, the perimeter term contributions are small as shown in fig. 4.2 B). Splitting of the contours also works in less elastic contours, resulting in a smoother contour but also longer execution time. The constraint term also contributes little, which shows that the image plane is properly partitioned. Particularly around the time of splitting of the objects, the constraint contributes most to the total energy, due to the fact that the vacuum occurring when two objects split is only filled with time by the background object.

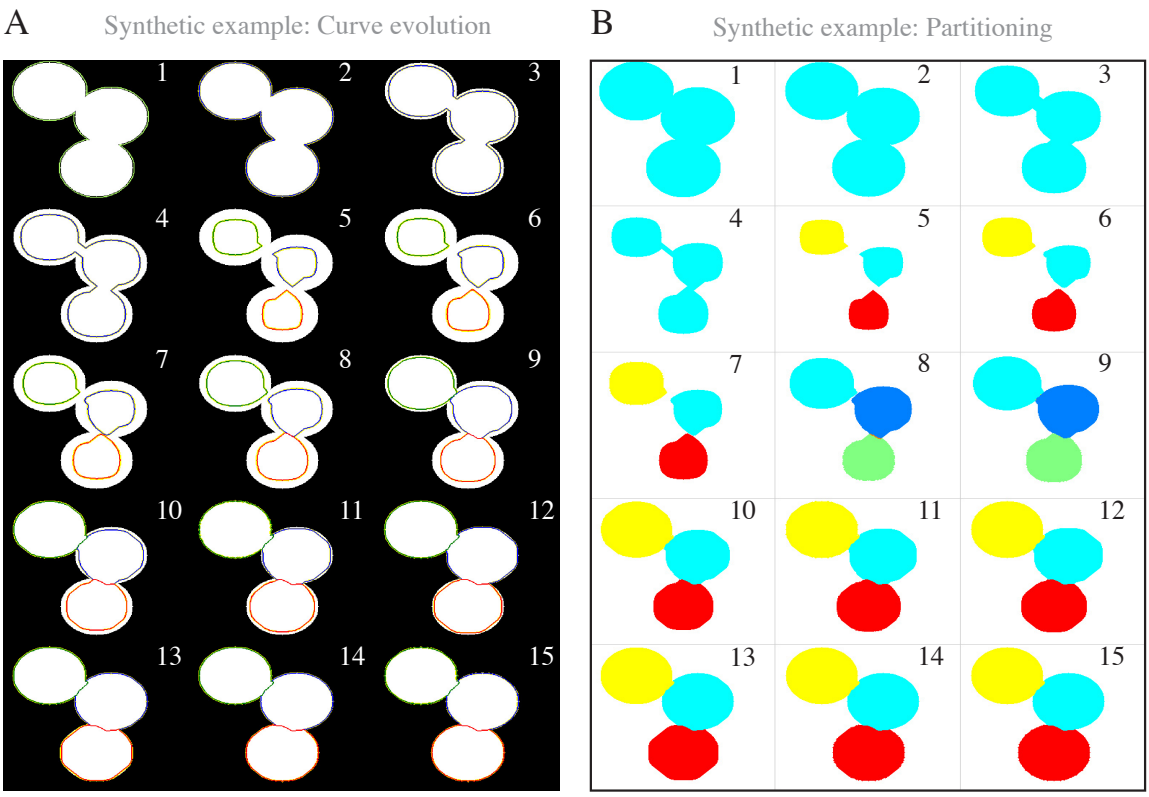

Figure 4.3: Contour evolution on a synthetic image. A) Black and white test image of three overlapping discs with identical foreground signal and identical radius. Sequence of evolution of the contour enclosing the detected objects is shown. Initial condition is a segmentation of the object based on the chan-vese energy [Chan01]. Then the foreground and the background are assigned to two level sets functions, i.e. two contours, where the background is shown in yellow and the foreground contours are in red and green. In the final image, an accurate segmentation is reached. B) The interior of the level sets functions of the foreground colour coded evolving over time. In the end of the experiment, three separated discs are identified.

Temporal evolution of the contours in the synthetic test with three overlapping identical discs is shown in fig. 4.3 A) and the interior of the contours shown in fig. 4.3 B). Driven by the deviation of the volume of the overlapping discs from the intrinsic volume, the contour shrinks and subsequently splits. The contours underestimate the volume of an individual disc and driven by the data term subsequently increase,

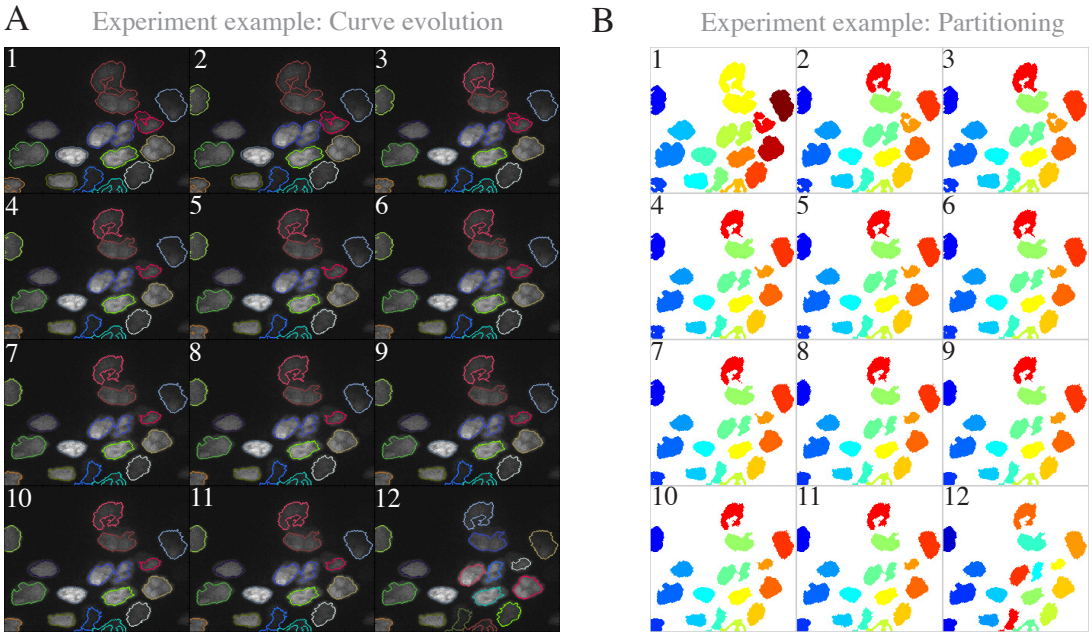

Figure 4.4: Contour evolution on a biophysical image A) Example cell culture image with nuclei of MDCK cells . Sequence of evolution of the contour enclosing the detected objects is shown. Initial condition is a segmentation of the objects based on a combination of filtering, thresholding and dilation operations. Objects are separated based on a connected components algorithm implemented in the image toolbox of matlab [Haralick92] and used as initial condition. The contours evolve and give an accurate partitioning of the image. B) The interior of the level sets functions of the foreground colour coded evolving over time.

until an accurate patterning into three discs covering the foreground is reached.

Fig. 4.4 shows an example segmentation of MDCK culture cells. The initial segmentation method is obtained by subsequent application of a mexican hat filter for edge detection, dilation and hole filling [Haralick92, Soille99, Gonzalez03]. Most nuclei are detected well, some are fused together. The individual objects are then each assigned a level sets function and the contours evolved as described in the synthetic example. μ_i in the image term is calculated as the mean value enclosed by the i-th contour. Similar to the synthetic case, after splitting, the objects tend to underestimate the volume and then increase again in size driven by the data term.

We have also successfully applied the above image model to volume data containing nuclei, with significant increase in execution time as well as memory usage, limiting realistic applicability to relatively small data-sets.

In general, we find that the contributions from image and volume term should be of the same order of magnitude, in order to achieve a satisfactory segmentation result. If the contribution of the data term is the leading part, then objects will not be split. On the other hand, if the volume terms contribution is overestimated, the contours tend to split irrespectively of objects present in the image. Such mal-segmentations can be avoided by a reasonable initial condition, where contours only enclose objects, but no background.

Such initial conditions can also help to speed up the segmentation process and increase the segmentation result in various ways. Using sparse field methods to update the level sets function, the only ways of changing the number of contours are provided by merging and splitting of individuals, hence a de-novo appearance of contours is not possible. Thus having an initial contour enclosing all objects in the image and as little background as possible, the contours don't have to become extended in order to enclose additional objects, saving computation time. Furthermore, updating a level sets function requires evaluation of the evolution equations on each point on the contour, becoming faster if the contour is tight.

The formulation of the image model should allow application of the model also to other types of images containing different tagged structures that overlap, such as crowded single cells. Furthermore, it is not limited to biologically motivated images, as it might become applied in the automated detection of essentially any type of overlapping objects with known volume.

4.4 Summary

In this section, we have discussed the advantages of the variational active contours in level sets frame work and its application to biological images. We identified that a formulation of the energy functional governing the contour motion including physical interpretation of objects in the image is a method to improve the segmentation result. We formulated the biophysical image model in the level sets frame work and derived the evolution equations for the level sets functions. We then showed that this energy function segments synthetic overlapping objects as well as real overlapping objects. We discussed the contribution of the individual parts of the energy functional and identified that the contributions from the image term as well as the volume term should be of a similar order of magnitude for proper object partitioning. We propose to use alternative methods to obtain a good initial condition for the mechanics based image segmentation in order to avoid appearance of mal-segmentations due to overestimated contributions from the volume term. Such a good initial condition could also be used to speed up the segmentation result.

Chapter 5

Conclusion

In this thesis, we have discussed the interplay of growth and migration of epithelial tissues, taking a combined approach of theory, experiment and data analysis. We considered two types of epithelia, one tissue covering a petri dish and another tissue moving through an embryo in response to chemokine signalling.

Using cultured MDCK cells, we have characterised the role of mechanics as a growth regulator, and identified regulatory mechanisms. We formulated a biophysical model for dynamic tissues to test the hypothesis and found that the model is able to reproduce the observations. With the same biophysical model for motility, coupled to chemokine signalling, we gave a possible explanation for organ deposition and stress distribution in the posterior lateral line primordium of zebrafish. Combined, this is a complementary study of the regulation of growth and motility, in vitro and in vivo.

Biophysical aspects of MET

We have conducted quantitative measurements on the mesenchymal to epithelial transition in growing tissues. We identified that exponential growth as observed for low cell densities takes place for several days, despite cell-cell contact. The transition to a sub-exponential expansion of the tissue is accompanied by density increase and reduction of cell motility. An increasing order appearing in the tissue

marks the time of morphological transition, where the tissue becomes characterised by a steady topology except for divisions. Continuous size reductive divisions result in shifting area distributions converging against a stationary area distribution. This is accompanied by a proliferation arrest in the tissues bulk.

By use of a model for motile tissues, we have shown that a cell size dependant growth rate together with finite velocity of cells and a plastic cell size increase can account for the observed patterns. An approximation for the critical time of the cross-over revealed a connection of the critical time to the proliferation rate and maximum crawling velocity of boundary cells. In the centre of the colony, cells cease division, whereas proliferation rate remains high in the boundary region, confirmed by our measurements. Cell size distribution in the centre of the colony resembles the observed distribution under the assumption of cell growth in response to tension, leading to a minimal state of compression in the centre of the colony and tension on the edges.

A study on migrating L1 fibroblast cells employs an agent based model of unconnected incompressible cells, that divide depending on the distance to the nearest neighbour [Bindschadler07]. The boundary advancement in division blocked as well as free-proliferative case is reproduced as in our model, though cell growth as well as mechanical coupling as an essential aspect of collective cell migration are not considered, which implies that cells are in a stress free state. A model of connected spheroids subject to a hard-core repulsive short distance attractive potential, with cell compression as the driving proliferation inhibitor report similar findings of proliferation inhibition in the centre of growing flat cell colonies [Drasdo07]. Measurements on growing cell colonies in the pre-contact inhibition regime have identified cells in a tensed state exerting inwards directed traction forces on the substrate [Trepat09, Tambe10]. This is in favour of our plastic growth model, that considers cell growth equilibrating tension, resulting in a minimal state of compression in cells in the contact inhibited regime of the bulk, and tension in the non-contact inhibited regime at the colony boundary.

Biophysical aspects of EMT

Presenting a contact inhibited tissue with free space results in a melting of the tissue, characterised by a reduced density (increased area covered by individuals) emerging from the boundary. By use of a dynamic cell cycle read-out, cells are partitioned into two different cell cycle stages and a difference in area distribution is observed. Cells in $S/G2/M$ phase are identified to occupy more space than cells than cells in $G0/G1$ and we identified a linear size increase of cells as they go along the cell cycle from $G1$ to M phase, with a characteristic area at cell cycle switch.

Assuming an S-phase entrance checkpoint for available space explains the two different distributions of cell areas for cells in $G0/G1$ versus cells in $S/G2/M$. Cells start in $G0/G1$ and grow until a critical threshold is reached, upon which they enter S-phase, thus a distribution with little numbers of cells above the threshold is observed. Contrary, cells in $S/G2/M$ recruit new cells from $G1$ phase only if those cells passed the threshold. Therefore, the resulting distribution gets shifted to higher values. This mechanism also explains measurements where cell cycle progression is chemically blocked. There the tissue melts and then stops expansion. After washout cells abruptly enter S-phase, also deep in the tissue, resulting in a fast acceleration of the boundary of the tissue. The dynamics of the boundary advancement is thereafter undistinguished from wild type dynamics, leading to the conclusion that cell division is essential for boundary advancement. Furthermore, the suggested S-phase size-checkpoint is in agreement with studies based on single cells, were a minimum area for cells to spread on was identified as critical for cell cycle progression [Chen97, Huang99].

In the long term, cells away from the leading edge begin to divide and reduce the space available to cells. As cells that once entered S phase can't switch back without division, the distribution gets shifted to narrower values. Our data also support the view of a size check-point in M phase, as cells passing fast through M-phase have an area distribution shifted to greater values than the those taking long through M-phase. As the cells on the boundary gradually obtain more space due to melting, they gradually take longer time to complete M-phase, whereas cells that

enter S-phase when the tissue is already molten significantly, require much less time to proceed until division.

From the cells point of view, such an S-phase entrance check-point related to size is reasonable, as during synthesis the cell material doubles and therefore, a cell requires more space. Thus it is an efficient strategy to probe the available area and enter S-phase if enough space is available. A similar argument would support an M-phase checkpoint as for a cell to divide, a minimal space available for the daughter cells should exist.

Such space checkpoints require mechanisms that allow the cell to translate space measurements to its molecular language. Commonly, the conversion of mechanical cues to signalling is referred to as mechanotransduction [Orr06]. One way to measure if there is enough space available, would be to probe stress on a cell. If there is compression, then for a cell it will be more difficult to gain space as compared to stress-free cells, or ones that are subject to tensile stress. Stress translation could be mediated via the cytoskeleton. Indeed an actin cytoskeleton dependant checkpoint in late $G1$ was previously identified [Huang02]. By depolimerisation of the actin cytoskeleton it was shown that cells become unable to advance to S phase. On the other hand, stress fibre formation induces clustering of integrins, which in turn enables sustained ERK signalling, necessary for cyclin D1 activation in mid $G1$ [Roovers03]. Also, integrin signalling in response to stress is reported [Katsumi05]. This supports the view, that the motile cells on the boundary induce stress in the neighbouring cells, which then leads to activation of growthfactor signalling pathways to finally result in cell cycle progression. A confirmation of this picture could be achieved by a joint measurement of cell size, ERK as well as integrin signalling activity. Such an experiment could also clarify the role of a previously observed travelling ERK wave, whether the wave passes cells before they increase their area or it is a consequence of the mechanical changes. Alternatively, stretching cells on an extendible membrane as used in [Trepat07] would provide a direct read-out of stress induced cell-cycle progression. There, one could measure the duration for cell cycle completion after S-phase entrance due to stretch and compare it to the duration measured for cells, which after S-phase entrance due to stretch become compressed.

We expect from out data, that the duration is then increased compared to the uncompressed case. Regulation of such an M-phase checkpoint could potentially be provided by the microtubule cytoskeleton, as drugs targeting microtubules result in prolonged M-phase duration [Jordan93, Sorger97], however, more experiments to clarify this are required.

The finding of a size checkpoint in S-phase and the proposed size checkpoint in M-phase, explain the observed size dependant growth rate. Together with our model this strongly suggests mechanical control of the cell cycle. The role of biochemical signalling cannot be neglected, but the picture of the mechanical aspects involved in growth control as well as collective migration becomes clearer. It suggests that cells grow in response to tension as proposed earlier [Huang99], divide as a function of area and exist in a state of minimal or no compression in the contact inhibited regime, supporting the view of mechanical regulation of proliferation as previously suggested in other contexts [Shraiman05, Hufnagel07].

Motion guided by dynamically maintained gradients

By quantitative measurements, we have identified, that the polarised migration of tissues induced by chemokine signalling is highly ordered and results in a tissue stretching. Loss of chemokine signalling leads to loss of order and reduced velocity of individuals accompanied by reduced tissue stretching. We concluded, that the tissue becomes polarised by chemokine signalling. A common method of cell polarisation is given by chemotaxis, where cells find themselves in a chemical concentration field and move in the direction of greater chemokine concentration. Previous experiments with the posterior lateral line primordium of zebrafish indicate that the chemical concentration field is homogeneous along a line, conflicting with the classical chemotaxis view. Graded transcription of the receptor CXCR4 for the chemokine SDF1 has been proposed as symmetry breaking mechanism, but lacks proof [Weijer09]. We provide an alternative interpretation of the data, that in contrast to common chemotaxis models, where the chemokine distribution is prefigured graded, shows that cell collectives with uniform receptor distribution can dynamically establish and maintain an asymmetric chemokine distribution in an isotropic production field

[Streichan11]. This is accomplished by storing the collectives velocity in the profile of the chemokine, rather than obtaining an internal polarisation due to receptor distribution. As the cells move, they actively modulate a diffusive ligand field that is uniformly produced along a line. Receptor induced ligand co-internalisation and degradation of ligand lead to a reduced ligand concentration in the vicinity of the tissue as compared to the surrounding environment. By moving, the cell collective shapes the ligand distribution asymmetrically, as the tissue becomes displaced to higher ligand concentrations at the front, whereas its rear moves away from high ligand concentrations. The mathematical treatment revealed a closed expression for the velocity of the tissue as a function of length, ligand spread as well as degradation and receptor uptake. An optimal length for the tissue, maximising velocity was identified.

Coupling chemotaxis to mechanics

We coupled the chemical based model to a mechanical description of moving cell collectives comprising attachment points coupled to elastic cells and identified that motion along dynamically maintained gradients induces an elongation of the lattice and result in an anisotropic stress distribution, where normal stress is highest in direction of migration.

By read-out of cell polarisation, we found that individual cells send protrusions in the direction of migration and towards the midline of the tissue. Experimental analysis showed that the motion of the tissue induces an anisotropic stress distribution, moving in the direction of greatest normal stress.Measurements with migration deficient primordia show that the anisotropy is indeed induced by the migration and not due to e.g. tissue topology or other mechanical properties. Interestingly, the stress distribution along the migration direction indicates reduced stress at the location of pro-neuromasts and increased stress in intermediate zones, which could be a consequence of increased coupling strength in those zones, as proposed in [Hava09].

Coupling growth to motility

On long time scales, migration in the pLLP is more complicated, as it deposits pro-

neuromasts en route. It is known that the tissue compensates for the deposition induced cell number reduction by proliferation. We thus extended our model to incorporate growth. This results in an increasing tissue length, eventually leading to a slow down of the tissue. We propose that the tissue compensates this slow down, by deposition of discrete subunits and show that, under these assumptions, the system is able to reproduce the observed discrete cell depositions. Furthermore, our analysis revealed a connection between the division rate of the cells, the tissue length and organ formation. The time until the next deposition occurs is predicted to be inversely proportional to the division rate, thus reductions in proliferation rate should result in an increased time between subsequent organ deposition events and, assuming the velocity to remain at similar levels, an increased distance travelled until the next organ deposition. Recent measurements support this view, as they show that a decreased proliferation rate as well as increased rate of apoptosis - programmed cell death - result in fewer neuromasts with increased spacing [Aman11], in agreement with another proliferation control study, which states pLLP migration with a reduced number of deposited organs upon inhibition of proliferation [Villablanca06].

Our model is in agreement with previous studies showing that receptor and ligand are a necessary requirement for migration [David02, Haas06]. This is also in agreement with our experimental analysis, as the high order in the moving tissue is lost in case of impaired chemokine signalling accompanied by migration arrest. The initial symmetry breaking required to initiate of the motion of the tissue could be provided by ligand independent motion, as the pLLP is observed to initially migrate for short distances away from its birthplace even in absence of SDF1 activity [Dambly-Chaudiere07].

Studies on the slime mould *Dictyostelium discoideum* showed that single cells of this species are able to remodel extracellular distributions of their chemoattractant cAMP by secreting a phosphodiesterase [Garcia09, Gregor10]. This results in a degradation of cAMP and thus promotes local gradient formation. Our mechanism enables directed migration over much larger scales than that of a single cell, simply by binding ligand to receptor and subsequent internalisation of both. As this is a common mechanism, our model provides a general mechanism independent of the

special genetic pathway used, that could be employed in other situations, where directed migration occurs.

Further experiments should be conducted to challenge the model. One way is provided by alteration of the tissues velocity, which should vary the spacing between organs, leading to closer organ deposition for slower tissues and greater separation between organs for faster tissues. Yet another way to test the model is to probe the ligand distribution or receptor dynamics, as the model makes predictions on the form of the ligand distribution and receptor-ligand interaction.

Here, we focused on the principle of encoding directionality in a dynamically maintained gradient and its implications on tissue mechanics. In future studies, one could extend the model to incorporate additional regulatory steps, such as graded receptor distributions or additional receptors acting as scavengers by removing additional extracellular ligand, optimally based on measurements. Another route is given by incorporation of stochastic fluctuations in the motion of the cells, to account for noisiness in the system.

Taken together, migration along dynamically maintained gradients provides a novel model for the polarisation of a cell collective in the setting of a uniform ligand distribution, that becomes actively modulated by a tissue moving along a travelling wave, which induces an anisotropic stress distribution in the tissue and can account for organ formation.

Image Analysis

Inspired by the biophysical description of epithelia, we developed a biophysical image model. Although high memory usage and long execution times for the algorithm are undesirable, a good initial guess can speed up the process, which also helps prevent formation of artefacts. The advantages of this model clearly are the physical interpretation of the objects in the image and an improvement of the segmentation result where other methods fail.

Outlook

Our approach to the study of the interplay between growth and migration involved

two sample epithelia. A two dimensional cultured monolayer and a tissue migrating through a Zebrafish embryo. One prominent similarity of these two systems is a reduction in epithelial character at the tissue's edge, described as partial epithelial to mesenchymal transition at the leading edge. The strategy of tissues to move whilst remaining in contact seems to be a commonly used mechanism to generate complex organs. One goal of developmental biology is to understand how this is controlled during embryogenesis. However, the highly complex character of tissues in an embryo, such as differentiation of specialised cell types within, increases the number of variables in this process.

In vitro studies, with cultured epithelial cells of essentially identical character provide a controlled framework, that significantly reduces the level of complexity. The conditions of the experiments are well defined and can be controlled, ideally suited to address specific mechanistic questions. Controle of growth in an embryonic tissue, such as the posterior lateral line primordium discussed here, can be mediated by a number of mechanisms, thus complicating the interpretation of the observed patterns. However, genetic studies on embryos have revealed a great deal about the nature and regulation of signalling systems that mediate cell-cell communication, a topic where cell culture is weaker, thus information from these systems may be integrated. Here, we have studied the role of mechanical regulation of morphological character of cells within epithelia. We have shown that biophysical mechanisms can account for the observed patterns. Combined knowledge of the behaviour of embryonic tissues in vivo with the methods used to interpret the in vitro observations, lead to the proposal of new experiments and allowed an interpretation of the emergent results.

Thus comparative studies of tissues in embryos and cell culture will help to increase our understanding of the formation of organs and the embryo. In future studies, one might envision a routine approach to organogenesis, where cells of the embryonic tissue are studied in cell culture, allowing an even closer analogy and highly specific hypotheses testing. Such a comparison between two systems requires a combined approach of sophisticated data analysis and methods from physics and mathematics, leading the way towards a quantitative understanding of biology.

Appendix A

Variation of lattice model energy

Here we want to derive the equations of motion for the vertices $\mathbf{q}(t)$ in the lattice model using gradient descent. The energy governing the vertex dynamics is given by

$$E(\mathbf{q}(t), \mathbf{R}) = \frac{k}{2}\Big(L^T\mathbf{q} - \mathbf{l}\Big)^T\Big(L^T\mathbf{q} - \mathbf{l}\Big) + \frac{\kappa}{2}\Big(\mathbf{R} - \frac{1}{2}C\mathbf{q}\Big)^T\Big(\mathbf{R} - \frac{1}{2}C\mathbf{q}\Big). \quad \text{(A.1)}$$

In order to derive the variation of the energy functional governing the vertices dynamics, we consider a curve $\mathbf{q} : I \to \mathbb{R}^{N+1}$, with $t \mapsto \mathbf{q}(t)$ as variation of $\tilde{\mathbf{q}}$, such that $\mathbf{q}(0) = \tilde{\mathbf{q}}$ and furthermore consider the attachment points R as fixed. We treat variation of the terms separately

The first term:

$$\begin{aligned}
\frac{d}{dt}\Big(\big(L^T\mathbf{q}(t) - \mathbf{l}\big)^T\big(L^T\mathbf{q}(t) - \mathbf{l}\big)\Big) &= \frac{d}{dt}\Big(\mathbf{q}(t)^T LL^T\mathbf{q}(t) - \mathbf{q}(t)^T L\mathbf{l} - \mathbf{l}^T L^T\mathbf{q}(t) + \mathbf{l}^T\mathbf{l}\Big) \\
&= \dot{\mathbf{q}}^T LL^T\mathbf{q} + \mathbf{q}^T LL^T\mathbf{q} - \dot{\mathbf{q}}^T L\mathbf{l} - \mathbf{l}^T L^T\dot{\mathbf{q}} \\
&= \Big(\big(LL^T\mathbf{q}\big)^T\dot{\mathbf{q}}\Big)^T + \big(LL^T\mathbf{q}\big)^T\dot{\mathbf{q}} - 2(L\mathbf{l})^T\dot{\mathbf{q}} \\
&= 2\Big(LL^T\mathbf{q} - L\mathbf{l}\Big)^T\dot{\mathbf{q}},
\end{aligned}$$

where in the third step, we made use of $c^T = c$ for scalar c. The second term gives

$$\begin{aligned}\frac{d}{dt}\left(\mathbf{R} - \frac{1}{2}C\mathbf{q}(t)\right)^T\left(\mathbf{R} - \frac{1}{2}C\mathbf{q}(t)\right) &= \frac{d}{dt}\left(\mathbf{R}^T\mathbf{R} - \frac{1}{2}(C\mathbf{q})^T\mathbf{R} - \frac{1}{2}\mathbf{R}^TC\mathbf{q} + \frac{1}{4}(C\mathbf{q})^T(C\mathbf{q})\right)\\ &= \frac{1}{4}(C\dot{\mathbf{q}})^T(C\mathbf{q}) + \frac{1}{4}(C\dot{\mathbf{q}})^T(C\dot{\mathbf{q}}) - (C^T\mathbf{R})^T\dot{\mathbf{q}}\\ &= \frac{1}{2}(C^TC\mathbf{q})^T\dot{\mathbf{q}} - 2(C^T\mathbf{R})^T\dot{\mathbf{q}}\\ &= \left(\frac{1}{2}C^TC\mathbf{q} - C^T\mathbf{R}\right)^T\dot{\mathbf{q}}.\end{aligned}$$

Putting the pieces together, we obtain the gradient of the energy functional as

$$\begin{aligned}grad(E(\mathbf{q}(t), \mathbf{R})) &= k\left(LL^T\mathbf{q} - L\mathbf{l}\right) + \kappa\left(\frac{1}{4}C^TC\mathbf{q} - \frac{1}{2}C^T\mathbf{R}\right)\\ &= \left(kLL^T + \frac{\kappa}{4}C^TC\right)\mathbf{q} - kL\mathbf{l} - \frac{\kappa}{2}C^T\mathbf{R},\end{aligned}$$

leading to the definition of $M = k(LL^T\frac{\kappa}{4}C^TC)$. Expressions for the matrices used above are

$$M = \begin{pmatrix} k+\frac{\kappa}{4} & \frac{\kappa}{4}-k & 0 & \cdots & \cdots & \cdots & 0\\ \frac{\kappa}{4}-k & 2k+\frac{\kappa}{2} & \frac{\kappa}{4}-k & 0 & \cdots & \cdots & \vdots\\ 0 & \frac{\kappa}{4}-k & 2k+\frac{\kappa}{2} & \frac{\kappa}{4}-k & 0 & \cdots & \vdots\\ \vdots & \ddots & \ddots & \ddots & \ddots & \ddots & \vdots\\ 0 & \cdots & \cdots & \cdots & \cdots & \frac{\kappa}{4}-k & k+\frac{\kappa}{4}\end{pmatrix}$$

$$C = \begin{pmatrix} 1 & 1 & 0 & 0 & \cdots & 0\\ 0 & 1 & 1 & 0 & \cdots & \vdots\\ \vdots & \ddots & \ddots & \ddots & \ddots & \vdots\\ 0 & \cdots & \cdots & \cdots & 1 & 1\end{pmatrix}, \qquad L = \begin{pmatrix} -1 & 0 & 0 & \cdots & \cdots & 0\\ 1 & -1 & 0 & \cdots & \cdots & \vdots\\ 0 & 1 & -1 & 0 & \cdots & \vdots\\ \vdots & \ddots & \ddots & \ddots & \ddots & \vdots\\ 0 & \cdots & \cdots & \cdots & 1 & -1\\ 0 & \cdots & \cdots & \cdots & 0 & 1\end{pmatrix}.$$

Appendix B

Dynamically maintained gradients appendix

The constants in eq. (3.6) are derived as described in the text and they read as follows:

$$B^{(1)} = \left(\frac{\tilde{\gamma}}{\lambda_D^2} - \frac{1}{1+\tilde{\rho}}\left(\frac{\tilde{\gamma}}{\lambda_D^2} - A^{(2)}\lambda_+^{(2)}e^{-\lambda_-^{(2)}L} - B^{(2)}\lambda_-^{(2)}e^{-\lambda_+^{(2)}L}\right)\right)\frac{e^{\lambda_+^{(1)}L}}{\lambda_-^{(1)}}$$

$$A^{(3)} = \left(\frac{\tilde{\gamma}}{\lambda_D^2} - \frac{1}{1+\tilde{\rho}}\left(\frac{\tilde{\gamma}}{\lambda_D^2} - A^{(2)}\lambda_+^{(2)}e^{\lambda_-^{(2)}L} - B^{(2)}\lambda_-^{(2)}e^{\lambda_+^{(2)}L}\right)\right)\frac{e^{-\lambda_-^{(1)}L}}{\lambda_+^{(1)}}$$

$$A^{(2)} = \frac{\tilde{\gamma}}{\lambda_D^2}\left(-e^{L\lambda_-^{(2)}}\left(\lambda_D^2 + \frac{\lambda_D^2}{1+\tilde{\rho}}\right) * \left(\lambda_D^2\left(\lambda_-^{(1)} - \lambda_+^{(1)}e^{2L\lambda_+^{(2)}}\right) - \frac{\lambda_D^2}{1+\tilde{\rho}}\left(\lambda_-^{(2)} - \lambda_-^{(2)}e^{2L\lambda_+^{(2)}}\right)\right)\right) / \left(\left(\lambda_D^2 + \frac{\lambda_D^2}{1+\tilde{\rho}}\right)\left(e^{2L\lambda_-^{(2)}} - e^{2L\lambda_+^{(2)}}\right) + \lambda_D^2\frac{\lambda_D^2}{1+\tilde{\rho}}\left(e^{2L\lambda_-^{(2)}}\left(\lambda_-^{(2)}\lambda_+^{(1)} + \lambda_-^{(1)}\lambda_+^{(2)}\right) - e^{2L\lambda_+^{(2)}}\left(\lambda_-^{(2)}\lambda_-^{(1)} + \lambda_+^{(1)}\lambda_+^{(2)}\right)\right)\right)$$

$$B^{(2)} = \frac{\tilde{\gamma}}{\lambda_D^2}\left(e^{L\lambda_+^{(2)}}\left(\lambda_D^2 + \frac{\lambda_D^2}{1+\tilde{\rho}}\right) * \left(\lambda_D^2\left(\lambda_-^{(1)} - \lambda_+^{(1)}e^{2L\lambda_-^{(2)}}\right) - \frac{\lambda_D^2}{1+\tilde{\rho}}\left(\lambda_+^{(2)} - \lambda_+^{(2)}e^{2L\lambda_-^{(2)}}\right)\right)\right) / \left(\left(\lambda_D^2 + \frac{\lambda_D^2}{1+\tilde{\rho}}\right)\left(e^{2L\lambda_-^{(2)}} - e^{2L\lambda_+^{(2)}}\right) + \lambda_D^2\frac{\lambda_D^2}{1+\tilde{\rho}}\left(e^{2L\lambda_-^{(2)}}\left(\lambda_-^{(2)}\lambda_+^{(1)} + \lambda_-^{(1)}\lambda_+^{(2)}\right) - e^{2L\lambda_+^{(2)}}\left(\lambda_-^{(2)}\lambda_-^{(1)} + \lambda_+^{(1)}\lambda_+^{(2)}\right)\right)\right).$$

The critical length for deposition from the linearisation of eq. 3.9 reads as

$$L_{dep} = \frac{\frac{\lambda_-^{(1)}-\lambda_+^{(1)}}{\left(1+\tilde{\rho}\right)^2}\left(\lambda_D^2\lambda_-^{(2)}\lambda_+^{(2)}(\lambda_+^{(2)} - \lambda_-^{(2)})a\vartheta + \tilde{\gamma}\frac{\tilde{\rho}^2+2\tilde{\rho}}{1+\tilde{\rho}}\left(\lambda_-^{(2)}(1-e^{a\lambda_+^{(2)}}) - \lambda_+^{(2)}(1-e^{a\lambda_-^{(2)}})\right)\right)}{2\tilde{\gamma}\lambda_+^{(1)}\frac{\tilde{\rho}}{1+\tilde{\rho}}\left(\lambda_-^{(1)}\left(\lambda_-^{(2)}(1-e^{a\lambda_+^{(2)}}) - \lambda_+^{(2)}(1-e^{a\lambda_-^{(2)}})\right) + \frac{\lambda_-^{(2)}\lambda_+^{(2)}}{1+\tilde{\rho}}(e^{a\lambda_+^{(2)}} - e^{a\lambda_-^{(2)}})\right)}.$$

Appendix C

Level Sets

In this section, we will give the definition of an implicit formulation of curves and surfaces, as can be found in [Osher03, Sethian08, Mitiche10]. For simplicity, let $\gamma : I \to \mathbb{R}^2$ denote a closed curve, that maps $s \mapsto \gamma(s)$ via the parametrisation s. Generalisation to surfaces is straight forward. Implicit representation of such curves in form of level sets provides not only a parameter free definition of the curve, but also a well defined notion of domains enclosed by the curve and exterior to the curve without additional expensive calculations. Let $\phi : \mathbb{R}^2 \to \mathbb{R}$, with $\mathbf{x} \mapsto \phi(\mathbf{x})$, such that

$$\gamma := \{\mathbf{x} \in \mathbb{R}^2 \mid \phi(\mathbf{x}) = 0\} \tag{C.1}$$

$$\gamma_{in} := \{\mathbf{x} \in \mathbb{R}^2 \mid \phi(\mathbf{x}) < 0\} \tag{C.2}$$

$$\gamma_{ext} := \{\mathbf{x} \in \mathbb{R}^2 \mid \phi(\mathbf{x}) > 0\}, \tag{C.3}$$

then ϕ is called a level sets function representing the curve γ. By this definition the interior of the curve γ_{in} as well as the exterior γ_{ext} are already obtained by ϕ, a valuable property, that saves computation time. An example of a level sets function representing a curve is provided by the signed distance function, which assigns a sign to the distance from each point to the curve depending on its membership with respect to γ_{in} and γ_{ext}.

Lets now consider a curve that evolves in the direction of its normal at each point with velocity v_n, with the definition of a variation of the curve evolving γ as $\tilde{\gamma} : I \times [-\epsilon, \epsilon] \to \mathbb{R}^2$, where $(s,t) \mapsto\to \tilde{\gamma}(s,t)$ with $\tilde{\gamma}(s,0) = \gamma(s)$ for all s [Baum09]. Then the variation of the level sets function $\tilde{\phi} : \mathbb{R}^2 \times [-\epsilon, \epsilon] \to \mathbb{R}$ is defined by the variation of the curve $\tilde{\gamma}$ as

$\tilde{\phi}\big(\tilde{\gamma}(s,t),t\big) = 0$ such that $\tilde{\phi}\big(\tilde{\gamma}(s,0),0\big) = \phi(\gamma(s)) = 0$. By using the fact that the level sets function always vanishes on the contour and that it is independent of the parametrisation, one obtains the evolution equation of the level sets function. By taking the total derivative of the curve, we get

$$\frac{d\tilde{\phi}}{dt} = \frac{\partial\tilde{\phi}}{\tilde{\partial}t} + \nabla\tilde{\phi}\frac{\partial\tilde{\gamma}}{\partial t} = 0.$$

On the other hand as the level sets function is independent of the parametrisation, we have

$$\frac{\partial\tilde{\phi}}{\partial s} = \nabla\tilde{\phi}\frac{\partial\tilde{\gamma}}{\partial s} = 0.$$

As $\frac{\partial\tilde{\gamma}}{\partial s} = \mathbf{t}$ is a tangent vector on the curve $\tilde{\gamma}$, we have the result that $\nabla\tilde{\phi} = \|\nabla\tilde{\phi}\|\mathbf{n}$, where $\mathbf{n}$ is a normal vector of the curve. As the curve evolves in the direction of the normal with velocity v_n, we also have $\frac{\partial\tilde{\gamma}}{\partial t} = v_n\mathbf{n}$ and we can combine that $\nabla\tilde{\phi}\frac{\partial\tilde{\gamma}}{\partial t} = \|\nabla\tilde{\phi}\|\mathbf{n}\mathbf{n}v_n$ and thus we have:

$$\frac{1}{\|\nabla\tilde{\phi}\|}\frac{\partial\tilde{\phi}}{\partial t} = -v_n. \tag{C.4}$$

Appendix D

Gradient descent

To obtain the evolution equation of contours, a gradient descent scheme is used, which we will explain here. We will follow the key arguments given in [Solem05], where a nice geometric introduction to gradient descent with moving surfaces is given. In the first part, the notion of tangential space of moving surfaces will be established and in the second part the general formulation of the gradient descent given.

Tangent space of evolving surfaces

Let

$$\begin{aligned} \phi : \mathbb{R}^{n+1} \times I &\to \mathbb{R} \\ (\mathbf{x}, t) &\mapsto \phi(\mathbf{x}, t) \end{aligned}$$

define a level sets function evolving with time. In particular the evolution of ϕ obeys the level sets equation (C.4)

$$\frac{1}{\|\nabla\phi\|}\frac{\partial\phi(\mathbf{x},t)}{\partial t} = -v_n. \tag{D.1}$$

The initial position of the surface is defined by $\gamma_o := \{\mathbf{x} \in \mathbb{R}^{n+1} \mid \phi(\mathbf{x}, 0) = 0\}$ and the **evolution of the surface** is defined as $\gamma(t) := \{\mathbf{x} \in \mathbb{R}^{n+1} \mid \phi(\mathbf{x}, t) = 0\}$. Then by the evolution of the surface, there is an equivalence relation $\sim$ between the surfaces at various times, as this relation is transitive, reflexive and symmetric. Let $M := \{\gamma \mid \gamma \sim \gamma_0\}$ denote

the manifold of all possible evolutions from γ_0. A tangential vector on a manifold M at a point γ_0 is defined as the derivative of a curve passing through γ_0. Let $\gamma_0 \in M$ be a point in M and $\gamma(t)$ an evolution of γ_0, defined as the zero level set of ϕ, i.e. $\gamma(t) = \{\mathbf{x} \mid \phi(\mathbf{x}, t) = 0\}$. As ϕ obeys the level sets equation, the following defines the normal velocity of evolution of γ_0

$$\dot{\gamma}(t) = -\frac{1}{\|\nabla\phi\|}\frac{\partial\phi(\mathbf{x},t)}{\partial t}. \tag{D.2}$$

As $\gamma(t)$ is a curve through M, $\dot{\gamma}(0)$ gives a tangent vector of M at γ_0 and the set of all tangent vectors defines the tangent space $T_{\gamma_0}M$ at γ_0.

Example

Consider an element $\gamma_0 \in M$, defined by the level sets function $\phi_0(\mathbf{x})$. Then choose another level set $\psi : \mathbb{R}^{n+1} \to \mathbb{R}$ and define $\phi(\mathbf{x}, t) := \phi_0(\mathbf{x}) + t\psi(\mathbf{x})$ such that $\gamma(t) := \{\mathbf{x} \mid \phi(\mathbf{x}, t) = 0\}$ is an evolution of γ_0. Then according to eq. D.2, the tangent vector at γ_0 is given by $\dot{\gamma}(0) = -\frac{1}{\|\nabla\phi\|}\frac{\partial\phi(\mathbf{x},t)}{\partial t}\,|_{t=0} = -\frac{\psi(\mathbf{x})}{\|\nabla\phi_0(\mathbf{x})}$.

Gradient descent

Let M denote a manifold and $\gamma(t)$ a curve through the point $p \in M$, such that $v = \dot{\gamma}(0) \in T_pM$. Furthermore let $E : M \to \mathbb{R}$ be a differentiable functional. Then the **differential** of E is defined as [O'Neill83, AmannEscher01]:

$$dE(p) : T_pM \to \mathbb{R} \tag{D.3}$$

$$v \to dE(p)v := \frac{d}{dt}E(\gamma(t))\,|_{t=0}\,. \tag{D.4}$$

With the bilinear form $\langle\cdot,\cdot\rangle : T_{\gamma(t)}M \times T_{\gamma(t)}M \to \mathbb{R}$, the gradient of the function E is defined as the vector $gradE(\gamma)$ which obeys $\langle gradE(\gamma), v\rangle = dE(\gamma)v$ for all $v \in T_{\gamma(t)}M$.

According to [Solem05], the **gradient descent** of the functional $E : M \to \mathbb{R}$ is defined as a curve $\gamma(t)$ that obeys

$$\dot{\gamma}(t) = -gradE(\gamma(t)). \tag{D.5}$$

As the tangent vector $\dot{\gamma}(t) \in T_{\gamma(t)}M$, we have

$$\frac{d}{dt}E(\gamma(t)) = dE(\gamma(t))\dot{\gamma}(t) = -dE(\gamma(t))gradE(\gamma(t)) = -\langle gradE(\gamma(t)), gradE(\gamma(t))\rangle \leq 0$$

and hence the definition produces a descent.

Example

Let $M = \mathbb{R}^3$ and $q : [0,1] \to M$, $s \mapsto q(s) \in M$ denote curve in M with tangent vector $q'(s) \in T_{q(s)}M$ subject to

$$E = \int \mathcal{L}(q(s), q'(s), s)ds. \tag{D.6}$$

With the variation $h : [0,1] \times (-\epsilon, \epsilon) \to M$ that maps $(s,t) \mapsto h(s,t)$ and coincides with $q(s)$ for $t = 0$ [Baum09], one obtains the variation of E

$$\frac{d}{dt}E(h(s,t)) = \int \left\{ \frac{\partial \mathcal{L}}{\partial q} - \frac{\partial}{\partial s}\left(\frac{\partial \mathcal{L}}{\partial \dot{q}}\right) \right\} \frac{\partial h}{\partial t} ds.$$

The gradient descent scheme then gives the following result

$$\dot{q}(t) = -\frac{\partial \mathcal{L}}{\partial q} + \frac{\partial}{\partial s}\left(\frac{\partial \mathcal{L}}{\partial \dot{q}}\right). \tag{D.7}$$

At the extremal position, one obtains the Euler-Lagrange equations that determine the trajectory of a particle q subject to the Lagrangian $\mathcal{L}$ [Scheck99].

Appendix E

Material and methods

Imaging and culturing methods

Time lapse imaging was performed on commercially available spinning disc microscopes with $10X/NA0.3$, $20X/0.7NA$, $40X/1.2NA$ or $63X/1.2NA$ objectives respectively. Illumination of phase images used a halogen lamp, fluorescence images were obtained using 488 nm, 562 nm and 405 nm laserlines.

Zebrafish where maintained at $28°C$ on a $14h/10h$ day and night cycle. Natural spawning provides embryos, which are kept in an incubator at $28°C$. Embryos used for imaging where around the stage of 32 hours post fertilisation. The embryos where anesthesied in 0.01% Tricane for imaging. For mounting, embryos where positioned on their sides in glass-bottom petri dishes and covered with 1% low point melting agarose in $E3$. Z-Stacks of pLLP where taken with 1 μm intervals, sampling through the tissue. Laser ablation experiments where performed with a pulsed UV laser attached to a confocal microscope. Time lapse of single planes is recorded and in parallel junctions are cut.

MDCK II (ATCC Number: CRL-2936) kidney cells from cocker spaniel where cultured in MEM with 1000 mg/l glucose, 5% FBS and 2mM glutamine, at 37°C and 5% CO_2, in 75 cm^2 flasks. For imaging of culture cells, phenol red free IMEM supplied with Penicillin-Streptomycin and 5% FBS was used. The medium was replaced every second day and the culture conditions were kept at 37°C and 5% CO_2. For the colony growth experiments, seeding cells was done at uniform density of approximately 600 cells $/mm^2$ on fibronectin coated PDMS membrane. Single colony experiments were performed by seeding cells at

a density of about 1 cell/cm^2 in a glass bottom petri dish. Growing MDCK-colonies where recorded on 9×9 field of view, with images taken every 10 minutes in phase and three hours in fluorescence. FUCCI-MDCK-cells were grown on a glass bottom petri dish containing an 8 mm teflon block, until the cells entered a state of contact inhibition of proliferation. Imaging started upon removal of the teflon block. A concentration of 20 μM of MEK-inhibitor U0126 (Promega) was added to the cells one our prior block removal and imaging. After 28 hours the MEK-inhibitor was removed by washing the cells with medium. Pictures of boundary release experiments where taken in a regular interval of 30 minutes, with ten per cent overlap of 30×9 images arranged in a grid as discussed.

Image Processing

Images where analysed based on several custom written MATLAB codes. Colony profiles where obtained by use of edge detection methods from the MATLAB image processing toolbox. Nuclei (both cell culture and zebrafish embryo) are analysed by use of sequential algorithm. If a Z-stack is taken, images are deconvolved, by use of an approximation of the microscopes point spread function [Grill99] and a maximum likelihood algorithm [Richardson72]. Then a procedure for both single plane and Z-stack images was employed. Background correction, object detection and refinement of object detection was performed. Local background was estimated by a top hat transformation and subtracted from the image. Then images are filtered with a mexican hat function of width corresponding to radius of nuclei using built in matlab function imfilter. Together with a histogram based threshold estimation, a mask for nuclei position is obtained [Otsu79]. This is fed to an implementation of the chan-vese energy in the level sets framework based on a sparse field method [Lankton09]. If objects greater than three standard deviations away from the median are identified, the mask is supplied as initial guess of contour of multi level sets based algorithm developed in 4. In case of the pLLP the membrane signal was detected using standard edge detection methods and used to restrict the segmented nuclei to the ones which are in the pLLP.

From positions of centroids, cell density and structure functions are obtained. A voronoi tesselation is constructed, used to obtain a proxy for the area covered by an individual cell. For velocity approximation, two methods are used: Nearest neighbour tracking of segmented objects is used to re-construct tracks and from this the velocity of a cell approximated. Poorly segmented nuclei, can result in short tracks, which are either fused by

allowing gaps of three consecutive images, or excluded from the analysis. Alternatively PIV analysis based on membrane or contrast images gives a mean displacement field [Raffel98]. The velocity of the boundary is obtained by averaging the velocity of individual cells on the boundary. In case of the FUCCI MDCK marker, if a nucleus appears in both channels, as they do during the transition from $G1$ to S, it is assigned to the $S/G2/M$ group. The first time of switch from red to green state in the tracks marks the point of transition to S phase. Duration from $S/G2/M$ is the amount of time steps a nucleus appears in green state.

To analyse the direction of the lamellipodia extending from individual cells, a computerised segmentation of actin bursts, based on the transient nature of bursts is constructed. In order to get rid of the moving but otherwise stationary signal from the membranes, images of the subsequent time point are shifted such that the correlation between the two time points is maximised. This corrects for the motion of the tissue and allows for a direct comparison of the actin signal at different times and at the same position within the tissue. Taking the difference between the shift corrected image and its predecessor, a simple threshold allows to segment parts of the image, where the signal has increased above the given threshold, resulting in an accurate identification of bursts.

Kymograph images where done with ImageJ 1.38 X, using the kymograph plug-in. Maximum intensity projection images where constructed by use of the Z-projection plug-in. Lines where chosen to be at the midline of the tissue. Stitching of images was performed using the stitching plug-in available in FIJI. Figures where made using Adobe InDesign CS.

Simulations

Simulations of vertex based lattice model for biophysical description of dynamic tissues are performed to obtain the configuration of vertices. Vertices are updated by matrix inversion for vertex position in the one dimensional case. Conjugate gradients algorithm is used to find the vertex configurations that minimise the energy in case of two dimensional lattices [Press07]. Attachment points dynamics is approximated by use of the explicit Euler algorithm over a small time step $\delta t << \nu$ [Gardiner09]. The probability of a cell to divide during an interval δt is $\delta t \gamma p(\Delta q_i)$. Simulations of ligand profiles are obtained by Runge-Kutta integration over a small time step δt. Numerical root of velocity is obtained by use of trust region dogleg method, implement in Matlab [More80].

List of Figures

Bibliography

[Abercrombie67] Abercrombie M *Contact inhibition: the phenomenon and its biological implications.* Natl Cancer Inst Monogr, 26 (1967), pp. 249-277

[Abercrombie70] Abercrombie M *Contact inhibition in tissue culture.* In Vitro, 6 (1970), pp. 128-142

[Aigouy10] Aigouy B, Farhadifar R, Staple D, Sagner A, Röper J, Jülicher F, Eaton S *Cell flow reorients the axis of planar polarity in the wing epithelium of drosophila* Cell, 142 (2010), pp. 773-786

[Alberts08] Alberts B, Johnson A, Lewis J, Raff M, Roberts K, Walter P *Molecular biology of the cell* Garland Science, 5 (2008)

[Altan04] Altan Z M, Fenteany G *c-Jun N-terminal kinase regulates lamellipodial protrusion and cell sheet migration during epithelial wound closure by a gene expression-independent mechanism* Biochem. Biophys. Res. Commun., 322 (2004), pp. 56-67

[Aman08] Aman A, Piotrowski T *Wnt/beta-catenin and Fgf signaling control collective cell migration by restricting chemokine receptor expression* Dev Cell, 15(5) (2008), pp. 749-761

[Aman10] Aman A, Piotrowski T *Cell migration during morphogenesis* Dev Biol, 341 (2010), pp. 20-33

[Aman11] Aman A, Nguyen M, Piotrowski T *Wnt/-catenin dependent cell proliferation underlies segmented lateral line morphogenesis* Dev Biol, 349(2) (2011), pp. 470-482

[AmannEscher01] Amann H, Escher J *Analysis III* Birkhuser Verlag, (2001)

[Angelini11] Angelini T E, Hannezo E, Trepat X, Marquez M, Fredberg J J, Weitz D A *Glass-like dynamics of collective cell migration* PNAS, 108(12) (2011), pp. 4714-4719

[Baum08] Baum B, Settleman J, Quinlan M P *Transitions between epithelial and mesenchymal states in development and disease* Semin. Cell Dev. Biol., 19(3) (2008), pp. 294-308

[Baum09] Baum H, *Eichfeldtheorie* Springer, (2009)

[Benoit09] Benoit Y D, Lussier C, Ducharme P A, Sivret S, Schnapp L M, Basora N, Beaulieu, J F *Integrin $\alpha 8\beta 1$ regulates adhesion, migration and proliferation of human intestinal crypt cells via a predominant RhoA/ROCK-dependent mechanism* Biol. Cell, 101 (2009), pp. 695-708

[Biname09] Binamé F, Pawlak G, Roux P, Hibner U *What makes cells move: requirements and obstacles for spontaneous cell motility* Mol. BioSyst., 6 (2010), pp. 648-661

[Bindschadler07] Bindschadler M, McGrath J L *Sheet migration by wounded monolayers as an emergent property of single-cell dynamics* J Cell Sci, 120 (2007), pp. 876-884

[Blaser05] Blaser H, Eisenbeiss S, Neumann M, Reichman-Fried M, Thisse B, Thisse C, Raz E *Transition from non-motile behaviour to directed migration during early PGC development in zebrafish* J. Cell Sci., 118(17) (2005), pp. 4027-4038

[Cakan09] Cakan Akdogan, G *FGF signaling couples morphogenesis to collective cell migration in the zebrafish posterior lateral line primordium* Ruperto-Carola Unversity Heidelberg, (2009), PhD Thesis

[Caselles97] Caselles V, Kimmel R, Sapiro G *Geodesic active contours* International Journal of Computer Vision, 22(1) (1997), pp. 61-79

[Castor68] Castor LN *Contact regulation of cell division in an epithelial-like cell line* J Cell Physiol, 72 (1968), pp. 161-72

[Chalfie94] Chalfie M, Tu Y, Euskirchen G, Ward W W, Prasher D C *Green fluorescent protein as a marker for gene expression* Science, 263(5148) (1994), pp. 802-805

[Chan01] Chan T F, Vese L A *Active contours without edges* IEEE Transactions on image processing, 10(2) (2001), pp. 266-277

[Chang96] Chang Y C, Hou T Y, Merrimen B, Osher S *A level set formulation of eulerian interface capturing methods for incompressible fluid flows* J Comp Phys, 124 (1996), pp. 449-464

[Chen97] Chen C S, Mrkisch M, Huang S, Whitesides G M, Ingber D E *Geometric control of cell life and death* Science, 276 (1997), pp. 1425-1428

[Cremers07] Cremers D, Rousson M, Derice R *A review of statistical approaches to level set segmentation: Integrating color, textrure, motion and shape* International Journal of Computer Vision, 72(2) (2007), pp. 195-215

[Dambly-Chaudiere07] C. Dambly-Chaudiére, N. Cubedo, A. Ghysen, *Control of cell migration in the development of the posterior lateral line: antagonistic interactions between the chemokine receptors CXCR4 and CXCR7/RDC1.* BMC Dev Biol., 29 (2007), pp. 7-23

[David02] David N, et. al. *Molecular basis of cell migration in the fish lateral line: Role of the chemokine receptor CXCR4 and of its ligand SDF1* PNAS, 99(25) (2002), pp. 16297-16302

[Dormann03] Dormann D, Weijer C J *Chemotactic cell movement during development* Curr. Opin. Genet. Dev., 13(4) (2003), pp. 358-364

[Drasdo07] Drasdo D, Hoehme S, Block M *On the role of physics in the growth and pattern formation of multi-cellular systems: What can we learn from individual-cell based models?* J Stat Phys, 128(1/2) (2007), pp. 287-345

[Farooqui04] Farooqui R, Fenteany G *Multiple rows of cells behind an epithelial wound edge extend cryptic lamellipodia to collectively drive cell sheet movement* J. Cell Sci, 118 (2004), pp. 51-63

[Farge11] Farge E *Mechanotransduction in development* Curr Top Dev Biol, 95 (2011), pp. 243-265

[Farhadifar07] Farhadifar R, Röper J, Aigouy B, Eaton S, Jülicher F *The influence of cell mechanics, cell-cell interactions, and proliferation on epithelial packing* Current Biology, 17(24) (2007), pp. 2095-2104

[Fenteany00] Fenteany G, Janmey P A, Stossel T P *Signaling pathways and cell mechanics involved in wound closure by epithelial cell sheets* Curr. Biol., 10 (2000), pp. 831-838

[Fletcher10] Fletcher D A, Mullins R D *Cell mechanics and the cyotskeleton* Nature, 463(28) (2010), pp. 485-492

[Folkman78] Folkman J, Moscona A *Role of cell shape in growth control* Nature, 273 (1978), pp. 345-349

[Friedl03] Friedl P, Wolf K *Tumor-cell invasion and migration: Diversity and escape mechanisms* Nature reviews Cancer, 3 (2003), pp. 362-374

[Friedl09] Friedl P, Gilmour D *Collective cell migration in morphogenesis, regeneration and cancer* Nature reviews Mol. Cell Biol., 10 (2009), pp. 445-457

[Garcia09] Garcia G L, Rericha E C, Heger C D, Goldsmith P K, Parent C A *The group migration of Dictyostelium cells is regulated by extracelular chemoattractant degradation* Mol. Biol. Cell, 20 (2009), pp. 3295-3304

[Gardiner09] Garinder C *Stochastic methods: A handbook for the natural and social sciences* Springer series in synergetics, 4 (2009)

[Gaush66] Gaush C R , Hard W L *Characterization of an established line of canine kidney cells (MDCK)* Proceedings of the Society for Experimental Biology and Medicine, 122 (1966), pp. 931-935

[Ghysen04] Ghysen A, Dambly-Chaudiére C *Development of the zebrafish lateral line* Curr Opin Neurobiol, 14(1) (2004), pp. 67-73

[Gompel01] Gompel N, et. al *Pattern formation in the lateral line of zebrafish* Mech Dev, 105 (2001), 1-2, pp. 69-77

[Goueli98] Goueli S A, Hsiao K, Lu T, Simpson D *U0126: A novel, selective and potent inhbitor of MAP Kinase Kinase (MEK)* Promega Notes, 69 (1998), pp. 6-11

[Gregor10] Gregor T, Fujimoto K, Masaki N, Sawai S *The onset of collective behavior in social amoebae* Science, 328 (2010), pp. 1021-1025

[Grill99] Grill S, Stelzer E H K *Method to calculate lateral and axial gain factors of optical setups with a large solid angle* J Opt Soc Am A, 16 (1999), pp. 2658-2665

[Gonzalez03] Gonzalez R C, Woods R E, Eddins S L *Digital image processing using matlab* Prentice Hall, (2003)

[Guck10] Guck J, Lautenschläger F, Paschke S, Beil M *Critical review: Cellular mechanobiology and amoeboid migration* Integr Biol, 2 (2010), pp. 575-583

[Haas06] Haas P, Gilmour D *Chemokine signaling mediates selforganizing tissue migration in the zebrafish lateral line* Dev. Cell, 10(5) (2006), pp. 673-680

[Haralick92] Haralick R M, Shapiro L G *Computer and Robot Vision* Addison-Wesley, 1 (1992)

[Hava09] Hava D, Forster U, Matsuda M, Cui S, Link B A, Eichhorst J, Wiesner B, Chitnis A, Abdelilah-Seyfried S *Apical membrane maturation and cellular rosette formation during morphogenesis of the zebrafish lateral line* J Cell Sci, 122 (2009), pp. 687-695

[Heim95] Heim R, Cubitt A B, Tsien R Y *Improved green fluorescence* Nature, 373 (1995), pp. 663-664

[Horstmann04] Horstmann D, Stevens A *A Constructive Approach to Traveling Waves in Chemotaxis* J. Nonlinear Sci., 14(1) (2004), pp. 1-25

[Honda84] Honda H, Yamanaka H *A computer simulation of geometrical configurations during cell division* J theor Biol, 106, pp. 423-435

[Huang99] Huang S, Ingber D *The structural and mechanical complexity of cell-growth control* Nat Cell Biol., 1(5) (1999), pp. E131-138.

[Huang02] Huang S, Ingber D *A discrete cell cycle checkpoint in late G1 that is cyoskeleton dependent and MAP kinase (Erk)-independent* Exp. Cell Res., 275 (2002), pp. 255-264

[Hufnagel07] Hufnagel L, Teleman A, Rouault H, Cohen S, Shraiman B *On the mechanicsm of wing size determination in fly development* PNAS, 104(10) (2007), pp. 3835-3840

[Huisken09] Huisken J, Stainier D Y R *Selective plane illumination microscopy techniques in developmental biology* Dev, 136 (2009) pp. 1963-1975

[Jordan93] Jordann M A, Toso R J, Thrower D, Wilson L *Mechanism of mitotic block and inhibition of cell proliferation by taxol at low concentrations* PNAS, 90 (1993), pp. 9552-9556

[Käfer07] Kafer J, Hayashi T, Marée A F M, Carthew R W, Graner F *Cell adhesion and cortex contractility determine cell patterning in the drosophila retina* PNAS, 104(47) (2007), pp. 18549-18554

[Katsumi05] Katsumi A, Naoe T, Matsushita T, Kaibuchi K, Schwartz M A *Integrin activation and matrix binding mediate cellular responses to mechanical stretch* J Biol Chem, 280 (2005), pp. 16546-16549

[Keller71] Keller E, Segel L *Model for Chemotaxis* J. Theor. Biol., 30(2) (1971), pp. 225-234

[Kiehart00] Kiehart D P, Galbraith C G, Edwards K A, Riekoll W L, Montague R A *Multiple forces contribute to cell sheet morphogenesis for dorsal closure in drosophila* JCB, 149(2) (2000) pp. 471-490

[Krzic09] Krzic U *Multiple-view microscopy with light-sheet based fluorescence microscope* Ruperto-Carola Unversity Heidelberg, (2009), PhD Thesis

[Kuramoto84] Kuramoto Y *Chemical oscillations, waves, and turbulence* Springer, (1984)

[Landau91] Landau L D, Lifschitz E M *Lehrbuch der theoretischen Physik VII Elastizitätstheorie* Akademischer Verlag, 7 (1991)

[Landsberg09] Landsberg K, Farhadifar R, Ranft J, Umetsu D, Widman T, Bittig T, Said A, Jülicher F, Dahmann C *Increased cell bond tension governs cell sorting at the drosophila anteroposterior compartment boundary* Current Biology, 19(22) (2009), pp. 1950-1955

[Lankton09] Lankton S *Sparse field methods - technical report* Georgia Institute of Technology, (2009)

[Lauffenburger96] Lauffenburger D A, Horwitz A F *Cell Migration: A physically integrated molecular process* Cell, 84 (1996), pp. 359-369

[Lecaudey06] Lecaudey V, Gilmour D *Organizing moving groups during morphogenesis* Curr Opin Cell Biol, 18(1), pp. 102-107

[LecaudeyCakan08] Lecaudey V, Cakan-Akdogan G, Norton WH, Gilmour D *Dynamic Fgf signaling couples morphogenesis and migration in the zebrafish lateral line primordium* Development, 135(16) (2008), pp. 2695-2705

[Lecuit07] Lecuit T, Lenne P F *Cell surface mechanics and the control of cell shape, tissue patterns and morphogenesis* Nature Rev Mol Cell Biol, 8 (2007), pp. 633-644

[Lecuit08] Lecuit T *"Developmental mechanics": cellular patterns controlled by adhesion, cortical tension and cell division* HFSP J, 2(2) (2008), pp. 72-78

[Lippincott-Schwartz03] Lippincott-Schwartz J, Patterson G H *Development and use of fluorescent protein markers in living cells* Science, 300(87) (2003), pp. 87-91

[Mark10] Mark S, Shlomovitz R, Gov N S, Poujade M, Grasland-Mongrain E, Silberzan P *Physical model of the dynamic instability in an expanding cell culture* Biophys J, 98 (2010), pp. 361-70.

[Martz72] Martz E, Steinberg M *The role of cell-cell contact in "contact" inhibition of cell division: a review and new evidence.* J. Cell Physiol., 79 (1972), pp. 189-210

[Matsubayashi04] Matsubayashi Y, Ebisuya M, Honjoh S, Nishida E *ERK activation propagates in epithelial cell sheets and regulates their migration during wound healing* Curr Biol, 14 (2004), pp. 731-735

[Menon10] Menon G I *Active Matter* arXiv:1003.2032v1 [cond-mat.soft], (2010)

[Mitiche10] Mitiche A, Ben Ayed I *Variational and level set methods in image segmentation* Spinter, Topics in singal processing 5 (2010)

[More80] Moré J J, Garbow B S, Hillstrom K E *User Guide for MINPACK 1* Argonne National Laboratory, Tech. Rep. ANL, (1980), 80-74

[Mumford89] Mumford D, Shah J *Optimal approximations by piecewise smooth functions and associated variational problems* Comm. Pure Appl. Math., 42(5) (1989), pp. 577-685

[Nechiporuk08] Nechiporuk A, Raible DW *FGF-dependent mechanosensory organ patterning in zebrafish* Science, 320(5884) (2008), pp. 1774-1777

[Nelson05] Nelson C M, Jean R P, Tan J L, Liu W F, Sniadecki N J, Spector A A, Chen C S *Emergent patterns of growth controlled by multicellular form and mechanics* PNAS, 102(33) (2005), pp. 11594-11599

[Nikolic06] Nikolić D L, Boettiger A N, Bar-Sagi D, Carbeck J D, Shvartsman S Y *Role of boundary conditions in an experimental model of epithelial wound healing* Am J. Physiol. Cell Physiol., 291 (2006), pp. C68-C75

[O'Neill83] O'Neill B *Semi-Riemannian Geometry* Academic Press, Mathematics 103 (1983)

[Orr06] Orr W A, Helmke B P, Blackman B R, Schwartz M A *Mechanisms of mechanotransduction* Dev. Cell, 10 (2006), pp. 11-20

[Osher03] Osher S, Fedkiw R *Level set methods and dynamic implicit surfaces* Springer, Applied Mathematical Series, 153 (2003)

[Otsu79] Otsu N *A threshold selection method from gray-level histograms* IEEE Trans Sys Man Cyber, 9(1) (1979), pp. 62-66

[Painter09] K.J. Painter *Continuous Models for Cell Migration in Tissues and Applications to Cell Sorting via Differential Chemotaxis* Bull. Math. Biol., 71(5) (2009), pp. 1117-1147

[Paragios02] *Geodesic active regions: a new framework to deal with frame partition problems in computer vision* JVCI, 13(1-2) (2002), pp. 249-268

[Petitjean10] Petitjean L, Reffay M, Grasland-Mongrain E, Poujade M, Ladoux B, Buguin A, Silberzan P *Velocity fields in a collectively migrating epithelium* Biophys. J., 98(9) (2010), pp. 1790-1800

[Phillips09] Phillips R, Kondev J, Theriot J *Physical biology of the cell* Gerland Science, (2009)

[Poujade07] Poujade M, Grasland-Mongrain E, Hertzog A, Jouanneau J, Chavrier P, Ladoux B, Buguin A, Silberzan P *Collective migration of an epithelial monolayer in response to a model wound* PNAS, 104(41) (2007), pp. 15988-15993

[Press07] Press W H, Teukolksy S A, Vetterling W T, Flannery B P *Numerical recipes 3rd edition: The art of scientific computing* Cambridge University Press, (2007)

[Puliafito11] Puliafito A, Hufnagel L, Neveu P, Streichan S J, Sigal A, Fygenson K, Shraiman B *Collective and single cell behaviour in epithelial contact inhibtion* PNAS submission.

[Raffel98] Raffel M., Willert Christian E. K J *Particle image velocimetry: A practical guide.* Springer, (1998)

[Ramaswamy10] Ramaswamy S *The mechanics and statistics of active matter* Annu Rev Condens Matter Phys, 1 (2010), pp. 323-345

[Rauzi08] Rauzi M, Verant P, Lecuit T, Lenne P *Nature and anisotropy of cortical forces orienting drosophila tissue morphogenesis* Nature Cell Biology, 10(12) (2008), pp. 1401-1410

[Richardson72] Richardson W H *Bayesian-based iterative method of image restoration* JOSA, 62(1) (1972), pp. 55-59

[Riedl08] Riedl J, et. al. *Lifeact: a versatile marker to visualize F-actin* Nature Methods, 5(7) (2010), pp. 605-607

[Revenu09] Revenu C, Gilmour D *EMT 2.0: shaping epithelia through collective migration* Curr. Opin. Genet. Dev., 19 (2009), pp. 338-342

[Roovers03] Roovers K, Assoian R K *Effects of rho kinase and actin stress fibers on sustained extracellular signal-regulated kinase activity and activation of G1 phase cyclin-dependent kinases* Mol Cell Biol, 23(12) (2003), pp. 4283-4294

[Rorth07] Rorth P *Collective guidance of collective cell migration* Trends in Cell Biology, 17(12) (2007), pp. 407-429

[Rorth09] Rorth P *Collective cell migration* Annu. Rev. Cell Dev. Biol., 25 (2009), pp. 407-429

[Rothen-Rutishauser98] Rothen-Rutishauser B, Krämer SD, Braun A, Günthert M, Wunderli-Allenspach H *MDCK cell cultures as an epithelial in vitro model: cytoskeleton and*

tight junctions as indicators for the definition of age-related stages by confocal microscopy. Pharm Res, 15 (1998), pp. 964-971

[Sakaue-Sawano08] Sakaue-Sawano A, Kurokawa H, Mormura T, Hanyu A, Hama H, Osawa H, Kashiwagi S, Fukami K, Miyata T, Miyoshi H, Imamura T, Ogawa M, Masai H, Miyawaki A *Visualizing spatiotemporal dynamics of multicellular cell-cycle progression* Cell, 132(3) (2008), pp. 487-498

[Samson99] Samson C, Blanc-Féraud L, Aubert G, Zerubia J *A level set model for image classification* Lecture Notes in Computer Science, 1682 (2005), pp. 306-317

[Scheck99] Scheck F *Theoretische Physik 1: Mechanik. Von den Newtonschen Gesetzen zum deterministischen Chaos* Springer, 6 (1999)

[Sengupta09] Sengupta A, van Teeffelen S, Löwen H *Dynamics of a microorganism moving by chemotaxis in its own secretion* Phys. Rev. E, 80(3) (2009), pp. 1-9

[Sethian08] Sethian J A *Level set methods and fast marching methods* Cambridge University Press, (2008)

[Shaw09] Shaw T J, Martin P *Wound repair at a glance* J. Cell Sci., 122 (2009), pp. 3209-3213

[Sherr96] Sherr C J *Cancer cell cycles* Science, 274 (1996), pp. 1672-1677

[Shixiong04] Shixiong L, Edward R, Balkovetz D *Evidence for ERK1/2 phosphorylation controlling contact inhibition of proliferation in Madin-Darby canine kidney epithelial cells.* Am J Physiol Cell Physiol, 287 (2004), pp. C432-C439.

[Shraiman05] Shraiman B *Mechanical feedback as a possible regulator of tissue growth* PNAS, 102(9) (2005), pp. 3318-3323

[Soille99] Soille, P., *Morphological image analysis: Principles and applications* Springer, (1999)

[Solem05] Solem J E, Overgaard N C *A geometric formulation of gradient descent for variational problems with moving surfaces* Lecture Notes in Computer Science, 3459 (2005), pp. 419-430

[Solon09] Solon J, Kaya-Copur A, Colombelli J, Brunner D *Pulsed forces timed by a ratchet-like mechanism drive directed tissue movement during dorsal closure* Cell, 137(7) (2009), pp. 1331-1342

[Sorger97] Sorger P K, Dobles M, Tournebize R, Hyman A A *Coupling cell division and cell death to microtubule dynamics* Curr Opin Biol, 9(6) (1997), pp. 807-814

[Stephens08] Stephens L, Milne L, Hawkins P *Moving towards a better understanding of chemotaxis* Curr. Biol. 18(11) (2008), pp. 485-494

[Streichan11] Streichan S J, Valentin G, Gilmour D, Hufnagel L *Collective cell migration guided by dynamically maintained gradients* Accepted for publication in Physical Biology.

[Stupack02] Stupack D G, Cheresh D A *Get a ligand, get a life: integrins, signaling and cell survival* J. Cell Sci., 115 (2002), pp. 3729-3738

[Tambe10] Tambe D Y, Hardin C C, Fredberg J J, Trepat X *Collective cell guidance by cooperative intercellular forces* nature pre, in press

[Taub79] Taub M, Chuman L, Saier M, Sato G *Growth of Madin-Darby canine kidney epithelial cell (MDCK) line in hormone-supplemented,serum-free medium* PNAS, 76(7) (1979), pp. 3338-3342

[Thompson92] Thompson D W *On growth and form* Dover, (1992)

[Tinkle08] Tinkle C L, Pasolli H A, Stokes N, Fuchs E *New insights into cadherin function in epidermal sheet formation and maintenance of tissue integrity* PNAS, 105 (2008), pp. 15405-15410

[Trepat07] Trepat X, Deng L, Ann S S, Nevajas D, Tschumperlin D J, Gerthoffer W T, Butler J P, Fredberg J J *Universal physical responses to stretch in the living cell* Nature, 447(7144) (2007), pp. 592-595

[Trepat09] Trepat X, Wasserman M R, Angelini T E, Millet E, Weitz D A, Butler J P, Fredberg J J *Physical forces during collective cell migration* Nature Physics, 5 (2009), pp. 426-430

[Valentin07] Valentin G, Haas P, Gilmour D *The chemokine sdf1a coordinates tissue migration through the spatially restricted activation of cxcr7 and cxcr4b* Curr. Biol., 17(12) (2007), pp. 1026-1031

[Valentin09] Valentin G *Chemokine receptors orchestrate collective cell migration in the zebrafish lateral line* Universite Montpellier II, (2009), PhD Thesis

[Vaughan66] Vaughan R B, Trinkaus J P *Movements of epithelial cell sheets in vitro* J Cell Sci, 1 (1966), pp. 407-413

[Vese02] Vese L A, Chan T F *A multiphase level set framework for image segmentation using the mumford and shah model* International Journal of Computer Vision,50(3) (2002), pp. 271-293

[Vicente-Manzanares05] Vicente-Manzanare M, Webb D J, Horwitz A R *Cell migration at a glance* J. Cell Sci., 118 (2005), pp. 4917-4919

[Villablanca06] Villablanca E, et. al. *Control of cell migration in the zebrafish lateral line: implication of the gene "tumour-associated calcium signal transducer," tacstd* Dev Dyn., 235(6) (2006), pp. 1578-1588

[Vitorino08] Vitorino P, Meyer T *Modular control of endothelial sheet migration* Genes Dev., 22 (2008), pp. 3268-3281

[Whitaker98] Whitaker R *A level-set approach to 3D reconstruction from range data* Int J Comp Vis, 29(3) (1998), pp. 203-231

[Weijer09] Weijer C J *Collective cell migration in development* J. Cell Sci., 122 (2009), pp. 3215-3223

[Wolpert07] Wolpert L, Jessel T, Lawrence P, Meyerowitz E, Robertson E, Smith J *Principles of Development* Oxford University Press, 3 (2007)

[Zhao96] Zhao H K, Chan T, Merriman B, Osher S *A variational level set approach to muliphase motion* J Comp Phys, 127 (1996), pp. 179-195

Eidesstattliche Versicherung

Hiermit versichere ich an Eides statt, dass ich die vorliegende Arbeit selbstständig und ohne Benutzung anderer als der angegebenen Hilfsmittel angefertigt habe. Die aus anderen Quellen oder indirekt übernommenen Daten und Konzepte sind unter Angabe der Quelle gekennzeichnet. Die Arbeit wurde bisher weder im In- noch im Ausland in gleicher oder ähnlicher Form in einem Verfahren zur Erlangung eines akademischen Grades vorgelegt.

Saarbrücken, 16. Mai 2011

Sebastian J Streichan